AN ABSTRACT OF THE DISSERTATION OF

Mark J. Kendrick for the degree of Doctor of Philosophy in Physics presented on May 25, 2012.
Title: Light-matter Interactions: From the Photophysics of Organic Semiconductors to High Spatial Resolution Optical Tweezer-controlled Nanoprobes.

Abstract approved:_____
Oksana Ostroverkhova

Studies of light-matter interactions in organic semiconductors and in optical tweezer trapping of nanoparticles are presented. In the research related to organic semiconductor materials, a variety of novel materials and their composites have been characterized, and physical mechanisms behind their optoelectronic properties have been established. Three novel functionalized hexacene derivatives were deemed sufficiently stable to enable characterization of these materials in devices. From dark current and photocurrent measurements of the hexacene thin-films, it was determined that all three derivatives are photoconductive in the near-infrared, and space charge limited mobility values were obtained. In addition, physical mechanisms behind charge transfer, charge carrier photogeneration, and charge transport in small-molecule donor/acceptor composite films have been systematically studied. In these studies, it was determined that the charge transfer from the donor to the acceptor molecule can result in either an emissive charge transfer exciton (exciplex) or a non-emissive charge transfer exciton formation, depending on the energy difference between LUMO of the donor and the

acceptor. However, the most dramatic trends in photoluminescent and photoconductive properties of the donor/acceptor composites were correlated with the separation between the donor and acceptor molecules at the donor/acceptor interface. In particular, composite films with larger separations exhibited electric field-assisted charge transfer exciton dissociation, which contributed to nanosecond time-scale photocurrents under a 500 ps pulsed photoexciation. Large donor/acceptor separation also resulted in reduced charge carrier recombination, which led to a factor of 5-10 increase in continuous wave photocurrents in certain donor/acceptor composites, as compared to those in pristine donor films.

In the optical tweezer based studies, work towards the development of high spatial resolution optical tweezer controlled nanoprobes is presented. In particular, the possibility of exploiting the optical resonance of a particle to increase the optical tweezer forces acting on it within the trap has been investigated. Such an increase in the force would improve the potential spatial resolution of an optical tweezer controlled probe. Experimental results and numerical simulations on micron sized resonant dielectric particles showed a small increase in the optical forces that confine such particles within the trap, when tweezer trapping is conducted at wavelengths on the red-side of the optical resonance. Preliminary work on optical tweezer controlled ion/pH sensitive probes and on surface charge measurements is also reported.

Light-matter Interactions: From the Photophysics of Organic Semiconductors to High Spatial Resolution Optical Tweezer-controlled Nanoprobes.

by
Mark J. Kendrick

A DISSERTATION

submitted to

Oregon State University

in partial fulfillment of
the requirements for the
degree of

Doctor of Philosophy

Presented May 25, 2012
Commencement June 2012

Doctor of Philosophy dissertation of Mark J. Kendrick presented on May 25, 2012.

APPROVED:

_____

Major Professor, representing Physics

_____

Chair of the Department of Physics

_____

Dean of the Graduate School

I understand that my dissertation will become part of the permanent collection of Oregon State University libraries. My signature below authorizes release of my dissertation to any reader upon request.

_____

Mark J. Kendrick, Author

ACKNOWLEDGEMENTS

I would like to express thanks to the many people who have made this thesis work possible. First, I would like to thank my advisor, Dr. Oksana Ostroverkhova for the support and guidance she has provided me. Her endless energy, creativity, and passion are truly inspirational. I would also like to thank Dr. David McIntyre, for his guidance and expertise in optical tweezers. I also owe appreciation to my lab mates past and present, Jonathan Day, Andy Platt, and Whitney Shepherd who have provided me with crucial technical assistance throughout the years. I am also grateful to Afina Neuntzert who has helped me carry out many experiments.

I would also like to thank my family for being supportive of me on this long, long journey. Finally, I would like to thank my fiancée Lyndsey for providing me support and sanctuary on a daily basis. I truly can't imagine getting through the past four years without you

TABLE OF CONTENTS

TABLE OF CONTENTS (Continued)

Page

TABLE OF CONTENTS (Continued)

Page

TABLE OF CONTENTS (Continued)

Page

TABLE OF CONTENTS (Continued)

Page

LIST OF FIGURES

LIST OF FIGURES (Continued)

Figure Page

LIST OF FIGURES (Continued)

Figure Page

LIST OF FIGURES (Continued)

Figure Page

LIST OF FIGURES (Continued)

Figure Page

LIST OF TABLES

Table Page

This dissertation is dedicated to Lyndsey, meeting you confirmed that coming to Oregon State is the best decision I've ever made.

1. Introduction

The interaction of light and matter is fundamental to many areas of research. These interactions, which are dictated by how matter absorbs, scatters, and transmits light over the entire radiative spectra, can, for example, be used as a tool to (i) probe the properties of matter, or (ii) to manipulate matter. The work presented in this thesis lies in two distinctly different research areas that employ light matter interactions in the two aforementioned ways. The first area is in the study of the (opto)electronic properties of organic semiconductors, and the second is in the application of optical tweezers.

1.1 Organic Semiconductors

Organic semiconductors are an important class of materials that have shown promise for use in applications that include: thin-film transistors, light-emitting diodes (LED), photovoltaic cells, photorefractive devices, photosensors, and lasers. An example of an organic-LED flexible, transparent laptop display by Samsung is shown in Fig 1.1 Organic-LED displays have been shown to have dramatically higher contrast than standard inorganic-LED displays. Another promising feature of these materials is that they can be processed using low-cost solution based techniques, such as spin-casting or ink printing. Given their potential, understanding the photophysical processes in these materials is an active area of research. Research with organic semiconductors presented in this thesis is focused on furthering the knowledge base of the (opto)electronic properties of a specific class of solution processable small-molecule organic

semiconductor materials; as well as to aid in the pursuit of new and better performing materials.

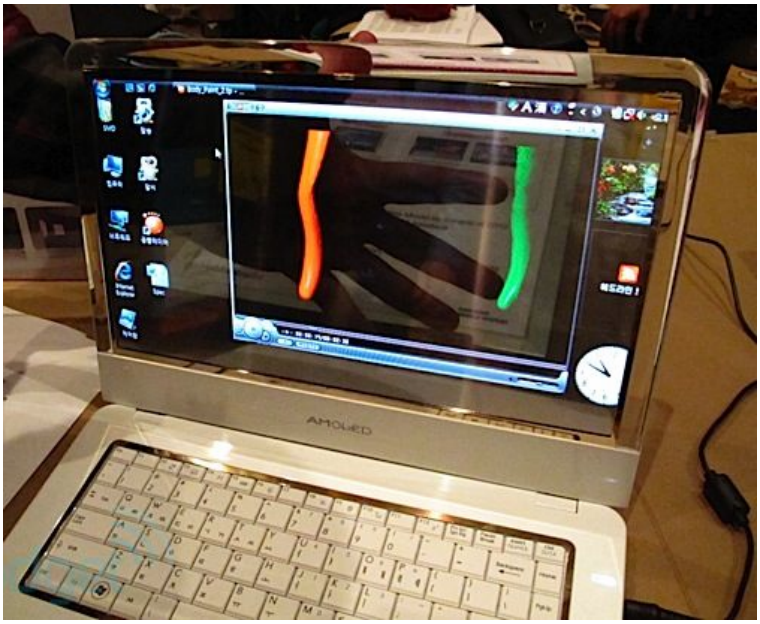

Figure 1.1: An image of a transparent, flexible organic LED laptop display designed by Samsung (image taken from http://www.oled-info.com/samsung-oled).

The work presented on this topic is organized as follows: in Chapter 2, background is given on the current understanding of photophysical properties in these materials, such as charge carrier photogeneration and charge transport; a discussion of our group's work in this field is also included. In Chapter 3, a study characterizing the stability, optical response, and (photo)conductivity of a new and novel hexacene material is presented. In Chapter 4, a temperature dependence study of the optical and conductive properties in donor/acceptor composite thin-films is described. Experimental results from the study that determined photophysical processes in the films are also discussed in the chapter. In Chapter 5, a study on a wide range of donor/acceptor composite materials

that was conducted to identify key factors behind charge transfer and charge carrier photogeneration in these materials is presented.

1.2 Optical Tweezers

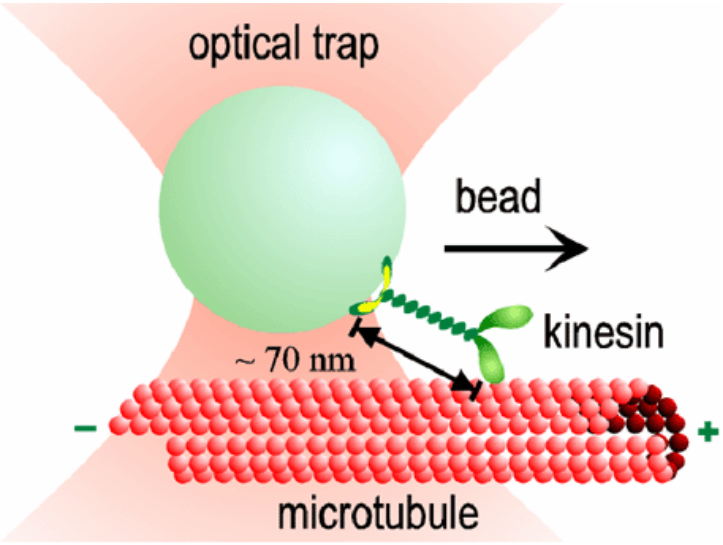

Figure 1.2: A diagram depicting an optical tweezer based experiment to determine kinesin motor dynamics. The kinesin motor is tethered to an optically trapped particle. As the kinesin motor, which can not be resolved by an optical microscope, moves it displaces the bead within the trap. The position of the bead can readily be monitored, allowing the motion of the motor to be resolved. This experiment determined that kinesin motors move in discrete ~8nm steps. Figure is taken from http://www.stanford.edu/group/blocklab/kinesin.html and adapted from Ref [1].

Since their inception in the early 1970s, optical tweezer traps, which provide the ability to confine, manipulate, and apply picoNewton forces on microscopic objects, have been of interest. Optical tweezers have been used in applications spanning the fields of biology, chemistry, engineering, and physics. For example, they have routinely been used in single molecule level studies of molecular motors (Fig. 1.2). An additional and exciting application is the use of an optical tweezer trapped particle as a high-spatial

resolution probe of the local environment of the confined particle. The research on optical tweezers presented in this thesis is along these lines. In particular, we were interested in (i) trying to improve the achievable spatial resolution of an optical tweezer controlled probe, and (ii) develop new optical tweezer based probes.

The research conducted with optical tweezers is presented in Chapter 6 and is organized as follows: In Section 6.1, an introduction to optical tweezers is given, along with the motivation behind using the optical properties of a particle to improve the spatial resolution of optical tweezer based probes. In Section 6.2, the theory behind optical tweezer traps and the forces acting on a particle in a trap are presented. The theory behind resonant enhancement of the optical tweezer force is also presented in this section. In Section 6.3, a study on the wavelength dependence of the optical tweezer force acting on dye-doped polystyrene particles is discussed. This study includes both experimental results and numerical simulations of the optical tweezer trapping force acting on the optically resonant dye-filled particles. In Section 6.4, preliminary work, using optically trapped ion-selective fluorescent particles as probes is described. Finally, in Section 6.5 preliminary work on surface charge measurements with optical tweezer trapped particles is presented.

2. Organic Semiconductor Materials background

2.1 Organic Semiconductor Materials

In the early 1900s the first studies on small molecular weight organic materials revealed that they were conductive (both dark and photo) [2]. Later, the discovery of electroluminescence in the 1960s motivated additional research on organic molecular crystals, from which the basis for the current understanding of fundamental optoelectronic processes in these materials was established [3]. During the past two decades, major improvements in organic synthesis and purification have been made. These improvements have resulted in a dramatic boost in material performance, thus increasing their potential for use in (opto)electronic applications. To date, organics have been implemented in many applications including, but not limited to, organic thin-film transistors (OTFTs), organic light emitting diodes (OLEDs), organic solar cells, sensors, organic lasers, and photorefractive devices [4-8]. This pioneering work along with continued development of materials with improved performance and highly tunable (opto)electronic properties, which can be fabricated using low cost techniques (e.g. solution deposition), have made organic semiconductors a very promising class of materials.

In the above mentioned applications two major classes of organic semiconductors have been utilized (i) (photo)conductive polymers and (ii) small molecular weight materials. However, for the low cost solution deposition techniques that our group employs, undoped polymers typically have much lower mobilities than small molecule

organics. In this work, small molecule organic materials, such as pentacene and anthradithiophene (ADT), will be discussed. Although significant progress has been made in understanding the photophysics of small molecule organic materials, there is still much that is not completely understood. Basic mechanisms such as charge carrier generation pathways upon photoexcitation are still up for debate and research on the photophysics in organic semiconductors is ongoing. This chapter provides an overview of the current understanding of the optical and electronic processes in small molecule organic semiconductor materials.

2.2 Polyacene Molecules and Crystals

Given the potential of organic semiconductor materials, much effort has been invested in understanding the (opto)electronic properties of these materials and the underlying physical mechanisms defining these properties. In particular, the mechanisms behind charge carrier photogeneration and transport in these molecular materials has been explored extensively [9-11].

The materials studied in this work are polyacenes, which consist of a succession of joined benzene rings that form a rigid 'backbone' of a fixed length. Along the backbone the sp^2 hybridized orbitals of the carbon atoms form σ-bonds with adjacent carbon atoms, while p_z orbitals form π-bonds. The weak π-bonds result in delocalized electrons which are shared along the backbone of the polyacene molecule. The formation of the π-bonds results in splitting of the initial p_z electronic states of the sp^2 hybridized carbon atoms into bonding orbitals and anti-bonding orbitals. The p_z electrons occupy

the π bonding orbitals, which are referred to as the highest occupied molecular orbital (HOMO), while the anti-bonding orbitals are left empty and are referred to as the lowest unoccupied molecular orbital (LUMO). The electrons in the π bonding orbitals are delocalized forming electron clouds above and below the plane of an isolated molecule. It is the interactions of these 'π electrons' between adjacent molecules in a crystal that will determine the conduction within these organic materials.

Crystal formation of polyacenes is dictated by van der Waals forces, which are much weaker than the covalent bonding forces in inorganic semiconductor crystals. This results in weaker bonding between molecules, less overlap (or electronic delocalization) between the outer orbital of neighboring molecules, and less effective screening, by electrons in inner orbitals, of the Coulombic forces between charge carriers and nuclei in organic crystals. As a result of the poor electronic delocalization between adjacent molecules, the single molecule HOMO and LUMO levels are a valid approximate description of the energy levels in a molecular crystal from which transport of excitons and charge carriers occur. In addition, the absorption and photoluminescence properties in the solid state are similar to those in solution.

A consequence of the poor electron screening mentioned above, is that photoexcitation in organic semiconductors results in a strongly bound, neutral exciton pair, which can move within the solid transporting energy, but not charge. To generate free carriers (electrons in the LUMO or holes in the HOMO) this excitonic binding energy (typically between 0.1 and 0.8 eV) must be overcome via an applied external

electric field, scattering from a phonon, exciton-exciton scattering, or thermal activation [12]. In the absence of the energy needed to dissociate the exciton, and create a free carrier either in the HOMO or LUMO, the electron-hole pair will most likely experience geminate recombination (recombination of the electron-hole pair within the same molecule from which it originated).

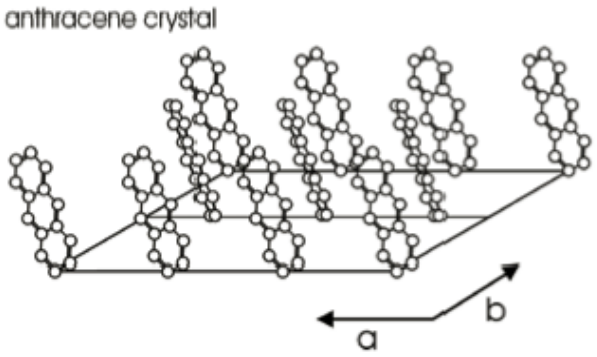

Figure 2.1: A diagram depicting molecular order within an anthracene crystal. Anthracene like other polyacenes tends to arrange into a 'herringbone' edge-to-face packing. Figure taken from Hegmann [12].

Molecular packing of acenes, such as anthracene, tetracene, and pentacene, which is dictated by the weak van der Waals forces, is an edge-to-face or a 'herringbone' orientation, as shown in Fig. 2.1. In this stacking arrangement π-orbitals, with delocalized electrons, interact with neighboring molecules on either side of the acene backbone forming a band that allows for electron transport between molecules (along the a-vector direction in Fig. 2.1). However the herringbone stacking only provides minimal π-orbital overlap [13], which has the implication of somewhat localized charge carriers and thus low mobility. The herringbone packing structure is believed to be an intrinsic limitation of the mobility in polyacene crystals [14].

To address the limitations of herringbone packing and increase the π-orbital overlap, methods to improve packing have been pursued, which include variations in deposition methods and substrate modifications [15, 16]. Another particularly effective technique implemented in the molecules studied herein, has been the functionalization of the acene backbone with a bulky side group that is attached to the backbone with a ridged alkyne 'spacer' (Fig. 2.2(c)) [16]. The purpose of the side groups is to disrupt the edge-to-face packing in the herringbone packing motif to promote purely face-to-face stacking and increase π-orbital overlap between molecules [17]. A detailed study of how various functional groups, added to the pentacene backbone, improved the face-to-face molecular packing was conducted by Anthony in Ref [13]. They found that in cases when the diameter of the side group was between ~4.3 and 7.5 Angstroms (Å) the molecular order was a slip-stack or 'brick-wall' (Fig. 2.2(b)) that did in fact result in both purely face-to-face packing and a reduction in interplanar separation between aromatic rings from ~6.27 Å in pentacene to between ~3.41 and 3.47 Å in the functionalized pentacenes [13]. The face-to-face packing and the reduced interplanar separation resulted in improved electrical properties in single crystal pentacene functionalized with triisopropylsilylethynyl (TIPS) side groups (resistivity ~10^{10} Ω-cm), as compared to non-functionalized pentacene crystals (resistivity ~10^{12} Ω-cm) [17]. Improvements in solution deposited OTFT performance, using the same pentacene with TIPS side groups, was also observed [18].

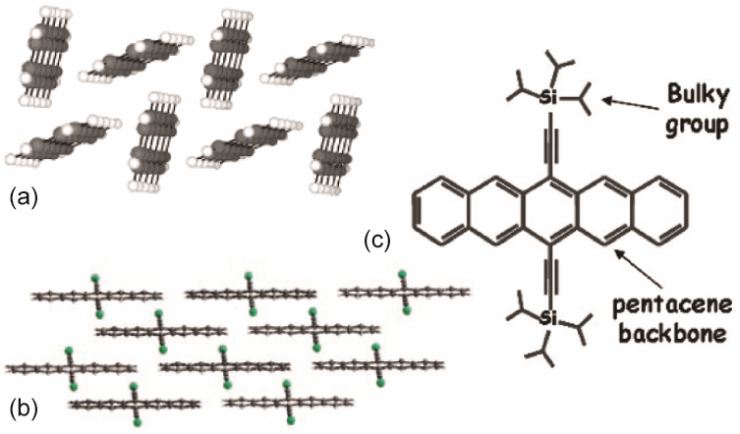

Figure 2.2: An image depicting molecular packing of pentacene and functionalized pentacene. (a) Herringbone molecular packing of pentacene molecules [13]. (b) Brick-wall packing of pentacene molecules functionalized with 'TIPS' side groups [19]. (c) Molecular structure of pentacene-TIPS. The bulky side groups help promote the face-to-face packing in the brick-wall packing motif, which increases the π-orbital overlap between neighboring molecules [18].

2.2.1 Organic Semiconductor Thin-Films

Up to this point, the discussion of organic molecules in the solid state has been focused on crystals. While high quality crystals provide the highest order in the solid state, resulting in very good electrical behavior, they require sophisticated production techniques to produce. As mentioned above, one of the main promises that organic semiconductors provide over inorganics, which are intrinsically better conductors in high quality crystals, is the possibility for low cost fabrication (e.g. solution or print processes). These processes result in polycrystalline or amorphous thin-films, as opposed to single crystals, in the solid-state. In particular, polycrystalline films are composed of many crystal domains within the film. How the crystalline domains form is dependent on the deposition method and conditions, the material, the substrate the film is deposited on,

and the pre-treatment of the substrate [20-22]. Nonetheless, a polycrystalline film, regardless of the exact deposition details, is a more disordered system as compared to single crystals. The increased disorder leads to charge carrier trapping states both in individual crystals that make up the polycrystalline film and at 'grain' boundaries between crystals. The disorder effectively limits the charge transfer, and thus mobility, between molecules in the film due to differences in HOMO-LUMO energies and intersite spacing between molecules. These defects essentially disrupt the ordered molecular packing that provides for π-orbital overlap, where charge is transferred between molecules. An unwanted consequence of the disorder is a reduction in charge carrier mobility in thin-films as compared to single crystals.

In addition to film deposition conditions, functionalization of molecules with side groups has been shown to dramatically improve crystallization in solution deposited thin-films. The improved crystallization has resulted in better material performance. For example the Anthony group displayed the ability to achieve highly ordered solution deposited thin-film transistors using functionalized pentacene and ADT derivatives on treated electrodes that exhibited high mobilities ($\mu > 1.0$ and > 1.5 $cm^2/(Vs)$, respectively) [18, 21]. Mobilities as high as these had previously only been achieved in high-cost vacuum deposited organic devices.

Although the push is towards low-cost fabrication of organic semiconductor devices, research on high quality crystals is still of importance as it provides the ability to study intrinsic physical properties of these materials that can be masked by grain boundaries in films [23]. Measurements on crystals can also be used to determine upper

limits on conductive and photoconductive properties of these materials. Such experiments aid in the ability to design improved next generation organic materials [9]. In this work, results both in high quality crystals and in thin-films from other groups will be referenced, when appropriate, even though the experimental results from our group are from polycrystalline thin-films.

2.3. Optical and Electronic Properties

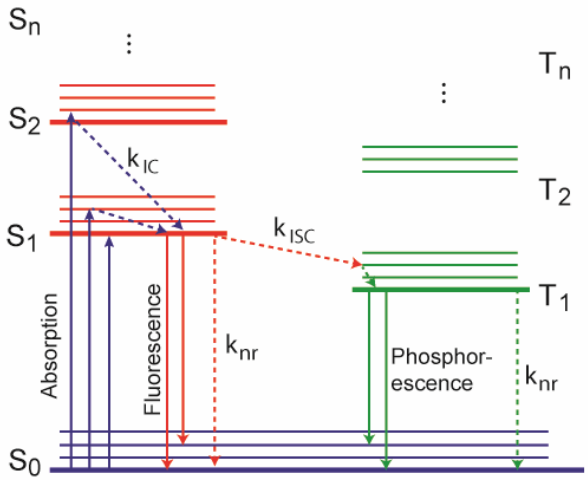

Figure 2.3: Energy level diagram for an organic molecule. Rates for internal conversion (k_{ic}) and nonradiative decays (k_{nr}) are labeled. Transitions between S_0 and excited triplet states (T_n) is forbidden, such that phosphorescence is much less prominent than fluorescence. Intersystem crossing (k_{isc}) is also labeled.

2.3.1 Optical Absorption and Photoluminescence (PL)

Due to the weak van der Waals forces between molecules within an organic semiconductor solid, the properties of individual molecules are retained. Thus, understanding the optical properties of individual molecules is crucial to understanding the optical properties of organic solids. An energy level diagram for an organic molecule

is shown in Fig. 2.3. The ground state is a singlet state, S_0, and excited states are either spin singlet or triplet states (S_n and T_n). The lowest electronic transition ($S_0 \rightarrow S_1$) in these molecules is typically somewhere between the ultraviolet (UV) and near-infrared (NIR) spectral regions ($300 < \lambda < 800$ nm). The small molecule organic materials used in this work have absorption bands in the visible spectrum between $\lambda \sim 500$ and 700nm. For example, the absorption band of fluorinated anthradithiophene (ADT) molecules, functionalized with a 'TES' side group (ADT-TES-F), in toluene is between $\lambda \sim 425$-550nm (Fig. 2.4). Within the absorption band, peaks from vibronic transitions can be resolved (i.e. 0–>m, where m = 1, 2 in Fig. 2.4). In organic molecules, electronic transitions from the $S_0 \rightarrow S_n$, (n>1) relax to the m=0 vibronic level of S_1 (k_{ic}, in Fig. 2.3); with fluorescence occurring from the m=0 vibronic state in S_1 to vibronic states (m=0, 1, 2 ...) in S_0 (Figs. 2.3 and 2.4). The spectral shift between the peak absorption and peak PL is due to Stokes shift and is related to structural relaxation of the molecule after photoexcitation; such that a more rigid molecule has a smaller Stokes shift [24, 25]. Transitions between excited triplet states and S_0 are very weak due to spin selection rules, so that phosphorescence is typically far less prominent than fluorescence.

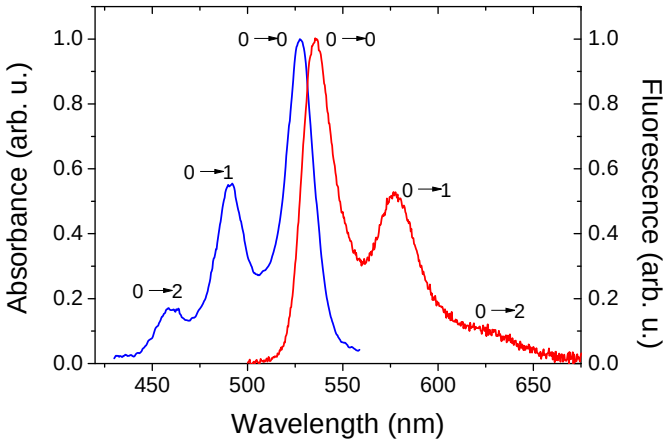

Figure 2.4: Optical absorption (blue) and fluorescence (red) from ADT-TES-F molecules in toluene solution. Transitions to vibronic states are labeled.

The optical properties of organic molecules in the solid state differ from those in solution due to intermolecular interactions, which results in an 'exciton band' (Fig. 2.5). The optical spectra in solid state still exhibit well-defined singlet and triplet spin-states (Fig. 2.6). However, there are a few distinct differences that are typically observed in the solid state relative to isolated molecules that result from the intermolecular interactions: (i) a broadening of spectral peaks, (ii) changes in oscillator strengths for vibronic transitions, and (iii) a red-shift in the overall spectra due to polarization (Fig. 2.6). Given the strong exciton binding energies, optical measurements are extremely useful for understanding processes in organic materials. For example, fluorescence lifetime and electric field (E-field) dependent fluorescence quenching measurements provide information concerning exciton dynamics and dissociation.

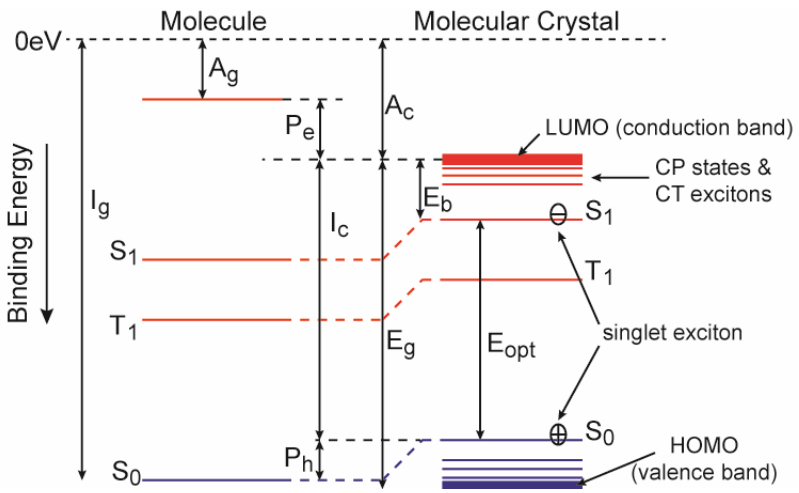

Figure 2.5: Energy diagram for an organic semiconductor molecule and a molecular solid. In the solid state multiple exciton species exist. The onset of optical absorption, labeled E_{opt}, and energies close to this (<~500 meV) result in Frenkel excitons (labeled singlet exciton), which must be dissociated to generate free carriers. Absorption at higher energies can generate less tightly bound bi-molecular excitons (labeled CT excitons), which are more likely to become free-carriers. While excitation at even higher energies ($>E_{opt}$) can either directly generate free carriers in the LUMO or lead to ionization processes that result in charge pair states (CP states) that can also result in free carriers. Also shown: P_e and P_h are polarization energy shifts due to molecular interactions in the solid-state; A_c and A_g are electron affinity energies; I_c and I_g are electron ionization energies; E_b is the singlet exciton binding energy; and E_g is the HOMO/LUMO energy gap. Figure adapted from Ref [26].

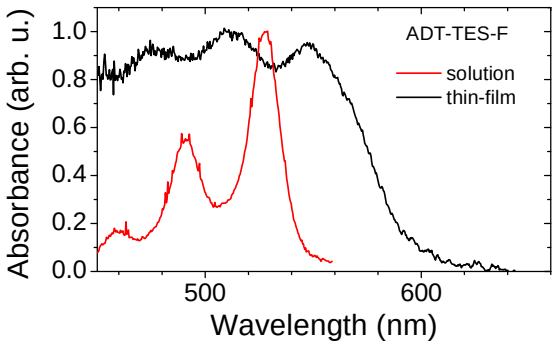

Figure 2.6: Optical absorption spectra of ADT-TES-F in toluene solution and in a solution deposited thin-film. The thin-film spectrum is red-shifted and has broadened spectral features, as compared to solution spectrum, due to intermolecular interactions in the solid-state.

2.3.2 Charge Carrier Photogeneration

Charge carrier photogeneration in organic semiconductors, unlike in inorganic semiconductors, is hindered by exciton binding energy. In inorganic semiconductor crystals, an absorbed photon with energy equal to or greater than the energy of the onset of optical absorption (or band gap) promotes an electron from the ground state or valence band directly into the conduction band where it is a free carrier. While in organic semiconductors a photon with energy equal to the onset of optical absorption (E_{opt} in Fig. 2.5) does not promote the electron to the LUMO level (the organic semiconductor equivalent of the conduction band), but rather promotes the electron from the singlet ground state of a molecule (S_0) to the excited state (S_1) (Fig. 2.5). The excited electron, instead of being a free carrier shared between molecules in the solid, is strongly bound to the hole in the S_0 state, forming a highly localized or Frenkel exciton (labeled singlet exciton in Fig. 2.5). Excitons can move within the solid between adjacent molecules, transferring energy but not charge. To transfer charge, the exciton must be dissociated to generate a free carrier. The energy needed to generate a free carrier by promoting the electron(hole) from $S_1(S_0)$ into to the LUMO(HOMO) is the exciton binding energy, E_b (Fig. 2.5). In typical small molecule organic semiconductors the binding energy is on the order of ~0.1 to 0.8 eV, which implies that the likelihood of promoting a free carrier to the LUMO or HOMO from a singlet exciton via an external field, scattering from a phonon or a neighboring exciton, or thermal activation is very small. Thus, generation of photocurrent under these circumstances is extremely inefficient. Instead singlet excitons

experience geminate recombination, either through radiative or nonradiative processes, on very short time-scales (~ns) with high probability.

Additional pathways for charge carrier photogeneration occur when higher energy photons are absorbed (Fig. 2.7). The observation of a threshold energy, E_{th}, for the onset of photoconductivity is common in organic semiconductors, such that $E_{th} > E_{opt}$. For example in pentacene, E_{opt} ~1.9 and E_{th} ~2.2 eV. At energies just above the threshold energy, there are two competing processes for charge carrier photogeneration: (i) autoionization of excited molecular states and (ii) dissociation of charge transfer excitons that are created via direct optical charge transfer between adjacent molecules. At even higher photon energies the autoionization process becomes the dominate mechanism for charge generation [3].

The autoionization mechanism for free carrier generation is a multistep process. The initial absorption leads to exciton formation followed by the autoionization of the excited molecular state creating a positively charged parent ion and a hot electron with excess kinetic energy. The hot electron then loses its excess energy via scattering and thermally relaxes at a distance r_{th} from the parent ion on a neighboring molecule; such that r_{th} increases with the energy of the initially absorbed photon (Fig. 2.7). After thermal relaxation, the initially quasifree electron becomes localized forming a positive and negative polaron pair (CP pair). The CP is bound, but moves within the crystal by noncoherent stochastic hopping. The binding energy of the CP is smaller than that of a singlet exciton given that the distance between the bound charge pair is larger, as described by the Onsager model or variations of the Onsager model [27]. The binding

energies of CP states are typically on the order of the thermal energy at room temperature (25 meV). This allows for a higher probability of dissociation and, thus, makes charge carrier generation more efficient via autoionization.

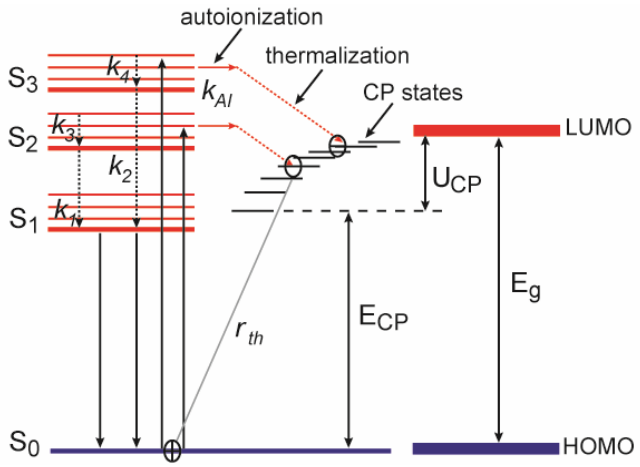

Figure 2.7: Energy diagram showing the autoionization mechanism for charge carrier photogeneration in organic semiconductors. Photoexcitation at energies above the onset of absorption ($S_0 \rightarrow S_1$), leads to autoionization of electrons in the excited state. The autoionized electrons thermalize into CP states at a distance, r_{th}, from the original hole site, with a binding energy, U_{CP}. CP states can then be dissociated to form free carriers in the HOMO and LUMO. Also shown, are the CP state and HOMO/LUMO energy gaps (E_{CP} and E_g), the rate constants for autoionization (k_{AI}), and the rate constants for intramolecular relaxation processes (k_i, for i=1-4). Figure adopted from Ref [3].

2.3.3 Charge Transport in Organic Semiconductors

Following the dissociation of an exciton into free carriers, the freed electron and holes are still relatively localized compared to those in inorganic semiconductors given the van der Waals binding forces between molecules. In addition, the strong polarizability resulting from van der Waals cause free electrons and holes to interact strongly with the neighboring molecules, forming polarons with an effective mass that is larger than the mass of an unbound electron. Given that polarons are charged

quasiparticles their motion within organic solids under an applied electric field is quantified by mobility (μ), which is the velocity gained per electric field, as opposed to neutral quasiparticles, like excitons, whose motion is best quantified by diffusion parameters [10]. However, due to the complicated nature of the polaron interactions within an organic semiconductor the underlying mechanism for transport is controversial, and a complete picture might best be described by multiple processes, of which a few will be discussed below. In addition, the presence of defects in crystals, and to an even further extent the polycrystalline and amorphous morphologies found in thin-films, leads to charge trap states, which further complicates charge transport phenomena in organic semiconductors.

It is most commonly believed that transport of photogenerated free polarons in organic semiconductors is governed by two distinct processes, both of which can be quantified by mobility. The first type of free carrier transport is coherent tunneling of the relatively localized free carriers to neighboring molecules. Tunneling transport is typically observed at low temperatures when phonons are frozen out, but can be present at higher temperatures in materials with extremely low electron-phonon coupling. This transport is characterized by a bandlike power law temperature dependence given by

$$\mu_{tun}(T) \sim T^{-n} \qquad (2.1),$$

where n is a real number greater than 0. The second type of charge transport is non-coherent hopping transport, where the localized free carriers must be thermally activated

to be transported between molecules (or hopping sites). In this case the mobility is described by an exponential probability of being thermally activated and thus has an Arrhenius-like temperature dependence

$$\mu_{hop}(T) \sim e^{(-\Delta/k_B T)} \quad (2.2),$$

where Δ is the activation energy and k_B is the Boltzmann constant. The total intrinsic mobility in organic semiconductors is considered to be

$$\mu(T) = \mu_{tun}(T) + \mu_{hop}(T) \quad (2.3),$$

such that over large temperature ranges, a transition between tunneling dominated transport at low temperatures and hopping dominated transport at higher temperatures can be observed. An example of this is depicted in Fig. 2.8(b) for an organic material with strong electron-phonon coupling, where there are 3 distinct temperature regions: (i) at low temperatures ($T<<T_1$) tunneling transport is dominant, (ii) as the temperature increases ($T_1<T<T_2$) the hopping term is significant and thermal activated transport is dominant, and (iii) at extremely high temperatures ($T>T_2$) thermal energy becomes significant resulting in increased scattering from thermal phonons that counteract the thermal activation of carriers, causing the mobility to again decrease with temperature [10]. The temperatures, T_1 and T_2, are material dependent and as a result the temperature region (iii) is not observed in all organic materials, typically only those with strong electron-phonon coupling.

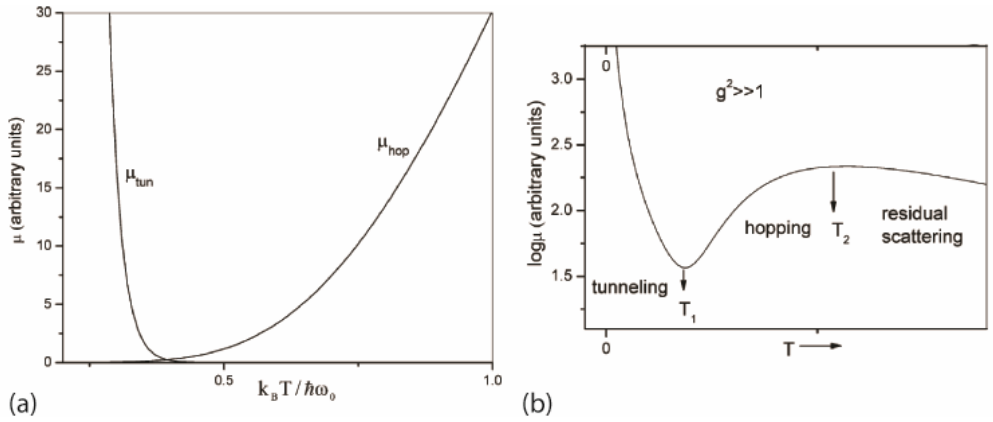

Figure 2.8: Models for the temperature dependence of mobility in organic materials. (a) Simulations of the mobility due to tunneling (μ_{tun}) and hopping (μ_{hop}) as calculated by Holstein in Ref[28]. (b) The temperature dependence of the mobility ($\mu(T)$) in the case of strong electron-phonon coupling, where there are 3 distinctive temperature regions. Figure taken from [10].

It should be noted that, the above description assumes an already formed polaron. However the polaron does not form instantaneously. After the autoionization process that creates the free carrier (as explained above), it first polarizes the electron cloud of the molecule it resides on to form an electronic polaron on the order of ~10^{-16} s after autoionization, followed by vibronic (nuclear) interaction with the molecule it resides on to form a small molecular polaron on the order of ~10^{-15} s after autoionization, and then finally interacts with neighboring molecules on the time-scale of ~10^{-14} s after autoionization to form a lattice polaron. One model that takes this into account, is presented by Silinsh and Capek [3]. In this model, the dynamics described above are represented in changes in the mobility due to the effective mass as the free carrier polarizes its surroundings. After the charge carrier is initially generated, it moves coherently on short time-scales and exhibits bandlike temperature dependence. On

longer time-scales the electronic and vibronic interactions cause a transition to hopping like transport. For simplicity, throughout the remainder of the document, polarons will be referred to as charge carriers.

In single crystals, tunneling (i.e. bandlike behavior with μ that decreases with increasing temperature) and hopping (i.e. μ that increases with increasing temperature) charge transport have been observed. For example tunneling transport was observed at long time-scales in naphthalene crystals [29] and in pentacene crystals [30] at temperatures between 30 and 300K; while a transition from tunneling transport at temperatures between 225 and 300K to hopping like transport at T>300K was observed in pentacene crystals [31]. Time dependent behavior, as discussed above, has also been reported. For example Moses observed tunneling transport on short time-scales, and hopping like transport on long time-scales in tetracene crystals at temperatures between 200 and 400K [32].

In polycrystalline organic semiconductor thin-films, grain boundaries and disorder serve as charge traps, which result in hopping transport due to energy and intersite spacing differences between molecules and domains. Thus, hopping transport can be described by a temperature and electric field dependent mobility [33]. For example hopping transport was observed in continuous wave (cw) photocurrent in functionalized anthradithiophene and pentacene films at temperatures between 300 and 350K [34]. Hopping transport was also observed on ~500ps time-scales in ADT-TES-F thin-films from 100 to 300K [35]; while on sub-ps time-scales, bandlike transport has been observed in pentacene thin-films [36]. However, the nature of bandlike transport

for charge carriers in organic semiconductors, and the mechanism causing the transition from bandlike to hopping charge transport are not completely understood and are still under investigation.

2.4 Focus of Thesis Work on Organic Semiconductor Thin-Films

Research by our group is focused on understanding the photophysics of optoelectronic processes in organic semiconductor thin-films. In particular, we are interested in understanding charge carrier photogeneration and transport on time-scales from picoseconds to seconds, as well as how these phenomena are affected by molecular packing/interactions in thin-films. Our group works specifically with functionalized acenes, including, but not limited to, pentacenes, hexacenes, indenoflourenes, and anthradithiophenes. Early work in our lab was conducted to investigate photogeneration and charge transport processes in thin-films of pristine pentacene and anthradithiophene materials [34, 37, 38]. For example, on picosecond time-scales bandlike photogeneartion of charge carriers were observed. In the same study, the charge transport mechanism at time-scales from tens of picoseconds to hundreds of microseconds was consistent with tunneling of nearly small molecular polarons. However, on longer time-scales thermally activated hopping transport was observed [34].

In addition to the pursuit of a better understanding of (opto)electronic properties, we are also in search of better performing organics and ways in which materials can be tailored for specific applications; such that our group is continuously characterizing new materials that are generously synthesized for us by our collaborators (John Anthony's

Group at the University of Kentucky, Mike Haley's group at the University of Oregon, and Bob Twieg's group at Kent State University).

Recently, our group has investigated the properties of donor/acceptor composite films. These composite films are comprised of two organic materials that are chosen such that they promote charge transfer between donor and acceptor molecules as a mechanism to improve photoconductivity. Our group's studies have been focused on understanding the optical properties, charge transfer mechanisms, charge-carrier photogeneration, and charge transport in composite materials, which employ the high performance ADT-TES-F molecule as the donor. Our early studies showed that charge transfer in composites with different acceptors can have dramatically different (opto)electronic properties, as compared to the pristine materials that make up the composite [39, 40].

In parallel, our group has also worked on understanding how molecular packing and interactions affect the properties of organic semiconductors both in the bulk and on the single molecule levels. Studies have been conducted to understand how aggregation of ADT-TES-F molecules changes when in a polymer or polycrystalline host matrix; and how that affects optical and electronic properties [40, 41]. Currently, work is being conducted to explore how single molecules pack in polymer vs. crystalline hosts, and how that affects the optical properties of ADT-TES-F on the single molecule level [42].

My work on organic materials, has been focused on characterization of new materials and on the continued pursuit of understanding donor/acceptor interactions in composite films. In Chapter 3, work is presented on the optical and electronic

characterization of a new novel hexacene material, which has optical response in the near-infrared, where most of the current small molecule materials do not. In particular, a stability study on this hexacene, which was previously considered to be unstable and, thus, not viable for use in device applications, is presented; along with the first, to our knowledge, results of photocurrent and mobility in hexacene thin-films. In Chapter 4, a study of the photophysical mechanisms of charge carrier photogeneration and charge transport in two composite materials, which exhibit different types of donor/acceptor charge transfer, is presented. In this study temperature dependent measurements were conducted to obtain a model of charge carrier photogeneration in these two composite materials. In these composites, hopping like transport was observed at temperatures between 100 and 300K. Finally in Chapter 5, a study was conducted exploring the effects of molecular packing at the donor/acceptor interface and differences between donor and acceptor LUMO energies on the photophysics in composite thin-films. In this study, a third type of charge transfer was observed. In addition, it was determined that the exciton dynamics can be effectively manipulated by changing the spacing between the donor and acceptor molecules within a composite film.

3. Optoelectronic Characterization of Stable Hexacene Derivatives

3.1 Introduction

3.1.1 Organic Semiconductor Materials

During the past few decades organic semiconductors have been investigated as an alternative to conventional inorganic semiconductors due to their low cost, ease of fabrication, and tunable properties [8]. Acene-based organic materials are one class of materials that have been widely studied and have well documented electrical properties [3, 19, 23]. For example functionalized pentacenes and anthradithiophenes (ADT) have shown high charge carrier mobility and photoconductivity in solution deposited films [18, 21, 34, 38]. The promising performance of small molecule organic materials like these, drives the continued pursuit of materials with improved (opto)electronic performance. In particular, the synthesis of larger acenes, for example hexacene and heptacene, have been pursued [43, 44], given their optical response in the near infrared, which provides access to new spectral regions not possible with pentacene and ADT, and theoretically predicted improvement in mobility [45].

3.1.2 Hexacenes

Until recently, hexacene has been considered to have poor solubility and to be unstable in solution and thus a non-viable option for solution deposited organic thin-films [46]. However, recent progress has been made to stabilize and solubilize hexacene by adding functional side groups to the backbone [47]. An empirical model

for engineering stable crystalline derivatives of large acenes by functionalizing the backbone with side groups that have a diameter between 35-50% of the length of the acene resulted from work by the Anthony and Wudl groups [47-49]. The large side groups are believed to protect the acene backbone from dimerization and photo-oxidation processes that make them unstable [49]. These discoveries have renewed the interest in functionalized hexacene and heptacene derivatives [50, 51]. However, to our knowledge, studies investigating the electrical properties of these larger-acene materials in thin-films have yet to be conducted.

In this chapter a study of the optical and photoconductive properties of fluorinated and non-fluorinated hexacene molecules functionalized with tricyclohexylsilylethynyl (TCHS) side groups is presented (Fig. 3.1(a)). The non-fluorinated hexacene-TCHS has a standard hexacene backbone (molecular formula $C_{26}H_{16}$) consisting of a six benzene ring chain, while the two fluorinated derivatives (hexacene-F4-TCHS and hexacene-F8-TCHS) have a hexacene backbone with either four or eight hydrogen atoms at the end of the benzene chain replaced with fluorine atoms (Fig. 3.1(a)). The replacement of hydrogen at the end of the acene backbone with fluorines has been shown to change the HOMO and LUMO energies (Fig. 3.1(b)), enhance crystallization, and improve stability of the molecules [52]. These materials were synthesized by John Anthony's group at the University of Kentucky [50]. For fluidity, the three hexacene derivatives will be referred to as 'TCHS', 'F4-TCHS', and 'F8-TCHS' throughout the remainder of this chapter.

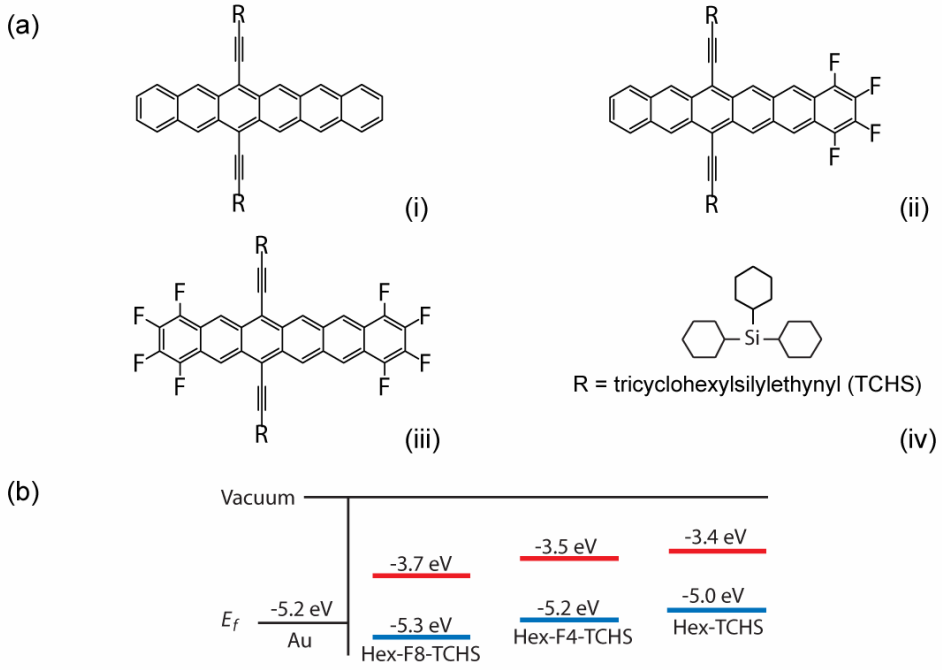

Figure 3.1: Molecular structures and HOMO-LUMO energies of the hexacene derivatives. (a) The molecular structures of the hexacene derivatives functionalized with tricyclohexylsilylethynyl (TCHS) side groups: (i) hexacene-TCHS (ii) hexacene-F4-TCHS, and (iii) hexacene-F8-TCHS. The molecular structure of the TCHS side group is also shown in (iv). (b) A diagram of the HOMO LUMO energies for the three hexacene-TCHS derivatives.

In the work presented here, for each of the three hexacene derivatives we explore the: (i) stability of the molecules in solution; (ii) conductive properties and steady state photoconductive properties under cw excitation in drop-cast films; and (iii) conductive and photoconductive stability of the drop-cast films. With this study we seek to examine how the addition of fluorine to the hexacene-TCHS backbone affects both the stability of the molecules in solution and their dark and cw photoconductive properties in thin-films, to determine the most promising of the three molecules for potential use in optoelectronic applications. In addition, we present

results from our collaborators for the performance of F4-TCHS in thin-film transistor and photovoltaic devices.

This chapter is organized as follows: Section 3.2 describes sample preparation and experimental methods. Section 3.3 presents and discusses results for optical properties, photostability, (photo)conductivity of the three derivatives. Section 3.4 briefly summarizes the study.

3.2 Experimental Methods

3.2.1 Sample Preparation

In all our experiments, both in solution and thin-film, hexacene-TCHS compounds were dissolved in de-oxygenated toluene. The toluene (JT, Baker, >99.7% purity) was de-oxygenated by boiling the solvent with nitrogen gas (~100 mL for ~ 1 hr). For experiments in solution, 0.1 mM solutions of hexacene-TCHS in de-oxygenated toluene were prepared in two steps. First a 1 mM concentration 'stock' solution was prepared and then diluted 10 fold to a 0.1 mM concentration. For drop-cast film preparation, higher concentration solutions (between 1 and 10 mM) were desired. While preparing the higher concentration solutions it was determined that the fluorinated compounds did not dissolve completely at concentrations above ~1 mM in de-oxygenated toluene. Upon this discovery, attempts were made to dissolve the fluorinated compounds in chlorobenzene and TCHF at these higher concentrations, and were unsuccessful. Films were drop-cast from solutions in toluene ranging in concentration from ~1 to 10 mM; in the case of the fluorinated derivatives, films, in

some cases, were prepared from solutions that were not completely dissolved. It was determined that drop-casting from solutions that were not completely dissolved did not dramatically affect film quality or (photo)conductivity in the fluorinated films.

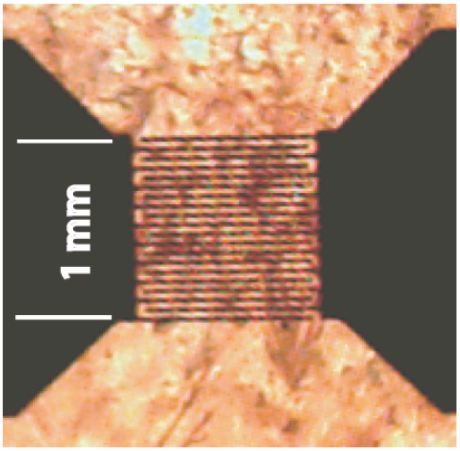

Figure 3.2: An image of the interdigitated electrode geometry on glass substrates that were used in conductivity measurements. The black area corresponds to the photolithographically deposited Au electrodes. The orange area corresponds to a deposited film (an ADT-TES-F film is shown).

Drop-cast films of all three compounds were prepared on glass substrates for absorption measurements, and on glass substrates with photolithographically deposited Cr/Au electrode pairs (either 5 nm/50 nm or 1 nm/50 nm thick) for conductivity measurements. An interdigitated electrode geometry, as shown in Fig. 3.2, was chosen over a simpler coplanar electrode geometry to provide a relatively large area of material (~1mm^2) to generate carriers in, while maintaining a 25 μm wide gap between electrodes. This is required to obtain the large electric fields, typically on the order ~10-100 kV/cm), needed to efficiently generate carriers in our materials at

applied voltages below 1kV. Each interdigitated electrode pair consists of 10 pairs of ~1mm long and 25 μm wide fingers that are separated by a 25 μm gap.

Films were typically drop-cast from 16 to 40 μL of solution onto a clean substrate on a hot plate at temperatures between 50^{o} and 60^{o} C. Substrates were cleaned in two steps: (i) the substrate was rinsed thoroughly with toluene then gently wiped clean with lens cleaning tissue (Thor Labs), and (ii) the substrate was thoroughly rinsed again with toluene and the remaining solvent dried using compressed air or nitrogen gas. While drop-casting the film, the solution was dispensed slowly as to control the solvent evaporation, such that the desired film area covered the electrode pairs. TCHS films tended to evaporate leaving films that appeared to be only slightly polycrystalline, almost 'amorphous like', in the center of evaporation, surrounded by a thicker, very polycrystalline film on the outer edge of the dispensed drop as the solvent evaporated. On the other hand, solutions of F4-TCHS and F8-TCHS were more difficult to make films with. The only consistent film coverage that could be achieved was the very polycrystalline film that formed at the evaporation edge of the dispensed drop of solution (as mentioned above with the TCHS). At the center of the very polycrystalline area, solvent evaporated such that noncontinuous clumps or 'islands' of agglomerated molecules were left behind. Thus, all films of F4-TCHS and F8-TCHS were prepared with the 'edge like' polycrystalline areas covering the electrodes.

3.2.2 Optical Absorption Measurements

For optical absorption measurements, samples were illuminated with fiber coupled light through a collimating lens, from a halogen lamp source (LS-1, Ocean Optics). The light that was transmitted through the sample was collected with a lens (Ocean Optics, 74-VIS) into a fiber, which coupled the transmitted light into an Ocean Optics USB2000, UV-VIS spectrometer (Fig. 3.3).

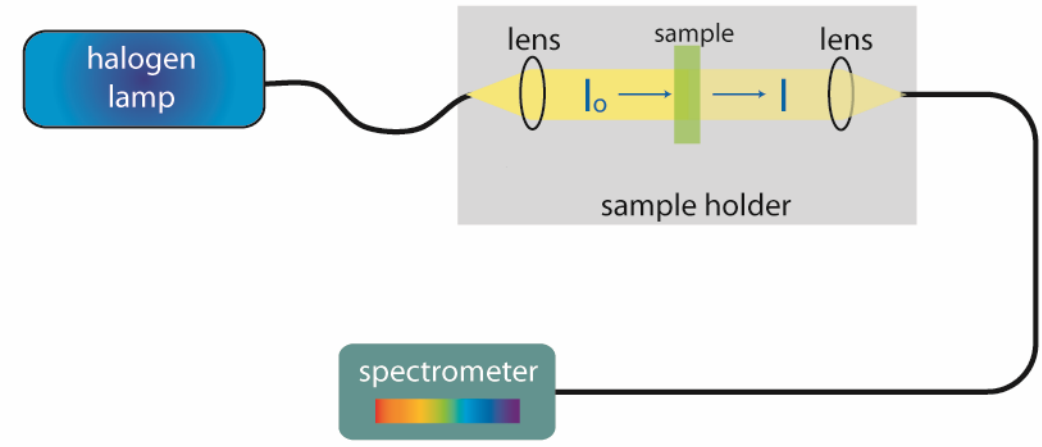

Figure 3.3: A diagram of the optical absorption experimental setup.

For each absorption measurement three spectral measurements were obtained: (i) the signal for the light transmitted through the sample, (ii) a dark/background signal, and (iii) a reference signal. Absorption was then calculated as absorbance with units of optical density (OD) using Beer's law

$$I = I_o \cdot 10^{-OD} \qquad (3.1),$$

where I_o is the intensity of the light into the sample from the halogen lamp, I is the intensity of the light transmitted through the sample, and OD is the optical density.

From Beer's law the optical density can be solved for and related to the experimental measured signals, as follows:

$$OD = -\log\left(\frac{I}{I_o}\right) = -\log\left(\frac{transmission - background}{reference - background}\right) \qquad (3.2).$$

For optical absorption measurements in solution, the solutions were prepared as described in the previous section. The 0.1 M solutions were placed in $1cm^2$ optical grade glass cuvettes (New Era, NE-23-G-10). The cuvettes were placed in a cuvette holder (Ocean Optics, CUV) with fiber and lens mounts to improve measurement reproducibility. De-oxygenated toluene in a similar optical grade cuvette was used as a reference. For measurements in films, the films were prepared on glass substrates, as mentioned above, and placed on a custom made sample holder, which contains both fiber and lens mounts. A clean blank glass substrate was used as a reference in these measurements.

3.2.3 Photoluminescence (PL) Measurements

In our measurements, although phosphorescence is expected to be minimal, at best, based on photoluminescence lifetime measurements, strictly speaking we can not resolve fluorescence emission from phosphorescence emission in our spectral measurements. Thus, we refer to emission from our samples as photoluminescence. Photoluminescence was excited in our experiments with either 633 nm (helium-neon, Melles Griot) or 532 nm laser light (Nd:YVO4, Coherent). The excitation source is focused onto the front of the sample using a lens (L1) and the photoluminescence

emission is coupled into the detection path (shown in red) using a parabolic mirror (Fig. 3.4). The emission is then focused (L2) through an alignment iris, and is collimated and refocused, using a lens pair (L3 and L4), into a 600 μm fiber (Ocean Optics, P600-2-600-UV-VIS) that is connected to a spectrometer (Ocean Optics, USB2000, UV-VIS). The spectrometer was calibrated with a 3100 K blackbody emitter. For measurements both in solution and film, samples were mounted in custom made sample holders.

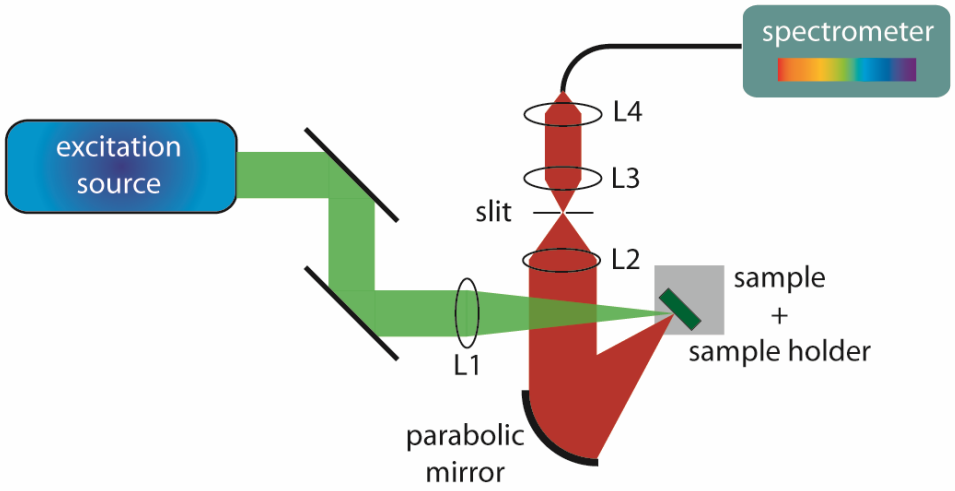

Figure 3.4: A diagram of the photoluminescence experimental setup.

3.2.4 Dark and Cw Photocurrent Measurements

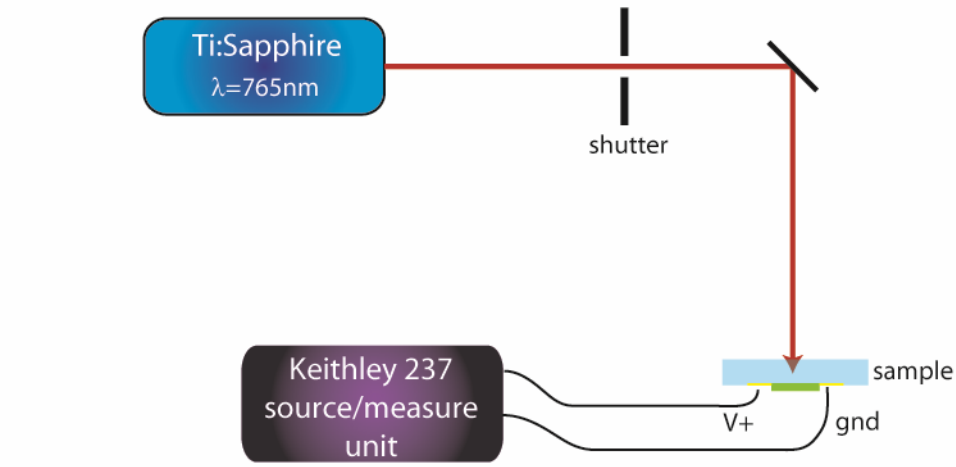

Figure 3.5: A diagram of the experimental setup for dark and photocurrent measurements as a function of voltage.

For dark and photocurrent experiments, voltage was applied to samples and current measured simultaneously with a Keithley 237 source/measure unit (Fig. 3.5). Data acquisition with the Ketihley was automated with a custom made LabView program, which provided the ability to systematically control the voltage applied to the sample during current measurements. Samples (drop-cast films on Au electrodes, *Section 3.2.1*) were mounted on a custom made sample holder. Photocurrent was excited using a cw titanium-sapphire laser (Kapteyn-Murnane Labs) tuned to λ~765 nm at an intensity of ~190 mW/cm^2. Samples were back-illuminated (Fig. 3.5), assuming that a majority of the excited carriers would be generated in the volume of the film between the 50 nm thick Au electrodes where the electric field is strongest. In addition, back illumination reduces the unwanted effect of excitation intensity

reduction due to absorption in the film outside of the volume of greatest importance for photocurrent generation. The excitation light was shuttered to reduce photo exposure of the sample between measurements. Photocurrent was considered to be the current measured under excitation minus the dark current. In addition, dark current was always measured before photocurrent, as the existence of trapped photogenerated carries can result in inaccurate dark current values.

3.3 Results and Discussion

3.3.1 Photostability in Solution

As discussed above the stability of hexacene molecules in powder and solution is of importance, if hexacene is to be considered a viable material for use in electronic applications. With this in mind, we started our study by exploring the stability of the hexacene-TCHS derivatives. To quantifiably compare the stability of the three derivatives, absorption and PL of the molecules in solution were monitored over time. Optical absorption and PL spectral data of the three hexacene-TCHS molecules in freshly prepared toluene solutions, from freshly synthesized powder are shown in Fig. 3.6. It can be seen from the data that the hexacene-TCHS molecules have an S_1 absorption band between λ~550-800 nm. The spectral features at λ<550 nm are most likely due to absorption from decomposition products of the hexacene molecules [50]. In addition, the fluorination of the hexacene backbone introduces a slight blue shift in absorption and PL spectra (~6nm in TCHS-F4 and ~12 nm in TCHS-F8 relative to TCHS).

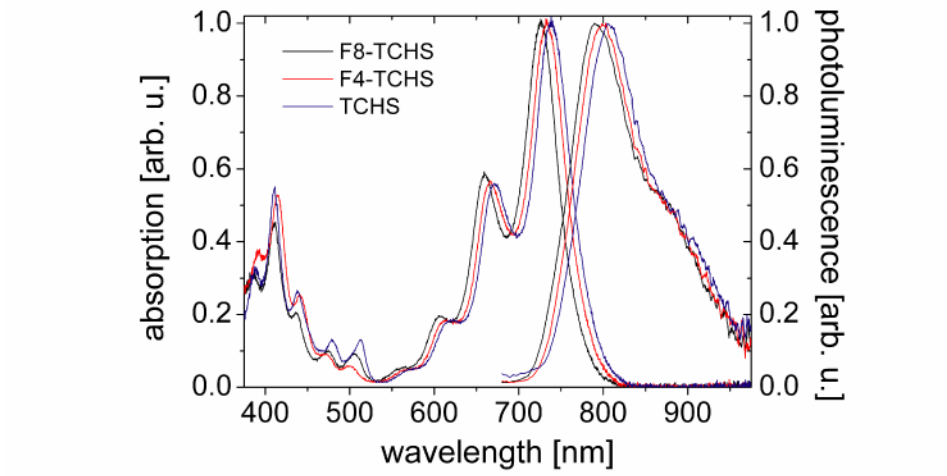

Figure 3.6: Optical absorption and photoluminescence spectra of hexacene-TCHS (blue), hexacene-F4-TCHS (red), and hexacene-F8-TCHS (black) in solution.

To monitor the photostability in solution, solutions of TCHS, F4-TCHS, F8-TCHS molecules in de-oxygenated toluene were prepared (see *Section 3.2.1* for details). Each solution was then aliquoted into two cuvettes (six total). Optical absorption and photoluminescence measurements were taken from each of the solutions immediately after preparation (at 't=0'). One solution of each of the compounds was then exposed to fluorescent light, in a fume hood, while the second solution of each compound was stored in the dark, as a control. Subsequent absorption and photoluminescence measurements were then taken at either 30 or 60 minute time intervals, depending on the rate that the solutions photobleached. The optical absorption and photoluminescence data in Fig. 3.7 (a) and (b), respectively, show the results for a F8-TCHS solution, which proved to be the most photostable derivative. Optical absorption and photoluminescence spectral data for the control solution are also included in Fig. 3.7 for comparison. It can be seen from the data that

the degradation of the photoresponse of F8-TCHS molecules in solution was due to exposure to light. Similar spectra were obtained for F4-TCHS and TCHS (not shown), with relatively faster photobleaching observed in the partially fluorinated and non-fluorinated derivatives as compared to F8-TCHS, such that the photostability of F8-TCHS > F4-TCHS > TCHS.

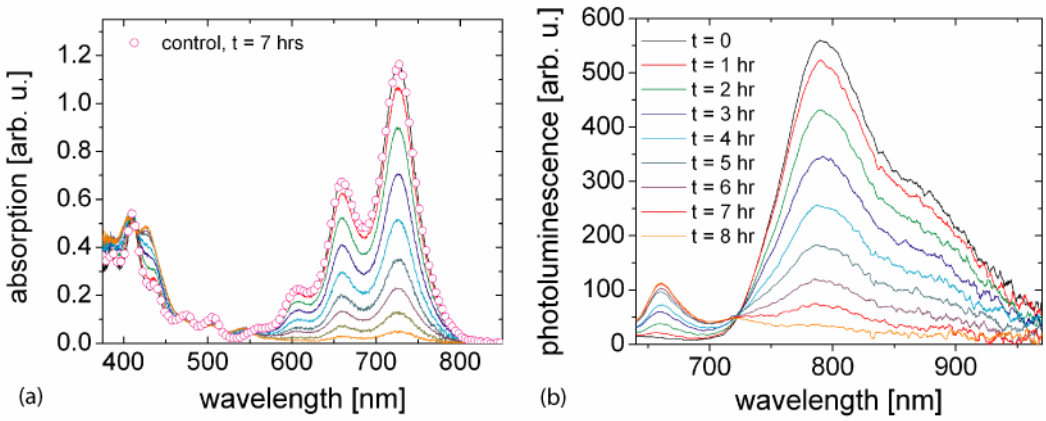

Figure 3.7: (a) Optical absorption and (b) PL spectra of F8-TCHS in toluene. Measurements were taken at one hour intervals with the solution exposed to fume hood lighting between measurements to monitor photostability. As a control, absorption measurements were taken on a similar solution that was stored in the dark.

To compare the photostability of the three derivatives, optical absorption spectra for each derivative at each time point was integrated from λ=640 to 824 nm. For each hexacene compound, the integrated absorption at each time point was then normalized to that of the 't=0' time point (Fig. 3.8). By comparing the approximate half-lives of the three compounds it was observed that F8-TCHS was ~ 1.5 (~3.0) more photostable than F4-TCHS (TCHS).

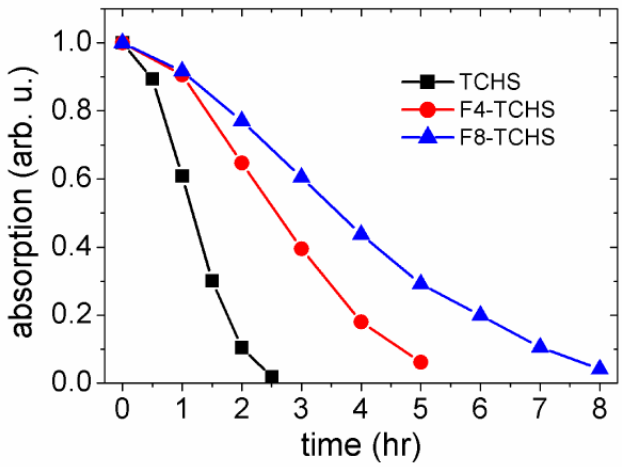

Figure 3.8: Integrated optical absorption spectra (640nm < λ < 824nm) as a function of light exposure time for TCHS, F4-TCHS and F8-TCHS (lines connecting data points added for clarity). The addition of fluorine to the acene backbone increased the photostability in solution, with compound F8-TCHS being the most stable.

3.3.2 Stability of Hexacene-TCHS Powders

To study the stability of the three hexacene derivatives in powder form, the compounds were stored in vials under ambient conditions in the dark. Solutions of the molecules in toluene where prepared at different time intervals during storage (as described in *Section 3.2.1*). Optical absorption measurements were conducted to monitor and compare the stability of the three hexacene derivatives. An example of data from measurements taken after ~1 and 3 months of storage, for F8-TCHS and TCHS are shown in Fig. 3.9. It can be seen from the data that the fluorination of the hexacene backbone also increases the stability of the compounds in powder form. We found that the fully fluorinated hexacene was more stable than the partially fluorinated (not shown) and the non-fluorinated, such that the stability of F8-TCHS > T4-TCHS >

TCHS (similar to solution). In particular, essentially no powder degradation was observed in compound F8-TCHS.

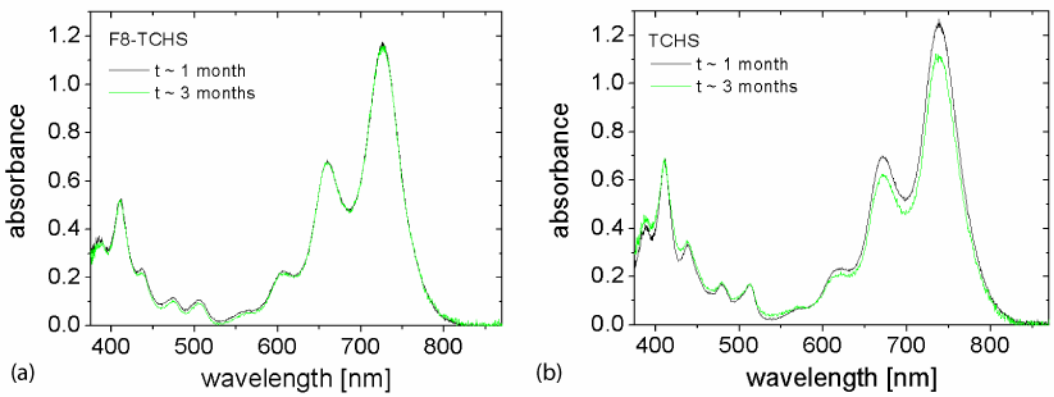

Figure 3.9: Optical absorption spectra of (a) F8-TCHS and (b) TCHS in toluene. Spectra were measured in freshly made solutions of powders stored for ~1 month and ~3 months after synthesis. Compounds were stored in the dark at room temperature in air between measurements. The addition of fluorine to the acene backbone increased the stability, such that the stability of F8-TCHS > F4-TCHS > TCHS.

3.3.3 Conductivity of Hexacene-TCHS Thin-Films

Given that the hexacene-TCHS derivatives were relatively stable, we pursued a study comparing the conductivity of these materials. To determine both the dark and photoconductivity, films were prepared and currents measured as a function of voltage (as discussed in *Section 3.2*). In our study, dark and photocurrents were measured at voltages between 10 and 150 V (4 kV/cm and 60 kV/cm) with λ=765nm excitation at an intensity of ~190 mW/cm^2. Data showing the largest dark and photocurrent values obtained for each material is presented in Fig 3.10. In our experiments dark currents ranged from ~140 to 325 nA, ~3.6 to 11.5 μA, and ~270 to 900 nA for TCHS, F4-TCHS, and F8-TCHS respectively; while photocurrents in our films ranged from ~100

to 800 nA, ~5.4 to 9.4 μA, and ~ 100 nA to 6.7 μA for TCHS, F4-TCHS, and F8-TCHS respectively. Although all three hexacences exhibited photoresponse, the F4-TCHS films had the best conductivity, as the F4-TCHS films consistently exhibited both dark and photocurrents in the μA regime. It should be noted that despite the data shown in Fig 3.10, which was the one instance where currents in the μA regime were measured in F8-TCHS films, dark and photocurrents in TCHS and F8-TCHS films were on average at least an order of magnitude smaller than in F4-TCHS films.

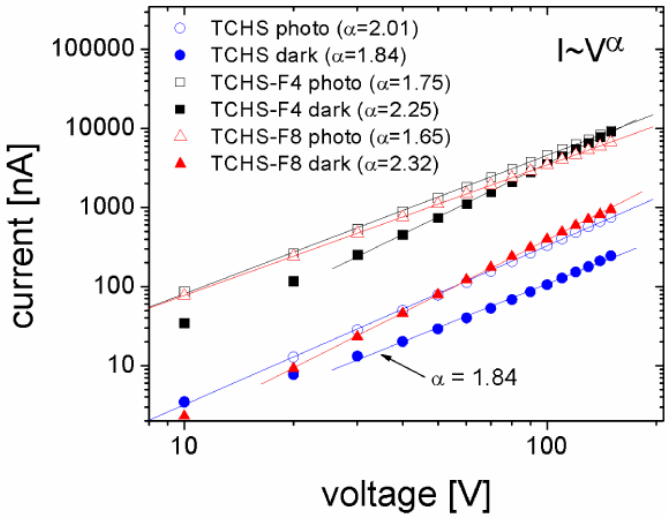

Figure 3.10: Dark and photocurrents in TCHS, F4-TCHS and F8-TCHS thin-films as a function of applied voltage. Power law ($I \sim V^{\alpha}$) fits to the data are also shown.

From power law fits to the current versus voltage data ($I \sim V^{\alpha}$), also shown in Fig. 3.10, we, on average, observed a voltage dependence of $\alpha \sim 2$ (i.e. $\alpha \sim 1.84$ for dark current in F4-TCHS, as shown in Fig. 3.10). This suggests that space-charge limited currents (SCLC) were predominant in the hexacene films. The SCLC are a result of efficient hole injection from the Au electrodes (as expected from the HOMO

energies of the three compounds (Fig. 3.1(b)) causing a build up of charge at one of the electrodes. The charge build up results in a non-uniform potential across the electrode gap, and can be described by a voltage squared dependence of the current [53].

To quantitatively access the performance of the three hexacene derivatives we calculated the mobility in the films from the SCLC data ($I_d \sim V^2$). The data was expressed as a current density in units of A/m, assuming that the current in our planar electrode geometry flows along a thin layer of unknown thickness, and plotted as a function of voltage squared (Fig 3.11). Although there is no analytical solution for the j-V relationship in a film of finite thickness, as in our films, we were able to obtain lower (an infinite thin-film) and upper bounds (in the infinite half space) for the SCLC mobility, μ, by fitting these data to the following equations [54]

thin film: $$j = \frac{2\mu\varepsilon\varepsilon_o}{\pi}\left(\frac{V}{L}\right)^2 \qquad (3.3)$$

half space: $$j = 0.28\mu\varepsilon\varepsilon_o\left(\frac{V}{L}\right)^2 \qquad (3.4).$$

Here L is the gap between the electrodes, ε is the relative dielectric constant of the film, ε_o is the dielectric permittivity of vacuum, and V is the voltage applied to the sample. In our calculations we assumed a value of ε =3.5 for all films [55]. As expected, from the dark current density values, the SCLC mobility in F4-TCHS films was much larger than in films of F8-TCHS and TCHS (results are summarized in

Table (3.1)). In the thin-film approximation, the estimated lower bound for the effective charge carrier mobilities are 8.4 x 10^{-3} cm^2/Vs, 6.9 x 10^{-4} cm^2/Vs, and 1.7 x 10^{-4} cm^2/Vs for F4-TCHS, F8-TCHS, and TCHS respectively. It should be noted that, given the voltage range of our experiments, which is not likely to generate currents in the trap-filled regime [27], and that our substrates were not treated [21], these effective values could be more than a factor of ~10 lower than what is possible in these materials in solution deposited films (e.g. see mobility values obtained from field effect transistor devices in *Section 3.4*).

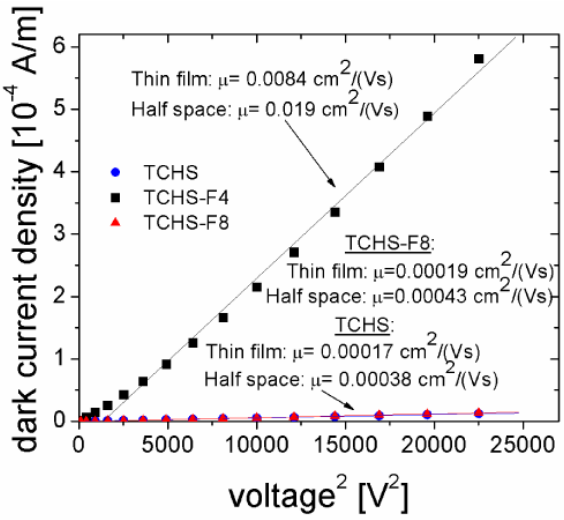

Figure 3.11: Dark current density TCHS, F4-TCHS, and F8-TCHS thin-films as a function of voltage squared. Linear fits, from which SCLC effective charge carrier mobilities were calculated, are also shown.

	μ, thin-film (cm^2/(V s))	μ, half-space (cm^2/(V s))
TCHS	$1.7x10^{-4}$	$3.8x10^{-4}$
F4-TCHS	$8.4x10^{-3}$	$1.9x10^{-2}$
F8-TCHS	$6.9x10^{-4}$	$1.6x10^{-3}$

Table 3.1: Thin-film and half-space effective charge carrier mobilities in films of the hexacene-TCHS derivatives.

3.3.4 Stability in Thin-Films

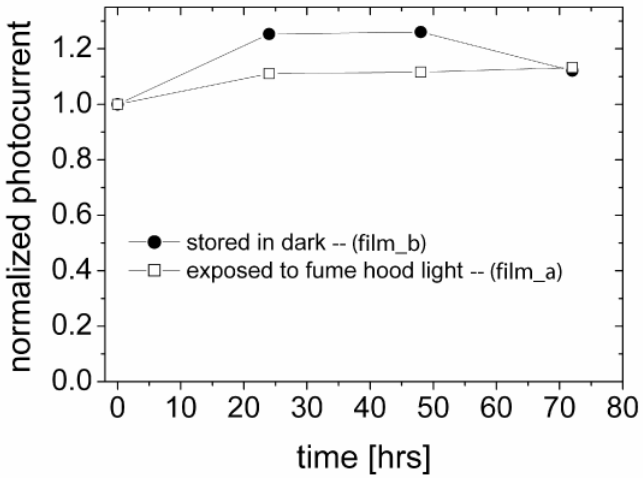

Figure 3.12: Photocurrent measured in F4-TCHS under 765 nm photoexcitation at 150 V, normalized by its value at t = 0 (freshly prepared film). Measurements were taken at ~24 hr intervals after film preparation to monitor film photostability. Between measurements, both films were stored in air. Film_a was stored under fume hood lights and film_b was stored in the dark, as a control.

Given the relatively superior photoresponse in F4-TCHS films, we studied the photostability of these films by conducting dark and photocurrent measurements at 24 hour intervals after film preparation (t=0). Between measurements, films were stored in ambient conditions either exposed to fumehood lights (film_a) or in the dark (film_b) (Fig. 3.12). At each 24 hour time point, dark and photocurrent were measured as a function of voltage (as described above). The data in Fig. 3.12, shows

the photocurrent at 150V (60 kV/cm), normalized to that at t = 0. Degradation in photocurrent was not observed in either film over the 72 hour time period, suggesting that the photostability is improved in the solid state as compared to in solution, which is consistent with what was observed in the powder form of the hexacene compounds (*Section 3.3.2*). Values greater than 1 are attributed to experimental error. The additional stability in film as compared to that in solution is promising for device applications.

3.4 Device Characterization of Hexacene-F4-TCHS

Following the initial optoelectronic characterization, our collaborators, conducted device characterization of the stable F4-TCHS derivative, which exhibited the highest mobility and photocurrent, in bottom-contact field-effect transistors (FETs) and in a bulk heterojunction photovoltaic cell. The FET devices were prepared, and measurements conducted, by our collaborator Dr. Oana Jurshecu at Wake Forest University. The photovoltaic cells were fabricated, and measurements conducted, by our collaborator Dr. George Malliaras at Cornell University. Results from these studies are presented here for completeness.

The FETs were fabricated from F4-TCHS on SiO_2 gate-dielectric and chemically modified Au contacts (Fig. 3.13(a)). Heavily doped Si was used as the gate electrode and 300 nm of thermally-grown SiO_2 at its surface served as gate dielectric. Ti/Au source and drain contacts were deposited by e-beam evaporation, and were treated with pentafluorobenzene thiol (PFBT) to enhance the crystallization of the fluorinated semiconductor [20]. The organic semiconductor was drop-cast from a

0.2 wt% chlorobenzene solution, and the solvent was allowed to evaporate slowly in a covered Petri dish in the dark for two to three days [56]. Figure 3.13(b) shows an optical micrograph of the crystalline films obtained by this process; the large, leaf-shaped crystals span the channel of the transistor, with crystal dimensions ranging from a few μm to hundreds of μm. The FETs fabricated in this fashion were measured under ambient conditions, and over 100 devices were sampled to yield hole mobility ranging from 0.01 to 0.10 cm^2/Vs. The variability arises from differing crystal quality along with the natural anisotropy present in these π-stacked systems [57]. Mobilities were calculated in the saturation regime, and Fig. 3.13(c) shows the transfer characteristics (log (I_D)) right axis and $\sqrt{I_D}$ left axis versus gate voltage V_{GS}) for the device shown in Fig. 3.13(b), demonstrating a mobility of 0.1 cm^2/Vs and on/off current ratio of 10^5. For mobility calculations, the channel width was defined as the portion of the channel covered by the crystals.

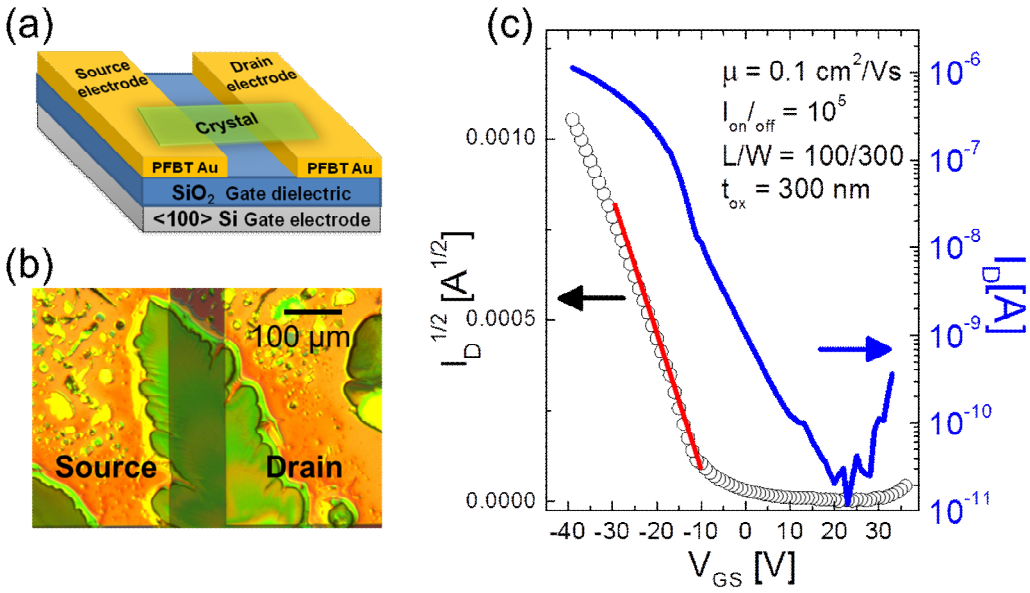

Figure 3.13: Hexacene-F4-TCHS based field-effect transistors (FET) fabricated by Dr. Oana Jurchescu at Wake Forest University. (a) Schematic representation of the FET geometry. (b) Top-view optical image of a device. (c) Evolution of the drain current, I_D, with the gate voltage, V_{GS}, for the same device.

The LUMO level estimated for F4-TCHS (3.5eV) suggests application as an acceptor in conjunction with poly(3-hexylthiophene) (P3HT) donor (3.3eV) in a bulk heterojunction photovoltaic cell. A 1:1 blend by weight of P3HT and F4-TCHS in toluene (20 mg/mL) was spin-cast onto PEDOT-PSS treated, patterned ITO electrodes on a glass substrate, and a CsF/Al cathode was evaporated through a shadow mask to define the photovoltaic cell. Under AM 1.5 illumination, the cell provided an open-circuit voltage of 0.3 V, short-circuit current density of 0.36 mA/cm^2, fill factor of 31%, and an overall power conversion efficiency of 0.034%. The performance was relatively poor. However, the purpose of this experiment was to demonstrate that hexacenes could be made suitably stable for exploration in this particularly demanding application. With that goal in mind, hexacene F4-TCHS performed admirably. The

absorption of light by hexacene into the near-infrared clearly contributed to the current output of the device, as shown by the external quantum efficiency plot in Fig. 3.14. More importantly, the device performance did not degrade appreciably when the device was exposed to intense AM 1.5 illumination under nitrogen atmosphere for 10 minutes, allowing unhurried characterization of the solar cell. While this particular hexacene derivative did not perform well as an acceptor, the appropriate LUMO energy, absorption beyond 1.5eV and reasonable photostability bodes well for future photovoltaic studies, provided appropriate film morphology and crystal packing can be achieved.

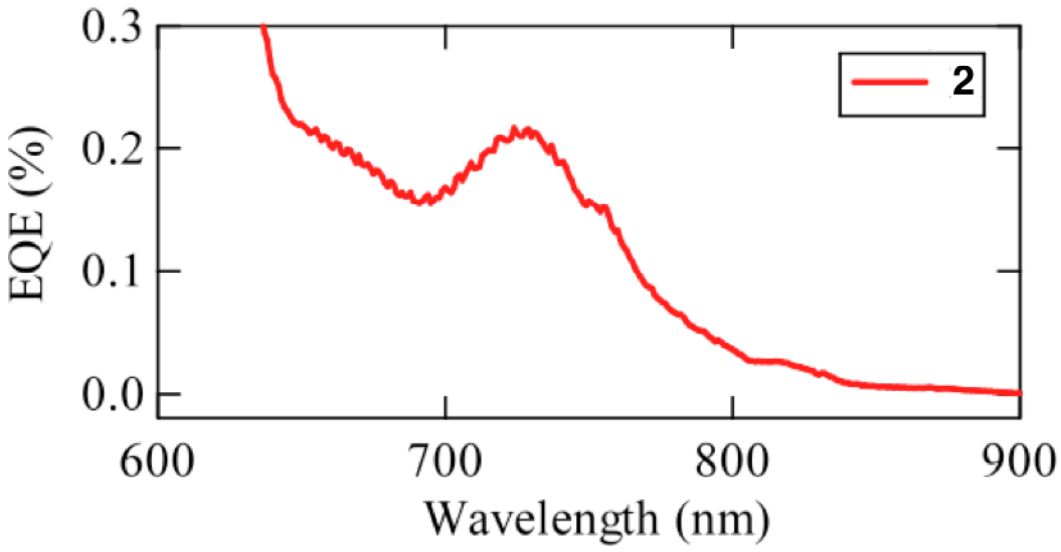

Figure 3.14: External quantum efficiency (EQE) obtained from a photovoltaic device fabricated by Dr. George Malliaras at Cornell University. The EQE data displays the long-wavelength portion of the power spectrum from a hexacene-F4-TCHS based photovoltaic, showing the contribution of the hexacene chromophore to the photocurrent.

3.5 Conclusion

We have demonstrated that hexacene can be made both sufficiently soluble and stable for studies in electronic devices. From stability studies it was determined that fluorination of the hexacene backbone added to the stability of the material, such that F8-TCHS was a factor of ~3.0 times more stable than TCHS. In addition, the partially fluorinated, F4-TCHS, derivative proved to be the most (photo)conductive of the three derivatives in drop-cast films. A lower bound value of the mobility (~8.4 x 10^{-3} cm^2/Vs) was obtained from SCL currents in a F4-TCHS drop-cast film on untreated electrodes. These results prompted the use of the F4-TCHS derivative in FET and photovoltaic devices. While performance in both thin-film transistors and photovoltaics was not as impressive as previous results reported for a variety of pentacene derivatives, this first-ever device study of hexacene derivatives yielded promising initial results. For example, FET mobilities as high as ~ 0.1 cm^2/Vs were obtained from F4-TCHS based devices. Optimization of both materials and processing conditions will be required to determine if stability and material performance can be achieved.

4. Temperature Dependence of Exciton and Charge Carrier Dynamics in Organic Donor-Acceptor Composite Films

4.1 Introduction

Organic (opto)electronic materials are of interest due to their low cost and tunable properties [8, 58]. Solution processable materials that can be cast into thin-films using various solution deposition techniques are especially advantageous [59]. For example, functionalized anthradithiophene (ADT) derivatives have recently been utilized in thin-film transistors (TFTs) [52] and solar cells [60, 61]; additionally, ADTs are promising for applications in photodetectors, light-emitting diodes, and lasers.

A promising venue for developing new materials with optoelectronic properties, fine-tuned for particular applications, is designing composites materials. Such materials can have charge transfer properties resulting in composites that have dramatically different optical and electronic properties than the pristine materials that make up the composite. These processes, become possible in composites by choosing two pristine materials, referred to as donors (D) and acceptors (A), with appropriate HOMO-LUMO levels. For example, if the energy of the acceptor is lower than that of the donor then it becomes energetically favorable for photoinduced electron transfer from the donor to the acceptor at the donor/acceptor (D/A) interface (Fig. 4.1) [62, 63]. In the case of solution-processable organic materials, bulk- heterojunctions (BHJ) can be achieved in composites, where D/A interfaces occur throughout the material. Such, BHJ composite systems have shown improved performance over pristine films,

and, for example, have been utilized in solar cells [64] and photodetectors [65] due to enhanced charge carrier photogeneration.

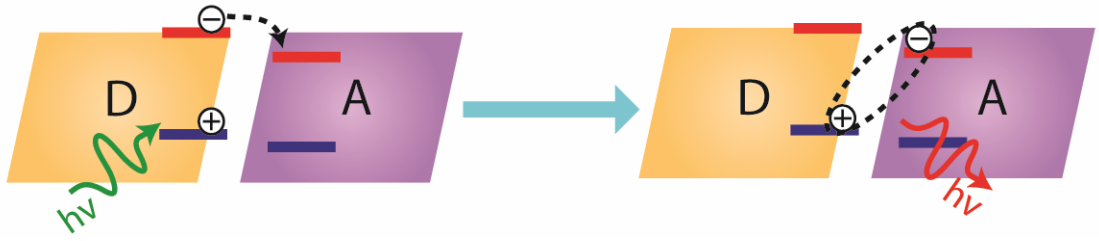

Figure 4.1: Diagram depicting exciplex formation. The electronic excitation on the donor is followed by charge transfer (CT) of the electron from the donor to the acceptor to form a bound emissive exciplex.

Previous studies by our group, on small molecule organic semiconductor composite films, with a fluorinated ADT, functionalized with triethylsilylethynyl (TES) side groups (ADT-TES-F), as the donor material have shown very interesting results. From these studies it was determined that D/A interactions can dramatically affect exciton and charge carrier dynamics typically observed in pristine ADT-TES-F films. In addition, substantially different charge carrier dynamics were observed between ADT-TES-F based composites with different acceptor molecules. These differences in charge carrier dynamics were due to the efficiency of the photoinduced charge transfer between donor and acceptor molecules. For example, composites with a second anthradithiophene functionalized with triisopropylsilylethynyl (TIPS) side groups and cyano end-groups (ADT-TIPS-CN, Fig. 4.2(a)) as an acceptor exhibited 'partial' charge transfer that lead to exciplex formation (an emissive bi-molecular exciton shared between donor and acceptor molecules) and a slow photogeneration process (~20ns) [39, 40]; while composites with C_{60} acceptors (Fig. 4.2(a)) displayed

'complete' charge transfer to charge separated states that resulted in a pronounced increase in charge carrier photogeneration on ps time-scales, followed by enhanced charge carrier recombination on ns time-scales [39]. Although, these earlier studies identified complex interactions contributing to optoelectronic properties of these composites, these interactions are still not well understood.

In this chapter, previous work on ADT-TES-F based composites with ADT-TIPS-CN and C_{60} molecules as acceptors is expanded on. In particular, the physical mechanisms that determine optical absorption, PL, and photoconductive properties of these composites are presented. These particular composites serve as model systems for a physical study of the effects of complete and partial charge transfer processes on exciton and charge carrier dynamics in ADT-TES-F-based films. Specific questions to be addressed include: (i) does charge carrier photogeneration rely on dissociation of the exciplex, (ii) what is the role of D/A charge transfer in charge carrier photogeneration and PL emission, and (iii) is charge transport in these composites hopping like or bandlike.

In order to establish the physical mechanisms outlined above, we performed a study of the temperature and electric field dependence of the optical absorption, PL, and transient photocurrent in composite films, from which we sought a physical model that would be consistent with all experimental observations. The chapter is organized as follows: In Section 4.2 sample preparation and experimental methods are described. In Section 4.3 analysis of optical absorption, PL, and photoconductive properties of ADT-TES-F/ADT-TIPS-CN and ADT-TES-F/ C_{60} composite films as a

function of temperature are presented. In Section 4.4 results are discussed further and a physical picture of exciton and photoinduced charge carrier dynamics in these composites is presented. In Section 4.5 the findings are summarized.

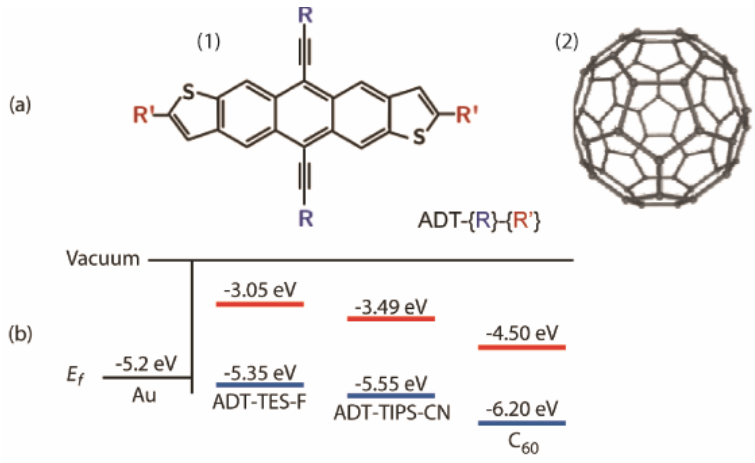

Figure 4.2: Molecular structures of donor and acceptor molecules: (a.1) Molecular structures of donor molecule ADT-TES-F (R = TES, R' = F), and the acceptor molecule ADT-TIPS-CN (R = TIPS, R' = CN). (a.2) Molecular structure of the acceptor molecule C_{60}. (b) HOMO and LUMO energy levels of all three molecules.

4.2 Materials and Experimental Methods

4.2.1 Materials

In this study, the high performance ADT-TES-F was used as the donor material. This ADT derivative was chosen, given that it has high charge carrier (hole) mobilities (e.g. > 1.5 $cm^2/(Vs)$ in spin-cast thin-films on treated electrodes [20, 21]), high photoconductive gain, and relatively strong photoluminescence in solution deposited thin-films [37, 38]. As discussed above, the acceptor molecules chosen for this study are ADT-TIPS-CN and C_{60}. HOMO and LUMO energy levels for all three derivatives are shown in Fig. 4.2(b). The energy values for ADT-TES-F and ADT-

TIPS-CN molecules were obtained by differential pulse voltammetry experiments conducted by our calibrator, who synthesized the compounds, Dr. John Anthony at the University of Kentucky [50, 52]; those for C_{60} were taken from Ref [66].

4.2.2 Sample Preparation

For preparation of pristine ADT-TES-F films, a 20 mM toluene solution was used. For ADT-TES-F/ADT-TIPS-CN blends, a composite solution of ADT-TES-F (98 wt%) with ADT-TIPS-CN (2 wt%) in toluene was prepared from a 20 mM stock solution of ADT-TES-F and a 1 mM stock solution of ADT-TIPS-CN. For similar wt/wt ratio ADT-TES-F/C_{60} films, a composite solution of ADT-TES-F (98 wt%) with C_{60} (2 wt%) was prepared from stock solutions of 20 mM and 3.5 mM, respectively. The low concentration of acceptor molecules was chosen to minimize the disruption of film crystallinity [67] and thus a reduction in hole mobility. Additionally, this enabled us to relate the photocurrent dynamics to properties of the CT states, while neglecting effects of acceptor domain formation and electron mobility in the acceptor domains [68]. Solutions were spin-cast at 4000 rpm onto glass substrates with photolithographically deposited 5 nm/50 nm thick Cr/Au interdigitated electrode pairs (*Section 3.2.1*, Fig. 3.2). Electrodes consisted of 10 pairs of 1 mm long fingers with 25 μm finger width and 25 μm gaps (*L*) between the fingers of opposite electrodes. After film deposition, samples were allowed to sit on the hotplate at 45^{o}-50^{o} C for ~30 min and then placed in a closed Petri dish overnight to promote residual solvent evaporation. This preparation method resulted in polycrystalline films, as confirmed by x-ray diffraction (XRD) from a pristine ADT-TES-F film [35].

4.2.3 Optical Absorption and PL Measurements

Absorption and PL were measured under vacuum, in a custom made liquid nitrogen cryostat. The absorption spectra were measured using an Ocean Optics USB4000 spectrometer and a halogen white light source (3100 K blackbody). The lamp was fiber delivered to a collimating lens focused into the cryostat on the active region of the sample and some of the surrounding area (~2 mm diameter); with illumination occurring on the substrate side of the film. Light transmitted through the sample was collected through a second collimating lens and coupled by fiber to the spectrometer. For the reference signals, the cryostat was translated so as to illuminate an empty region (free of the film and of electrodes) on the glass substrate.

PL was excited with a 355 nm frequency-tripled Nd:YAG laser, using excitation conditions similar to those utilized in the photocurrent measurements (*Section 4.2.4*), and detected with a second fiber coupled spectrometer (Ocean Optics USB2000) calibrated with a 3100 K blackbody emitter; with sample illumination occurring on the substrate side. It should be noted that, the independence of the PL spectra in ADT derivatives on the excitation wavelength at wavelengths above the absorption edge has been previously verified [38]. This is brought to the readers attention to validate references made to any previous work by our group, at 532 nm excitation. For measurements under applied electric field (E), voltage was applied to samples using a Kiethley 237 source/measurement unit. The average E-field was calculated using E=V/L, where L is the gap between the electrodes. This calculation is

made assuming that the field was approximately constant in the region of the film directly between the electrodes, where a majority of absorption occurs within the film.

4.2.4 Transient Photocurrent Measurements

Transient photocurrent measurements were also conducted in the custom made cryostat, under 355 nm, ~500 ps, 0.4 μJ/cm^2 pulsed excitation (Nd:YAG laser, 44.6 kHz repetition rate, from Nanolase). Voltage (*V*) was applied to the samples using a Keithley 237 source-measure unit, and the transient photocurrent was measured using an Agilent DSO6032A oscilloscope [34, 37-39]. The time resolution was ~500 ps, limited by the laser pulse width. As with absorption and PL measurements, the average E-field applied to samples was calculated using $E = V/L$, where L is the gap between the electrodes.

4.3 Experimental Results

4.3.1 Optical Absorption and PL in Composites

An optical absorption spectrum from a spun-cast pristine ADT-TES-F film at a temperature of 298 K is shown in Fig. 4.3(a). The optical absorption in ADT-TES-F exhibited S_1 absorption between λ~400 and 600 nm, with a vibronic progression of ~1360 cm^{-1}; and peak absorption corresponding to the S_0 –> S_1 0-0 transition at ~550 nm. PL spectra in the same pristine ADT-TES-F film, at multiple temperatures between 100 and 350 K, are shown in Fig. 4.3(b). The PL spectra at 298 K, is consistent with previous results, having emission between λ~550 and 800 nm and pronounced vibronic structure. Sample to sample variation resulted in similar optical

absorption and PL spectra, but with changes in the relative vibronic peak heights, which has been attributed to differences in morphology and disorder in films [35, 69]. These results are also consistent with those obtained in previous studies of the optical absorption and PL in pristine ADT-TES-F films [38, 41]. A detailed discussion of the temperature dependence on the optical absorption and PL properties in these spun-cast pristine ADT-TES-F films is presented in Ref [35].

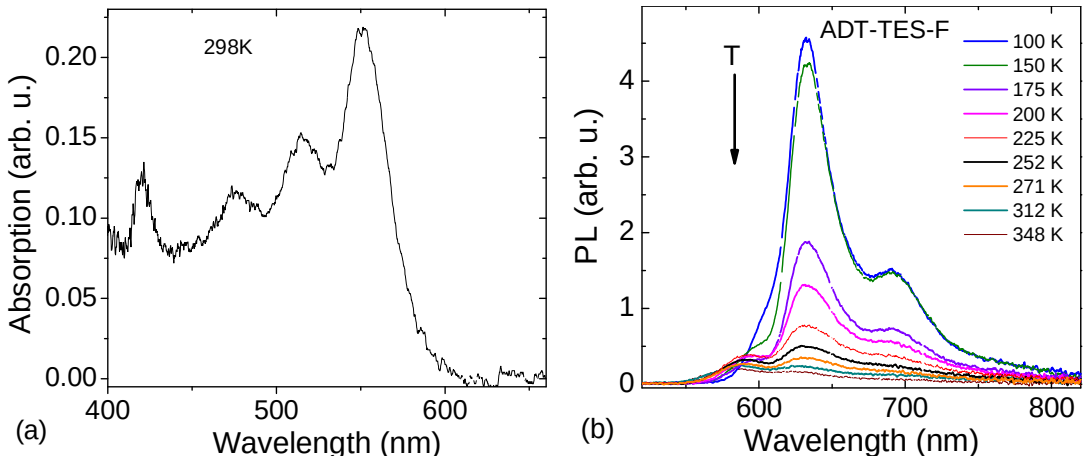

Figure 4.3: (a) Absorption spectra at 298K and (b) PL spectra at multiple temperatures in a pristine ADT-TES-F film.

With the addition of C_{60} to ADT-TES-F, in composite films (ADT-TES-F/C_{60} (2%)), optical absorption spectra did not change. Spectra were similar to those of pristine ADT-TES-F films in Fig. 4.3(a), indicative of no significant ground-state interaction (charge transfer) between the ADT-TES-F and C_{60} molecules (i.e. direct absorption from the ground state of the donor to the acceptor). However, PL quantum yield (QY), which is the ratio of emitted photons to absorbed photons, was about a factor of ~10 lower than that in pristine ADT-TES-F films under the same conditions. The PL QY quenching in fullerene-containing composites has been reported in various

conjugated polymer/fullerene blends and attributed to ultrafast photoinduced electron transfer from the donor (polymer) to the acceptor (fullerene) molecules [70]. As was previously observed in ADT-TES-F/C_{60} composites [39], we attribute the reduction in QY in these samples to a similar photoinduced electron transfer process, with C_{60} acting as a strong acceptor in these films. The spectrum of the residual PL emission in ADT-TES-F/C_{60} composites (which has not been quenched via photoinduced electron transfer) and its temperature dependence were identical to those of the pristine ADT-TES-F films in Fig. 4.3(b), confirming the sole contribution of ADT-TES-F in the PL properties of ADT-TES-F/C_{60} films.

Optical absorption spectra of ADT-TES-F/ADT-TIPS-CN (2%) films were also similar to those from pristine ADT-TES-F films in Fig. 4.3(a), and no significant ground-state charge transfer was observed, which is consistent with previous results [39]. The PL spectra obtained from the ADT-TIPS-CN composite at multiple temperatures are presented in Fig. 4.4. At room temperature peak emission is at λ~668 nm (1.86eV), which matches the energy difference between the LUMO of the acceptor and the HOMO of the donor. The PL is, thus, attributed to exciplex emission, which is consistent with previous results from ADT-TES-F/ADT-TIPS-CN composites [40]. As the temperature decreased, the PL spectra red-shifted at a rate of $(2.5 \pm 0.1) \times 10^{-4}$ eV/K, similar to that in the pristine ADT-TES-F films (Fig. 4.3(b)) [35]. The red shift is therefore considered to be related to disorder effects of ADT-TES-F in the films [35, 69].

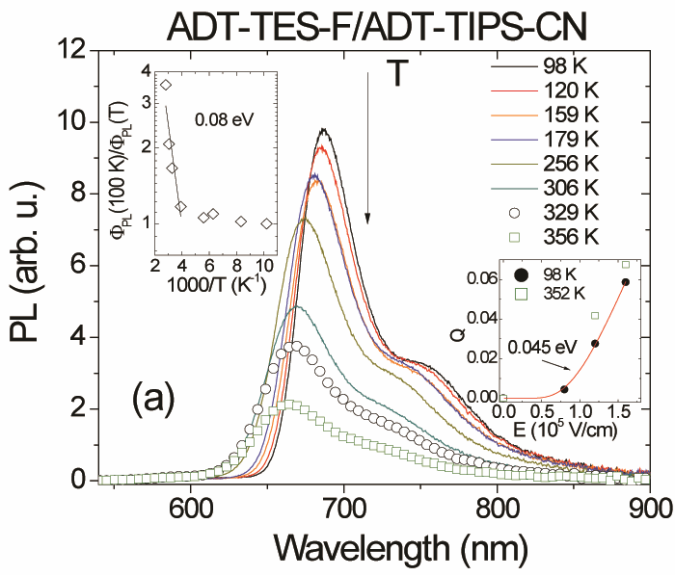

Figure 4.4: PL spectra obtained from an ADT-TES-F/ADT-TIPS-CN (2%) film at multiple temperatures. (Left inset): The inverse of PL QY (Φ), normalized by its value at 100 K, as a function of inverse temperature. A fit to the data with $\Phi_{PL} \sim \exp(-\Delta_{PL}/k_BT)$ is also shown. (Right inset): The E-field-induced PL quenching parameter Q as a function of applied electric field, at 98 K and 352 K. A fit of the data at 98 K to Eq.(4.4) and the binding energy $E_b = 0.045\pm0.003$ eV are also included.

In addition, the PL QY in the composites with ADT-TIPS-CN increased as the temperature decreased (Fig. 4.4), similar to that in pristine ADT-TES-F [35]. This behavior can be described by thermally activated exciton diffusion to excitonic dark states, leading to nonradiative recombination [71, 72]; such that this diffusion is 'frozen out' at low temperatures resulting in larger PL QY. It should be noted, that temperature-dependent nonradiative recombination has been previously noted in various ADT films [38]. From this physical picture, we consider a thermally activated nonradiative recombination rate, k_{nr}, which can be expressed as

$$k_{nr}(T) = k_{nr}^{0} + k_{nr}^{*} \exp\left(-\Delta_{PL} / k_B T\right) \qquad (4.1)$$

where Δ_{PL} is the activation energy and k_{nr}^{0} and k_{nr}^{*} are constants [73]. The temperature dependent QY, Φ(T), is related to $k_{nr}(T)$ by

$$\Phi(T) = \frac{k_r}{k_r + k_{nr}(T)} \tag{4.2}$$

From Eqs. (4.1) and (4.2), it can be shown that the ratio of the QY at temperature T=100K divided by the QY at T is

$$\frac{\Phi(100K)}{\Phi(T)} \sim A\exp\left(-\Delta_{PL}/k_B T\right) \tag{4.3}$$

The left inset of Fig. 4.4 shows a fit of Eq. 4.3 to data from a ADT-TES-F/ADT-TIPS-CN film. The fit yielded an activation energy Δ_{PL} = 0.08±0.02 eV, comparable to ~0.07 eV in pristine ADT-TES-F films [35], suggesting that mechanisms for non-radiative recombination are similar to that of the ADT-TES-F exciton.

To explore effects of the electric field on the exciplex, PL spectra were measured at multiple electric field strengths and temperatures. To quantify E-field activated PL quenching, the parameter Q,

$$Q = 1 - \frac{I_{PL}(E)}{I_{PL}(0)} \tag{4.4}$$

was calculated, where E is the E-field applied to the sample, $I_{PL}(E)$ is the integrated PL spectra at the field value E, and $I_{PL}(0)$ is the integrated PL spectra without an applied E-field. In the ADT-TES-F/ADT-TIPS-CN samples, values of Q reached ~0.06-0.07

at the highest applied field of 160kV/cm, at all temperatures studied (right inset of Fig. 4.4). In this study the behavior of *Q(E)* did not change significantly over the temperature range studied. However, from the *Q(E)* data, the nature of the exciplex exciton can be determined. For example, a linear dependence of *Q* on the E-field has been attributed to charge-transfer excitons dissociating into free carriers, while a quadratic dependence has been related to neutral exciton dissociation [74, 75]. In the ADT-TES-F/ADT-TIPS-CN composites, the dependence of Q on the electric field was stronger than quadratic at fields above ~ 50kV/cm, similar to what was observed in pristine ADT-TES-F [35]. This behavior is better described by a one-dimensional model for tunneling through a potential barrier [76]:

$$Q = \left\{ 1 + A \exp\left[\frac{\pi \sqrt{m^*} E_b^{3/2}}{2\sqrt{2}\hbar e E} \right] \right\}^{-1} \qquad (4.5)$$

where A is a constant (free fit parameter), m^* is the effective mass, $\hbar$ is the Planck constant, e is the unit charge, and E_b is the exciton binding energy. Fits to the data with Eq. 4.5 (assuming $m^* = m_e$) yielded a binding energy of $E_b = 0.045 \pm 0.005$ eV at 98 K, which did not appreciably change with temperature (right inset of Fig. 4.4). The binding energies obtained for the exciplex where smaller than those obtained in pristine ADT-TES-F ($E_b = 0.097 \pm 0.009$ eV), which were also temperature independent [35]. The lower binding energy obtained for the exciplex, is consistent with the physical picture of a larger spatial separation between the electron-hole pair in the exciplex as compared to the ADT-TES-F exciton.

In addition, it was determined from temperature dependent PL lifetime measurements, conducted on the same ADT-TES-F/ADT-TIPS-CN (2%) composite samples, that the ADT-TES-F exciton is likely a precursor state to exciplex formation [35]. The existence of a slow charge carrier generation channel, on the ~20 ns time-scale, due to dissociation of the exciplex was also discovered in PL-lifetime measurements as a function of E-field in these samples [35, 40].

4.3.2 Transient Photocurrent in Composite Films

Figure 4.5 shows transient photocurrent in an ADT-TES-F film at multiple temperatures, obtained under 355 nm, ~500 ps, pulsed illumination at an electric field of 120kV/cm. The measured rise time was limited by the laser pulse width, at all temperatures, which suggests sub-500 ps charge carrier photogeneration, consistent with our previous findings [37, 39, 40]. After the fast initial charge carrier generation, the transient photocurrents exhibited a fast initial decay, due to charge carrier trapping and recombination, followed by a slow power-law decay on time-scales up to ~1-2 μs indicative of tunneling transport [77]. Three main changes in the transient photocurrent were observed as the temperature decreased: (i) the peak amplitude decreased (by ~7-8 from 298K to 100K), (ii) the initial decay dynamics became faster and more pronounced, (iii) the long time-scale tunneling transport did not change substantially, and (iv) the E-field dependence of the peak amplitude became stronger, which was attributed to the mobility being E-field dependent (as described in detail in Ref [35]).

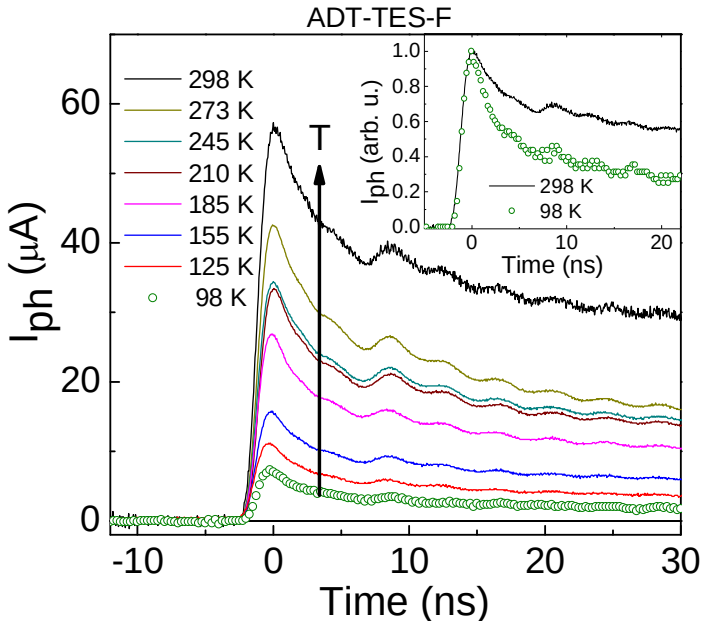

Figure 4.5: Transient photocurrent (I_{ph}) measured in a spun-cast pristine ADT-TES-F film at multiple temperatures. Data was taken with an applied E-field of 120 kV/cm. (Inset) I_{ph} measured at 298 K and 98 K, normalized by their peak values.

The addition of the C_{60} acceptor to ADT-TES-F, in composite films, resulted in transient photocurrents that exhibited sub-500ps initial charge carrier photogeneration at all temperatures studied, similar to pristine ADT-TES-F (Fig. 4.6). However, the peak photocurrents were ~2-3 higher, than those obtained from pristine ADT-TES-F films under similar conditions. This increase in photocurrent on short time-scale is consistent with previous results, and is due to improved charge carrier photogeneration on the sub-500 ps time-scale resulting from donor to acceptor charge transfer to charge separated states [39]. In addition, peak photocurrent in these composites was followed by a faster initial decay (limited by the pulse width) than that in pristine ADT-TES-F films, which is also consistent with previous studies [39]. This fast initial decay is attributed to enhanced initial carrier trapping and

recombination in these composites. The fast initial decay was then followed by a slow power-law decay on longer time-scales, as was obtained in pristine ADT-TES-F films. The temperature dependent trends of the photocurrent in the C_{60} composites were similar to those in pristine ADT-TES-F films [35]. As the temperature decreased the following was observed: (i) the peak photocurrent decreased in a similar manner to that in pristine ADT-TES-F films (Fig. 4.8), (ii) the contribution of the fast initial decay to the transient became more pronounced (Fig. 4.6, inset), and (iii) the slower power-law decay component was weakly temperature dependent. Thus, physical mechanisms that determine the temperature dependence of the transient photocurrent in ADT-TES-F/C_{60} composites are similar to those in pristine ADT-TES-F films (as explained in *Section. 4.3.3*).

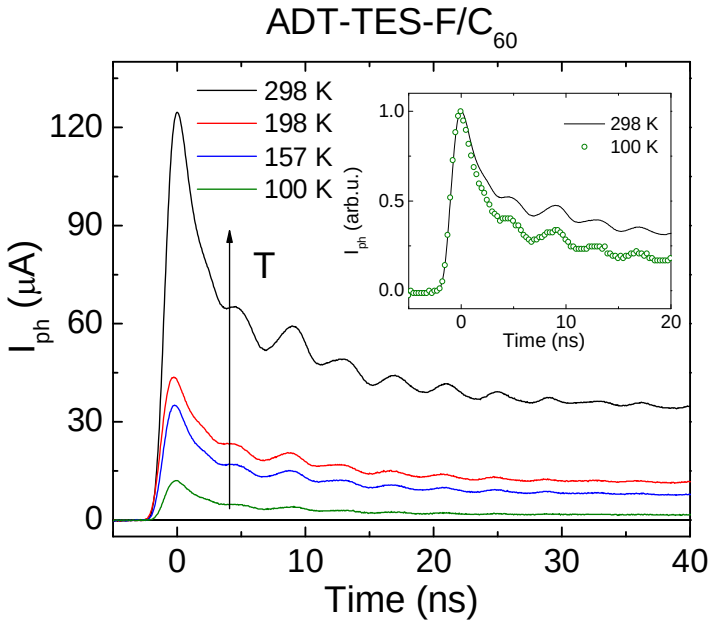

Figure 4.6: Transient photocurrent (I_{ph}) measured in a spun-cast ADT-TES-F/C60 (2%) composite film at 120 kV/cm. Data is shown for multiple temperatures. (Inset) I_{ph} measured at 298 K and 98 K, normalized by their peak values.

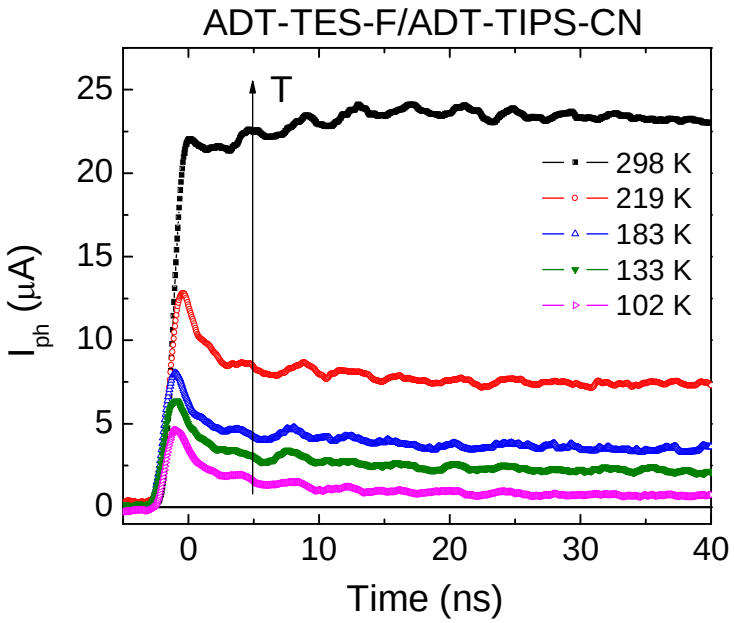

Figure 4.7: Transient photocurrent (I_{ph}) measured in a spun-cast 2% ADT-TES-F/C_{60} composite film at 120 kV/cm. Data is shown for multiple temperatures.

Figure 4.7 shows the transient photocurrent in an ADT-TES-F/ADT-TIPS-CN (2%) film at multiple temperatures, obtained under 355 nm, ~500 ps, pulsed illumination at an electric field of 120kV/cm. At room temperature, initial sub-500ps charge carrier photogeneration, (η) was about a factor of ~2 lower than that in pristine ADT-TES-F films. In addition, the peak photocurrent occurred at ~20 ns after the photoexcitation, due to the emergence of a slower component in the photocurrent rise dynamics. This component has been previously attributed to slow charge carrier photogeneration due to exciplex dissociation over the period of exciplex lifetime (~20 ns) [40]. At times above ~20 ns, a power-law decay slower than that obtained in pristine ADT-TES-F was measured. Drastic slowing down of the photocurrent decay dynamics in the ADT-TES-F/ADT-TIPS-CN composite as compared to that in pristine ADT-TES-F films has previously been attributed to inhibited charge carrier

recombination [39]. The temperature dependent trends of the photocurrent in the ADT-TIPS-CN composites were similar to those in the pristine ADT-TES-F films, indicative of similar charge transport properties (as described below in *Section 4.3.3*). In particular, as the temperature decreased, the photocurrent at ~1 ns after photoexcitation decreased in a similar manner to that in pristine ADT-TES-F films (Fig. 4.5), and the initial decay dynamics (at <5 ns) became faster. At low temperatures, the contribution of charge carriers produced via exciplex dissociation to the photocurrent was no longer observed, due to less efficient exciplex dissociation and more pronounced carrier loss in deep traps.

4.3.3 Thermally Assisted Charge Transport on Short Time-Scales

As mentioned above, the temperature dependent behavior of the transient photocurrent in composites films was similar to that in pristine ADT-TES-F. To quantify this trend, the peak photocurrent, $I_{ph,peak}$, at all temperatures was normalized to that at 300K (Fig. 4.8). It can be seen from the data that the temperature dependence of , $I_{ph,peak}$ is almost identical in both composites films and in pristine ADT-TES-F. At an electric field of 120kV/cm, the photocurrent activation energy, Δ_{ph}, was obtained from fits to the peak photocurrent data in Fig. 4.8 with the Arrhenius-type function [10],

$$I_{peak,ph}(T) = \exp(-\Delta_{ph} / k_B T) \qquad (4.6).$$

These fits yielded values Δ_{ph}~0.025 (inset of Fig. 4.8, pristine ADT-TES-F shown). Additionally, the peak photocurrent, can be expressed as

$$I_{peak,ph}(E) = N_{abs} e\mu\eta E / L \qquad (4.7),$$

where N_{abs} is the number of absorbed photons during the pulse, *e* is the electric charge, μ is the mobility (here dominated by the hole mobility) [20, 78], *E* is the electric field, *L* is the gap between the electrodes and η is the photogeneration efficiency, which included carrier loss due to trapping and recombination during the pulse duration [34, 79]. From Eqs. (4.6) and (4.7) it can be seen that that the activation energy Δ_{ph} could be a result of the temperature dependence of the carrier mobility, μ, the photogeneration efficiency, η, or both. Given that the two composites under study exhibited a temperature dependence of the peak photocurrent that was similar to that in pristine ADT-TES-F films, in spite of differences in charge carrier photogeneration mechanisms in the two composites, the activation energy, Δ_{ph}, in the composites, like pristine ADT-TES-F, is most likely due to a thermally activated mobility, μ, rather than the photogeneration efficiency, η. This is consistent with previous observations of thermally activated mobility in ADT-TES-F TFTs [15]. As such, Δ_{ph} provides a measure of the energy distribution of charge traps participating in the hopping transport on short time-scales (~1ns). The similarity in Δ_{ph} in composites and in pristine ADT-TES-F also suggests that the energy distribution is dictated by the large percentage of ADT-TES-F in the composite films.

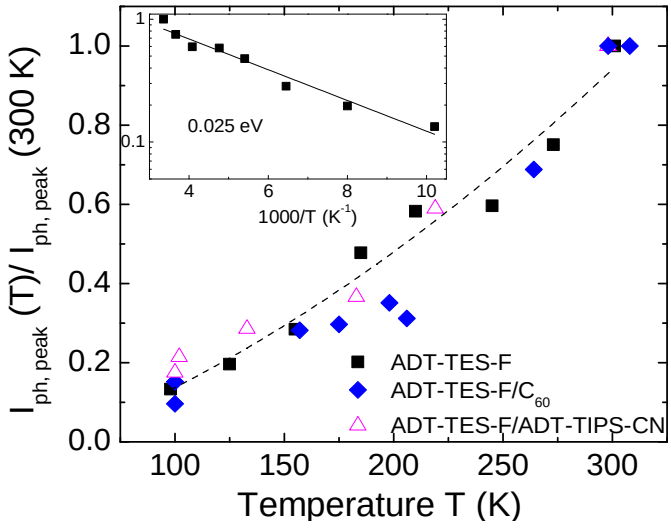

Figure 4.8: Temperature dependence of the peak photocurrent $I_{ph,peak}$ at 120kV/cm, normalized by the value at 300 K. Data is shown for pristine ADT-TES-F, ADT-TES-F/C_{60} (2%) composite, and ADT-TES-F/ADT-TIPS-CN (2%) composite films. The dashed line is a guide for the eye. The inset shows a fit of the data from a pristine ADT-TES-F film with $I_{ph,peak} \sim \exp(-\Delta_{ph}/k_BT)$. The resulting activation energy from the fits (Δ_{ph} = 0.025±0.003 eV) is also shown.

4.4 Discussion

4.4.1 Charge carrier dynamics

The observed PL and nanosecond time-scale photoconductive properties of pristine ADT-TES-F films and ADT-TES-F-based composites are consistent with the following picture (Fig. 4.9). The initial photoexcitation of ADT-TES-F was distributed among the excitonic channel (responsible for PL, blue-dotted arrow), fast photoconductive channel (responsible for fast photocurrents, η), and photoinduced electron transfer, CT. This distribution of the photoexcitation occurred on the picosecond or sub-picosecond time-scales.

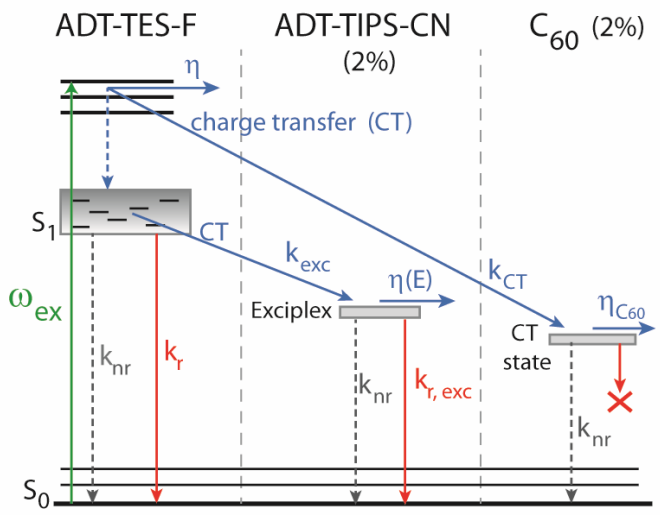

Figure 4.9: Schematic of exciton and charge carrier dynamics in ADT-TES-F/C_{60} and ADT-TES-F/ADT-TIPS-CN composite films. The ground state (S_0) and the exciton band (S_1) are shown for ADT-TES-F. The photoexcitation (ω_{ex}) in composites results in absorption by ADT-TES-F results in one of the following: fast charge carrier generation (η), charge transfer (k_{CT}), or internal conversion to S_1 and ADT-TES-F exciton formation (blue dotted line). Charge transfer to C_{60} results in charge carrier generation (η_{C60}). In the ADT-TES-F composite, internal conversion dominates and is followed by either the formation of a relaxed ADT-TES-F exciton or in charge transfer to an emissive exciplex state (k_{exc}). From the exciplex state, a slow charge carrier generation path, due to E-field assisted dissociation, occurs at room temperature. Radiative and nonradiative exciton and exciplex recombination are also shown (k_r, k_{nr}, and $k_{r,\,exc}$)

Upon photoexcitation of a higher excited state of ADT-TES-F (Fig. 4.9), the charge carriers were created on sub-500 ps (most likely on sub-30 ps or faster) [36, 39] time-scales, with a photogeneration efficiency $\eta<0.1$ (as determined in Ref [35]), which is independent of temperature and electric field. In order to distinguish between direct charge carrier photogeneration [80] and ultrafast hot exciton dissociation [81], both of which would be consistent with these observations, measurements of the wavelength dependence of time-resolved photocurrent would be necessary. The photogeneration efficiency was enhanced in the presence of C_{60} due to fast

photoinduced electron transfer (k_{CT}) from ADT-TES-F to C_{60} (e.g. by a factor of 2-3 in the ADT-TES-F/C_{60} (2%) composite). In the ADT-TES-F/ADT-TIPS-CN composite, after exciplex formation (k_{exci}), a small additional contribution ($\eta(E)$) to charge carrier photogeneration due to exciplex dissociation at time-scales of <20 ns was observed at room temperature, but not at low temperatures. In all three materials studied, electric field-induced dissociation of emissive excitons investigated by our PL measurements did not play an important role in fast charge carrier generation.

In all materials, at time-scales of ~0.5-5 ns, the charge carrier transport proceeded by hopping via shallow traps characterized by weakly thermally-activated (Δ_{ph}~0.025 eV) and electric field-dependent charge carrier mobility. At time-scales above ~5 ns after photoexcitation, the charge propagated within a narrow energy manifold by non-activated tunneling [82]. At low temperatures, a significant number of charge carriers were frozen in traps and did not contribute to charge transport at nanosecond time-scales.

4.4.2 Exciton dynamics

In ADT-TES-F/C_{60} composites, emissive species were the same as those in pristine ADT-TES-F films. However, the overall PL was strongly quenched due to efficient photoinduced electron transfer (k_{CT}) from ADT-TES-F to C_{60}. The residual ADT-TES-F PL emission, had similar temperature and E-field dependent behavior as was observed in pristine ADT-TES-F [35]. No evidence of emission from the CT state was observed (Fig. 4.9). In ADT-TES-F/ADT-TIPS-CN composites, the PL

emission at all temperatures was dominated by that of an exciplex formed between the HOMO of ADT-TES-F and LUMO of ADT-TIPS-CN. The relaxed ADT-TES-F exciton appears to be a precursor state for the exciplex, as schematically shown in Fig. 4.9, leading to similar features in the temperature and E-field dependence of the PL from the exciplex and the ADT-TES-F exciton. For example, fast nonradiative recombination, due to thermally-activated processes was observed. At low temperatures, it was possible to reactivate the fast nonradiative recombination process by applying an electric field, which induced PL quenching.

4.5 Conclusion

We have presented a physical picture of exciton and charge carrier dynamics in spin-cast ADT-TES-F/C_{60} (2%) and ADT-TES-F/ADT-TIPS-CN (2%) composite thin-films obtained through measurements and analysis of the temperature dependence of their optical absorption, PL, and photoconductive properties. In ADT-TES-F/C_{60} composites, the PL was considerably quenched due to fast photoinduced electron transfer from ADT-TES-F to C_{60}. The PL properties of the residual emission were similar to those of ADT-TES-F aggregates in pristine ADT-TES-F films. In ADT-TES-F/ADT-TIPS-CN composites, the PL emission was dominated by that due to an exciplex formed between ADT-TES-F and ADT-TIPS-CN (Fig. 4.4). The ADT-TES-F relaxed exciton appears to serve as a precursor to the exciplex. Thus, sub-200 ps thermally-activated nonradiative recombination with activation energies of ~0.08 eV and electric field-induced PL quenching at fields above 100kV/cm were observed in ADT-TES-F/ADT-TIPS-CN films, similar to those in pristine ADT-TES-F films.

Weak E-field-induced PL quenching was observed during the exciplex lifetime of ~20 ns at higher temperatures due to exciplex dissociation into free carriers (Fig. 4.8).

In all materials investigated, the charge carriers were generated on sub-500 ps time-scales (limited by the laser pulse width) (Figs. 4.5, 4.6, and 4.7) with the photogeneration efficiency independent of the electric field and temperature. In the C_{60} composites, the photogeneration efficiency was ~2-3 times larger than in pristine ADT-TES-F films. In addition, no evidence of emissive exciton dissociation contributing to fast charge carrier generation was observed, similar to what was observed in pristine ADT-TES-F films [35]. In ADT-TES-F/ADT-TIPS-CN (2%) composite films, the efficiency of fast charge carrier photogeneration was reduced, but an additional slow charge carrier photogeneration process developed on time-scales of ~20 ns due to exciplex dissociation at room temperature. This long time-scale contribution was not observed at lower temperatures. In all materials, the charge transport at 0.5-5 ns after photoexcitation was dominated by electric field- and temperature-activated hopping via shallow traps with an activation energy of ~0.025 eV at 120kV/cm, relaxing to iso-energetic tunneling at time-scales above ~5 ns.

5 Formation of Donor-Acceptor Charge Transfer Excitons and Their Contribution to Charge Carrier Photogeneration and Recombination

5.1 Introduction

Organic optoelectronic materials have drawn interest based on their low cost and tunable properties, and have shown promise in a wide range of applications, from display technologies to photovoltaics [8, 58]. Additionally, solution-processable organics can be combined into composite materials, which have drastically different optical and electronic properties and can be tailored for specific applications. For example, organic bulk heterojunctions (BHJs) have been utilized in solar cells [64], photodetectors [65], and photorefractive devices [7], due to enhanced photogeneration of charge carriers that results from photoinduced electron transfer between donor (D) and (A) acceptor molecules with properly offset HOMO and LUMO energy [55]. Currently, most high-performance BHJs are combinations of a photoconductive polymer donor with fullerene-based acceptors, whereas small-molecule BHJs have not yet been explored to the same extent [83-86].

The difference in LUMO energies of the donor and acceptor (ΔLUMO) and molecular packing at the D/A interface have been identified as key factors in efficient charge photogeneration [55, 68, 87, 88]. However, the mechanisms driving the evolution of an exciton created by an absorbed photon in the donor to free charge carriers, especially those involving the formation of intermediate bound charge transfer (CT) states shared between adjacent donor and acceptor molecules, are not completely understood. As a result, the dependence of these mechanisms on the

ΔLUMO and molecular alignment at the D/A interface is still under investigation [55, 89-91]. In particular, the relationship between properties of CT excitons and photocurrent is not well understood [55], and is important to address for the development of efficient BHJs.

In this chapter, we systematically explore the effects of (i) the ΔLUMO and (ii) the molecular packing at the D/A interface on CT state formation, exciton dynamics, and photocurrent in small-molecule BHJs. The chapter is organized as follows: In Section 5.2, the materials used in the study, sample preparation and experimental techniques are described. In Section 5.3, experimental results are presented, along with a discussion of the results. In Section 5.4, the findings from the study are summarized.

5.2 Materials and Experimental Methods

5.2.1 Anthradithiophene Donor Molecule

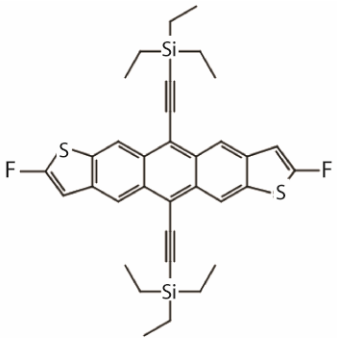

Figure 5.1: Molecular structure of the donor molecule ADT-TES-F.

In this study, the high performance ADT-TES-F (Fig. 5.1) was used as the donor material. This ADT derivative was chosen, given its high charge carrier (hole)

mobility (e.g. > 1.5 cm^2 /(Vs) in spin-coated thin-films on treated electrodes [20, 21]) and its relatively strong photoluminescence (PL) in solution deposited thin-films [38]. In addition, previous work using ADT-TES-F as a donor in composites films has shown promising results [39, 40]. For example, emissive exciplex formation with long charge carrier lifetimes have been observed in composites with ADT-TIPS-CN as an acceptor, while strong PL quenching and enhanced charge carrier generation with short charge carrier lifetimes were observed in composites with C_{60} as an acceptor [39]. In addition, work presented in the previous chapter identified: (i) a model for charge carrier photogeneration, and (ii) thermally activated hopping charge transport in these composites with ADT-TIPS-CN and C_{60} as acceptors.

5.2.2 Acceptor Molecules

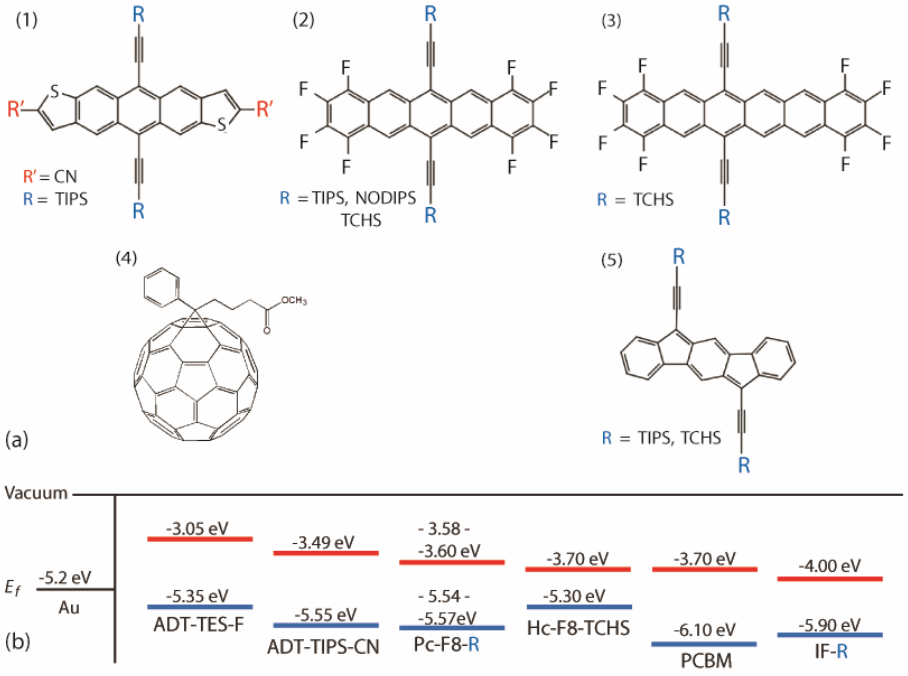

Figure 5.2: (a) Molecular structures of the acceptors used in the study: (a.1) ADT-TIPS-CN; (a.2) Pn derivatives; (a.3) Hex derivative; (a.4) PCBM; and (a.5) IF derivatives. (b) HOMO and LUMO energies of molecules under study.

To explore ΔLUMO effects, we chose multiple acceptors that yielded a ΔLUMO ranging between 0.44 and 0.95eV (Fig. 5.2(b) and Table 5.1). To explore packing effects, two different groups of acceptor molecules were chosen, pentacene (Pn) and indenofluorene (IF) derivatives, which have similar LUMO energies but are functionalized with different sized side groups (R in Fig. 5.2(a)) that yield different packing motifs in the solid state [13, 17]. In particular, the following acceptor molecules were employed: (i) ADT-TIPS-CN, Fig. 5.2 (a.1) [35, 40]; (ii) three fluorinated Pn derivatives with TIPS[92], n-octyl disopropylsilyl (NODIPS), and tricyclohexylsilyl (TCHS) side groups (Pn-F8-R, Fig. 5.2(a.2)); (iii) a fluorinated

hexacene derivative with TCHS side groups (Hex-F8-TCHS, Fig. 5.2(a.3)) [93]; (iv) two IF derivatives with TIPS and TCHS side groups (IF-R, Fig 5.2(a.5)) [94]; and (v) PCBM (Fig. 5.2(a.4), from Sigma-Aldrich). HOMO and LUMO energies for all molecules under study, measured using differential pulse voltammetry [50, 52], are shown in Fig. 5.2(b). Molecular structures for side groups, are provided in Fig. 5.3. Although the exact molecular arrangement of donor and acceptor molecules at the D/A interface is not known, the average volume per molecule calculated from crystallographic data (unit cell volume divided by the number of molecules in the unit cell, Table 5.1) for the donor and acceptor molecules provided a relative measure of separation between the donor and acceptor molecules in the solid state. For example, in composites with Pn acceptors, the largest D/A separation at the D/A interface would be expected with TCHS side groups, followed by NODIPS and TIPS side groups. It should be noted that crystallographic information was obtained from our collaborators: Dr. John Anthony at the University of Kentucky and Dr. Mike Haley at University of Oregon.

Material	ΔLUMO (eV)	volume/molecule[a] (Å^3)	Exciplex Peak PL (eV) (E_{DA})	I_{PL}/I_{PL}(TIPS-CN)[c] Exciplex	$I_{PL,\ exciplex}/I_{PL,total}$[d]	$t_{ph,\ max}$ (ns)[e] at 20 (100) (kV/cm)
pristine ADT-TES-F	N/A	807				<0.6 (<0.6)
D/A composites						
ADT-TIPS-CN	0.45	1051	1.86 (1.86)	1	0.97	<0.6 (<0.6)
Pn-F8-NODIPS	0.53	2491	1.72 (1.76)	0.067	0.62	3.2 (<0.6)
Pn-F8-TCHS	0.54	2661	1.75 (1.77)	0.022	0.39	2.3 (<0.6)
Pn-F8-TIPS	0.55	1975	1.72 (1.75)	0.17	0.51	<0.6 (<0.6)
Hex-F8-TCHS	0.65	2726	-	-	-	2.2 (<0.6)
PCBM	0.65	2343[b]	-	-	-	2.8 (<0.6)
IF-TCHS	0.92	-	-	-	-	3.2 (<0.6)
IF-TIPS	0.95	1855	-	-	-	<0.6 (<0.6)

Table 5.1: Electrochemical, crystallographic, photoluminescent, and photoconductive properties of films. [a]Calculated as unit cell volume (from CIF files) divided by the number of molecules in the unit cell. Most molecules had one molecule per unit cell, except for acceptors with TCHS side groups which had 2 molecules per unit cell. [b] From Ref.[95] [c] Exciplex PL obtained from integrated exciplex PL spectra in various D/A composites with respect to that in the composite with ADT-TIPS-CN acceptor. [d] Relative contribution of the exciplex PL in the overall PL emission of the composite. [e] The time at which the transient photocurrent reached maximum at the applied field of 20 kV/cm (100 kV/cm).

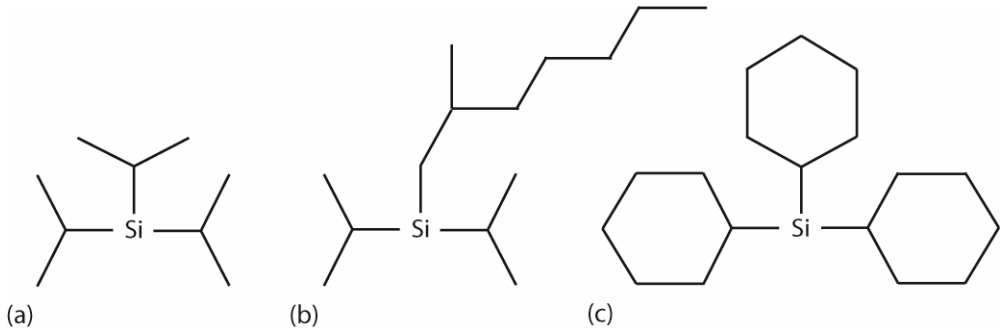

Figure 5.3: Chemical structure of the functionalized side groups. (a) TIPS = SiC_9H_{21} (b) NODIPS = $SiC_{14}H_{31}$ and (c) TCHS = $SiC_{18}H_{33}$.

5.2.3 Sample Preparation

In all our experiments, both in solution and thin-film, donor and acceptor compounds were dissolved in toluene (JT Baker, >99.7% purity). For experiments in

solution 0.1 mM concentrations of molecules in toluene were prepared in two steps. First a 'stock' 10 mM concentration solution was prepared and then diluted 10 fold. For drop-cast films preparation, 2% wt/wt composite solutions were made by combining 6 mM solutions of ADT-TES-F in toluene and 1 mM solutions of acceptor molecules in toluene, at the appropriate ratios. As mentioned in *Section 4.2.2*, the low concentration of acceptor molecules was chosen to minimize the disruption of film crystallinity [67] and thus a reduction in hole mobility. Additionally, this enabled us to relate the photocurrent dynamics to properties of the CT states, while neglecting effects of acceptor domain formation and electron mobility in the acceptor domains [68].

Drop-cast films of pristine ADT-TES-F and composite films were prepared on glass substrates with photolithographically deposited Cr/Au electrode pairs (5 nm/50 nm). Each interdigitated electrode pair consisted of 10 pairs of 1 mm long and 25 μm wide fingers, with a 25 μm gap between the fingers of opposing electrodes (see *Section 3.2.1* and Fig. 3.2 for further details). Films were typically drop-cast from 16 to 40 μL of solution onto a clean substrate on a hot plate at temperatures between 60^{o} and 70^{o} C, yielding polycrystalline films. To drop-cast the film, the solution was dispensed slowly as to control the solvent evaporation, such that the desired film area covered the electrode pairs. After film deposition, samples were allowed to sit on the hotplate at 45^{o}-50^{o} C for ~30 min and then placed in a closed Petri dish over night to promote residual solvent evaporation.

5.2.4 Optical Absorption Experiments

For optical absorption in solution, samples were illuminated with fiber coupled light through a collimating lens, from a halogen lamp source (LS-1, Ocean Optics). The light that was transmitted through the sample was collected with a lens (Ocean Optics, 74-VIS) into a fiber, which coupled the transmitted light into an Ocean Optics USB2000, UV-VIS, spectrometer (*Section 3.2.2*, Fig. 3.3). Absorption data were obtained from the transmission measurements as described in *Section 3.2.2*.

Optical absorption measurements of thin-films, via transmission spectroscopy, with and without an applied E-field were conducted on an inverted microscope (Olympus, IX71). Samples were mounted onto a custom sample holder, similar to those used for cw photocurrent measurements, which was then mounted onto a micrometer driven 2-D stage. Samples were illuminated with halogen lamp light that was coupled into a 50 μm fiber. Light from the fiber was collimated and then focused using a lens pair (50mm and 30 mm part) as to only illuminate an area within the electrodes. Light transmitted through the sample was coupled into a 10x objective (Olympus, UPLANFL N), routed through the microscope's confocal port into a fiber (Ocean Optics, P1000-2-1000-UV-VIS), and collected by a spectrometer (Ocean Optics USB2000, UV-VIS FLG). With this experimental setup, absorption could be measured at different locations in the film within the interdigitated electrode area. An area on the sample substrate without film (i.e. glass only) was used as a reference. For electric field (E-field) dependent measurements, voltage was applied to the samples using a Keithley 237 source/measure unit. As with all measurements described below,

the average applied *E*-field was calculated using $E = V/L$, where L is the gap between the electrodes.

5.2.5 Photoluminescence (PL) Measurements

PL was excited in our experiments with 532 nm (Nd:YVO4, Coherent) light. The measurements of PL in solution were conducted in the same manner as in *Section 3.2.3.* However, PL measurements in films were conducted on an inverted microscope. Samples were mounted in a similar fashion as absorption measurements and were illuminated with wide-field excitation through a 10x objective. PL emission was coupled back into the microscope through the objective, and then through a 560DCLP dichroic mirror (Omega optical) to filter out scatter at the excitation wavelength. Emission, through the microscope's confocal port, was then coupled into a 1 mm fiber (Ocean Optics, P1000-2-1000-UV-VIS), and delivered to a spectrometer (Ocean Optics USB2000, UV-VIS FLG). The spectrometer was calibrated to 3100K halogen lamp light that was collected through the emission path in the microscope, described above. This was done mainly to account for the spectral response of the dichroic mirror. Voltage was applied to samples for the E-field dependent PL measurements using a Keithley 237 source/measure unit.

5.2.6 PL Lifetime Measurements

PL lifetime measurements were taken under 400 nm excitation from a frequency-doubled 100 fs Ti:Sapphire laser (Kapteyn-Murnane Labs) with a repetition rate of 93MHz. A time-correlated single photon counter (TCSPC) board (PicoQuant

TimeHarp 200) was used with a single photon avalanche photodiode (SPAD – Molecular Photonic Devices) for detection. Appropriate combinations of a 420DCLP dichroic mirror (Omega Optical), a 3RD440LP long pass filter (Omega Optical), and a D740/80x band-pass filter (Chroma Tech.) were used to study the lifetimes of either ADT-TES-F or exciplex PL. The instrument response function (~ 200 ps) was recorded using scattered light from a frosted microscope slide. The PL lifetime data were fit with a single-exponential function (I_{PL}~ Cexp[-t/τ]) to determine the amplitude C and lifetime τ of the PL emission [96]. Voltage was applied to samples for the E-field dependent PL measurements using a Keithley 237 source/measure unit.

5.2.7 Dark and Cw Photocurrent Measurements

Continuous wave (cw) photocurrents in films were measured under 532 nm ($Nd:YVO_4$,Coherent) excitation at an intensity of ~3 mW/cm^2, or broad-band ~300-400 nm (peaked at ~370 nm) excitation at an intensity of ~2 mW/cm^2 (96000 solar simulator, Newport). See Fig. 3.5 in *Section 3.2.4* for the diagram of the setup. Unwanted wavelengths of light were filtered from the solar simulator spectra with a dichroic mirror (Oriel 81045), a UV band-pass filter (Oriel 81046), and a color glass filter (BG39, CVI). Samples were mounted on a custom sample holder, and voltage (*V*) was applied to the samples and currents measured using a Keithley 237 source-measure unit. Photocurrent was calculated as the difference between the current measured under photoexcitation and the dark current. In addition, dark current measurements were always conducted before photocurrent measurements. In pristine

ADT-TES-F films under these photoexcitation conditions, the photocurrents, for example, reached ~40 μA (12μA) at 532 nm (~370 nm) excitation at an applied E-field of 40 kV/cm.

5.2.8 Transient Photocurrent (I_{ph}) Measurements

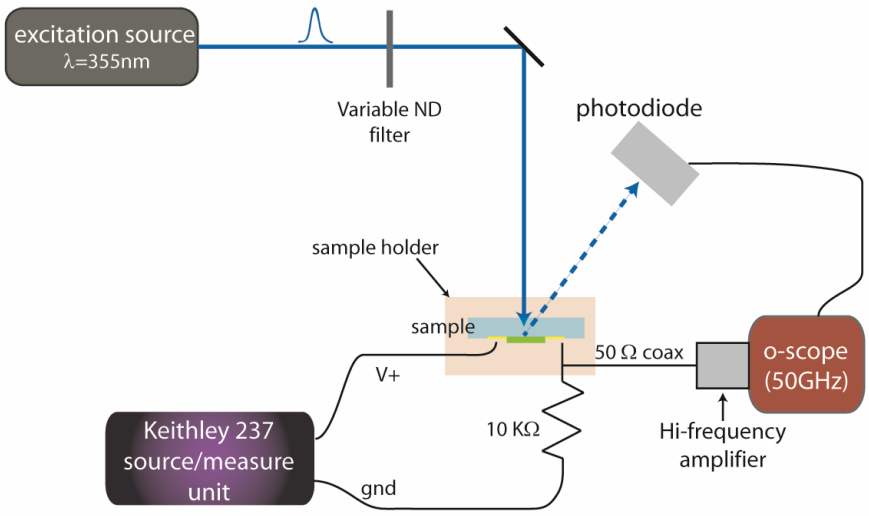

Figure 5.4: A diagram of the experimental setup for transient photocurrent measurements.

For transient photocurrent measurements, a 355 nm, 500 ps, 0.18 μJ/cm^2 pulsed laser (Nd:YAG laser, 44.6 kHz repetition rate, from Nanolase) source was used to excite photocurrent in samples (Fig. 5.4). Samples were back illuminated, and voltage (*V*) was applied using a Keithley 237 source-measure unit. Transient photocurrents were measured using a 50 GHz digital sampling oscilloscope (CSA8200/Tek80E01) with a Centellax UAOL65VM broadband amplifier (100 kHz to 65GHz) for measurements on nanosecond time-scales. For measurements on microsecond time-scales a 300 MHz digital sampling oscilloscope (Agilent

DSO6032A) was used without the amplifier. Samples were mounted on custom made sample holders that were designed to have minimal parasitic inductance and capacitance to limit unwanted electrical artifacts in the short time-scale (high-frequency band-width) transient photocurrent signals (Fig. 5. 5). The time resolution of the setup was about 500 ps, limited by the laser pulse width and coax cables.

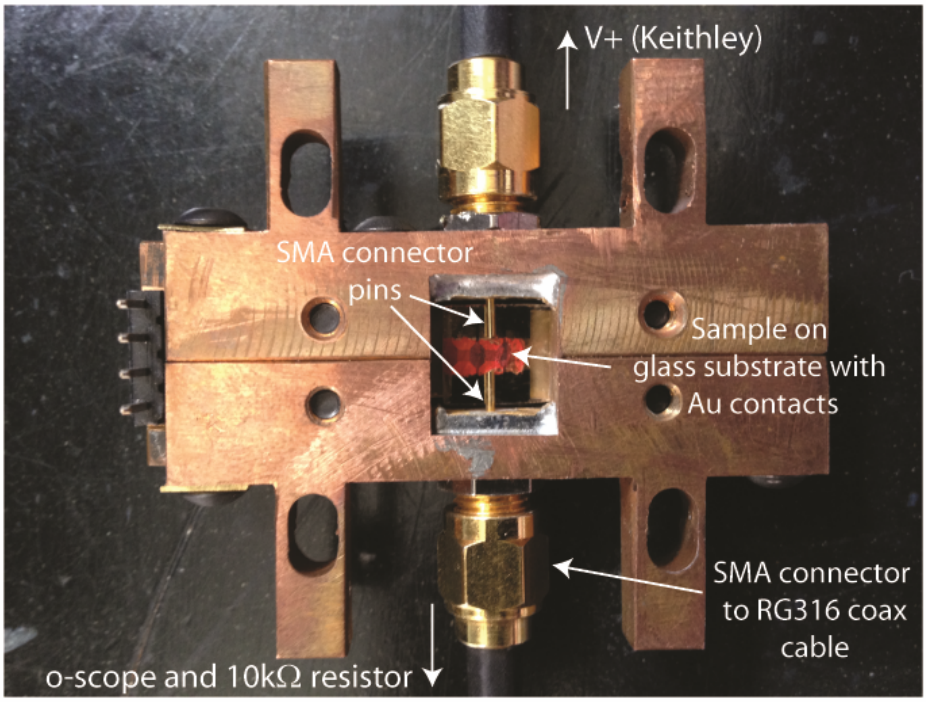

Figure 5.5: Image of sample holder used for transient photocurrent measurements. SMA connectors are used to connect RG-316 coax cables directly to the sample substrate.

5.3 Experimental Results and Discussion

5.3.1 Optical Properties of Acceptors in Solution

The optical properties of acceptor molecules in toluene solution were studied before making composite samples. Figure 5.6 shows optical absorption and PL

spectral data for the ADT-TES-F donor and for selected acceptors used in the study in toluene. Spectral data for Pn-F8-TIPS, which is not shown, was identical to the data shown for Pn-F8-NODIPS. In solution the functionalization of the backbone with different side groups is not expected to affect the optical properties of the molecule [38]. Interestingly, the data for Pn-F8-TCHS (also not shown) was red-shifted by ~2-3 nm from data obtained in Pn-F8-NO-DIPS and Pn-F8-TIPS solutions. A similar red-shift of ~2-3 nm was observed in the absorption of IF-TCHS (not shown), as compared to IF-TIPS; we are unsure of the cause of these spectral shifts. In addition, both IF derivatives are non-fluorescent in solution.

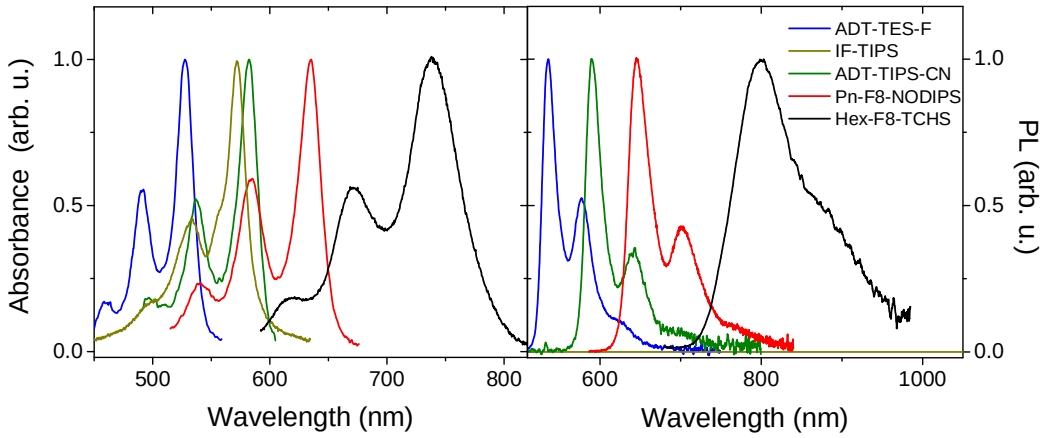

Figure 5.6: Optical absorption and PL spectra from ADT-TES-F (donor) and acceptor molecules in toluene.

5.3.2 Optical Absorption and PL in Composites

To explore changes in exciton dynamics due to various acceptors in composite films, we measured the optical absorption, PL spectra, and PL lifetime decays. Absorption spectra of all composites were similar to those of the pristine donor films (Fig. 5.7). Analysis of PL emission in pristine donor films is described in *Section*

4.3.1 and has also been previously reported [35, 38, 41]. In addition, absorption did not change significantly under applied E-field in pristine donor (Fig. 5.7), or composite films.

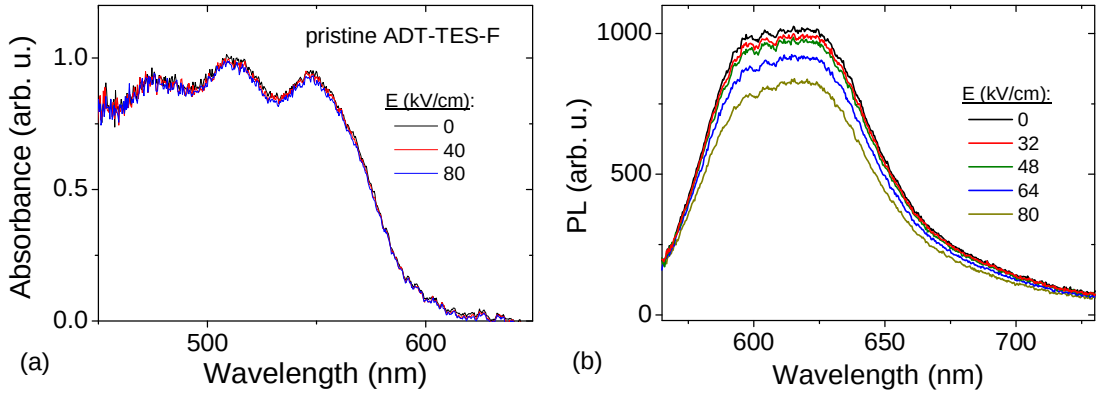

Figure 5.7: (a) Absorption spectra and (b) PL spectra as a function of applied E-field in a pristine ADT-TES-F donor film.

In all D/A composites with an acceptor such that ΔLUMO <0.6 eV (i.e. Pn-F8-R and ADT-TIPS-CN), PL spectra that was red-shifted from donor emission was observed (e.g peak PL~715nm in Fig. 5.8). The peak of this spectral feature closely matches the energy gap between the LUMO of the acceptor and the HOMO of the donor, E_{DA} (Table 1), and cannot be attributed to PL features from the acceptor molecules in solution, thus this PL is attributed to an emissive CT state (exciplex) (Fig. 5.8) [35, 40]. In addition, from single exponential fits (I_{PL}~Cexp(-t/τ) [96]) to PL lifetime data (Fig. 5.8(b)) without an applied E-field, lifetimes of the exciplex (e.g. ~3.2-3.4 ns, ~4.3-4.6 ns, and ~20 ns in composites with Pn-F8-NODIPS, Pn-F8-TIPS, and ADT-TIPS-CN acceptors, respectively) were longer than those of ADT-TES-F

excitons in pristine donor films (~1.3 ns). The longer PL-lifetimes of the exciplex (or CT state) emission is consistent with previously reported results [40, 97].

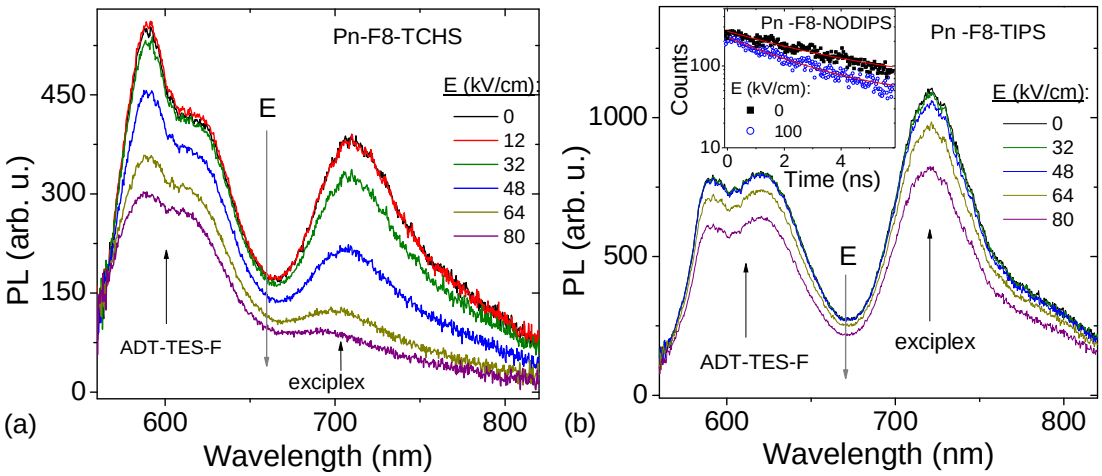

Figure 5.8: (a) PL spectra of composite films with Pn-F8-TCHS and (b) Pn-F8-TIPS acceptors at multiple values of applied E-field. Spectral contributions corresponding to residual ADT-TES-F donor emission and to exciplex emission are indicated. (Inset) PL lifetime decays of the ADT-TES-F/Pn-F8-NODIPS exciplex in the absence of applied electric field and at 100 kV/cm. Single exponential fits (I_{PL}~Cexp(-t/τ)) are also included. The resulting fit parameters are: C=206±2.9, τ =3.43±0.08 ns in the absence of the electric field and C=183±2.5, τ=2.52±0.05 at 100 kV/cm.

The strongest exciplex emission was observed in the composite with ADT-TIPS-CN (smallest D/A separation of all composites), in which most of the emission originated from the exciplex, while that of the donor was almost completely quenched (Table 1) [35, 40]. Exciplex emission and quenching of donor emission were considerably weaker in the composites with Pn-F8-R than those with ADT-TIPS-CN (Table 5.1 and Fig. 5.8). In addition, a factor of ~8x (~2.5x) stronger exciplex emission was observed in the composite with Pn-F8-TIPS as compared to that with Pn-F8-TCHS (Pn-F8-NODIPS). This trend correlates well with the size of the

acceptor's side group R, such that a larger D/A separation at the D/A interface corresponds to a less emissive exciplex.

In all composite films with acceptors such that ΔLUMO >0.6 eV (0.65-0.95 eV, Table 5.1), there was no evidence of exciplex emission, as only the residual PL from the ADT-TES-F donor was present (Fig. 5.9). In previously studied ADT-TES-F/C_{60} (2 wt%) D/A films (ΔLUMO = 1.45eV), a factor of 5-10 reduction in the PL quantum yield (depending on the film preparation method) was observed, as compared to that in pristine donor films. This non-E-field assisted quenching was attributed to fast photoinduced charge transfer from the donor to the acceptor into charge separated states, which is beneficial for fast charge carrier photogeneration [35, 39]. A considerably weaker PL quenching of the donor was observed in the composites under study with PCBM, Hex-F8-TCHS, and IF-R acceptors, ranging between a factor of 1.3 (in composites with PCBM) and 2 (in those with Hex-F8-TCHS). This suggests that the donor to acceptor charge transfer to charge separated states in these composites is not as efficient as in those with C_{60}. The reduced efficiency in the films in this study could be due to smaller ΔLUMOs, larger D/A separation[95], or both.

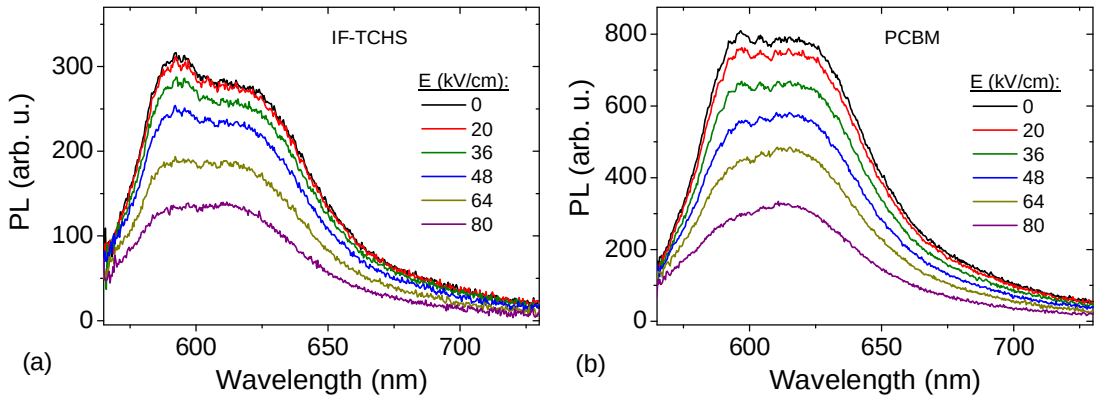

Figure 5.9: PL spectra of composites with (a) IF-TCHS and (b) PCBM acceptors at multiple values of applied E-fields. Increased PL quenching of ADT-TES-F exciton emission was observed in composites with larger D/A separation.

5.3.3 PL Quenching and Exciton Dissociation in Composite Films

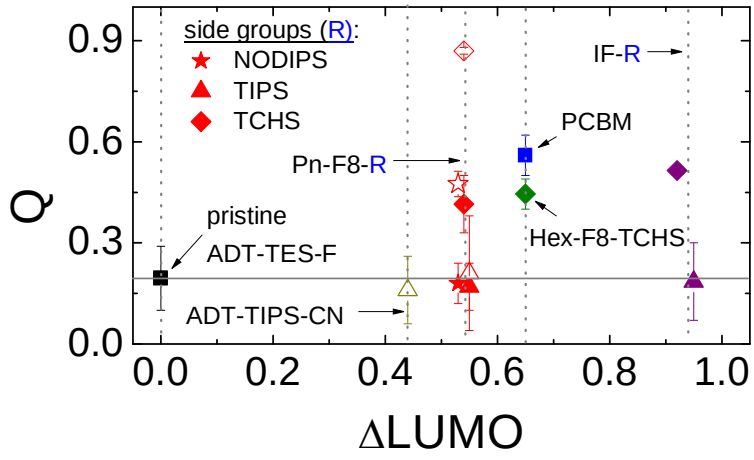

Figure 5.10: E-field-assisted PL quenching (Q) at 100 kV/cm in pristine ADT-TES-F donor films (ΔLUMO = 0) and in composite films. Filled and open symbols correspond to the donor exciton and exciplex emission, respectively. Considerably higher values of *Q* are observed in composites with larger D/A separation.

To explore the propensity of emissive states to dissociate under applied *E*-fields, we measured PL spectra at various E-fields and obtained the E-field-assisted PL quenching parameter $Q(E)=1-I_{PL}(E)/I_{PL}(0)$, where $I_{PL}(E)$ and $I_{PL}(0)$ are integrated PL

spectra at the field value *E* and in the absence of an applied electric field, respectively. The spectral data were integrated in the PL spectral ranges of the donor and, when applicable, of the exciplex. Considerably higher E-field-assisted quenching *Q*, of both donor exciton and exciplex emission (filled and open symbols in Fig. 5.10, respectively), was observed in composites with larger D/A separations, such as those with PCBM (Fig. 5.9) or derivatives with TCHS (Figs. 5.8 and 5.9) or NODIPS side groups, as compared to those with derivatives with TIPS side groups or pristine donor films (Figs. 5.7 and 5.8). It should be noted that no significant changes in absorption spectra were observed with applied E-field, suggesting that any changes in PL spectra with an applied E-field are related to exciton dynamics. In addition, a reduction in the PL lifetimes, of both the exciplex and donor exciton, with an increase in E-field, was observed in all samples. For example, the PL lifetimes of the exciplex in composites with Pn-F8-NODIPS (Pn-F8-TIPS) decreased from 3.4 ns (4.6 ns) in the absence of an E-field to 2.5 ns (3.8 ns) at 100 kV/cm (inset, Fig. 5.8(b)). Under similar conditions, the PL lifetimes of the donor exciton in composites with PCBM (pristine donor films) decreased from 1.8 ns (1.3 ns) to 1.2 ns (1.1 ns). These observations confirm that most of the PL quenching *Q* in Fig. 5.10 is due to the exciplex and donor exciton dissociation. In the case of the exciplex, the increase in *Q* with a larger D/A separation is consistent with a smaller exciplex binding energy resulting from the larger separation and, thus, more efficient dissociation under E-fields. The similar trend in Q for the donor exciton suggests that in composites with large D/A separation, excitons on donor molecules near the D/A interface contribute significantly to the PL

and are considerably more prone to dissociation, as compared to donor excitons in pristine donor films or in composites with acceptors that have TIPS side groups.

A reduction in the amplitude, C, obtained from fits of PL lifetime data without an applied E-field and at an E-field of 100 kV/cm, was also observed (e.g. inset of Fig. 5.8(b)), both for the exciplex and donor exciton. This reduction in the amplitude was more pronounced in composites with a larger D/A separation; for example, an amplitude reduction of ~11% (~1%) in composites with the Pn-F8-NODIPS (Pn-F8-TIPS) exciplex and of ~20% (~8%) in the donor exciton in the composite with PCBM (pristine donor films) was observed. This suggests that the efficiency of E-field-assisted dissociation of a state, which is a precursor to both exciplex and donor exciton formation, is also affected by the D/A separation.

5.3.4 Charge Carrier Generation and Recombination in Transient Photocurrents in Composite Films

To understand the relationship between the exciton dissociation (both exciplex and donor exciton) observed in PL and charge carrier photogeneration, we measured photocurrents in films under pulsed (355 nm, 500 ps) photoexcitation as a function of applied *E*-field. In pristine donor films, at all values of applied *E*-field, transient photocurrents (I_{ph}) with a sub-0.6 ns rise time, limited by the time resolution of the setup, were obtained (Table 5.1 and Fig. 5.11). This indicates fast (most likely sub-30 ps) [34, 37] charge carrier photogeneration, consistent with previous studies of similar films [35, 37, 38]. Since charge photogeneration occurred faster than donor exciton dissociation times, obtained from PL lifetime data at all *E*-fields, most of the

photogenerated carriers contributing to the peak of I_{ph} originated from the dissociation of a state which is a precursor to the emissive donor exciton [35]. After peak photogeneration, the I_{ph} transient exhibited a fast initial decay, due to carrier trapping and recombination, followed by a slow power-law decay that persisted up to at least ~2 μs, consistent with previous studies [37, 39].

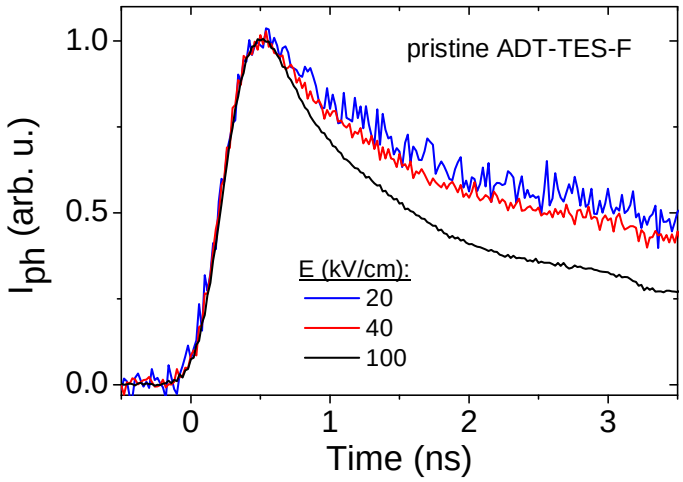

Figure 5.11: Transient photocurrent (I_{ph}) in a pristine ADT-TES-F donor film at multiple values of applied E-field. The rise time of the I_{ph} is <0.6 ns, limited by the time resolution of the setup, at all electric fields.

In composites with small D/A separation (acceptors with TIPS side groups), a sub-0.6 ns rise time of the I_{ph} was observed at all *E*-fields ($t_{ph,max}$ <0.6 ns, Table 5.1 and Fig. 5.12(a)), similar to pristine donor films. Thus, most of the photogenerated carriers contributing to the peak of I_{ph} were produced by dissociation of a state that is a precursor to the donor exciton, as in pristine donor films, and the contribution of exciplex dissociation to I_{ph} was small. In contrast, in composites with a larger D/A separation, the rise time of I_{ph} was highly *E*-field dependent (Figs. 5.12(b) and Table

5.1). For example, in composites with Pn-F8-TCHS or Pn-F8-NODIPS acceptors, the peak of I_{ph} at 20 kV/cm occurred at $t_{ph,max}$~2.3 and 3.2 ns, consistent with the time scales of exciplex lifetimes in Pn-F8-R composites (Fig. 5.8(b)), whereas the charge photogeneration was considerably faster (<0.6 ns) at 100 kV/cm. Interestingly, at 20 kV/cm, a similarly slow photocurrent rise (with $t_{ph,max}$ ~2.2-3.2 ns) was observed in composites that did not exhibit any exciplex emission (i.e. those with Hex-F8-TCHS, PCBM, and IF-TCHS acceptors (Table 5.1 and Fig. 5.13)). This suggests the existence of a non-emissive CT state with a lifetime >2 ns in these composites.

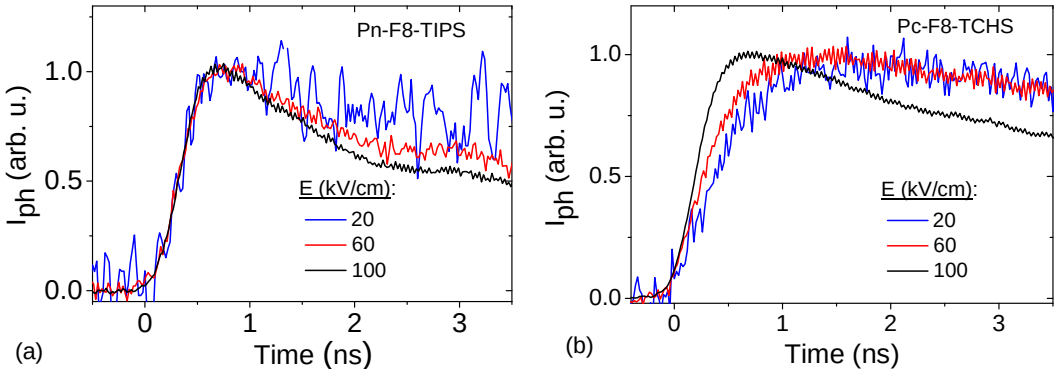

Figure 5.12: Transient photocurrents (I_{ph}) at multiple values of applied E-field in composite films with (a) Pn-F8-TIPS and (b) Pn-F8-TCHS acceptors. I_{ph} was measured under 355 nm, 500 ps pulsed excitation. The currents shown are normalized by their peak values. In Pn-F8-TCHS composites the photocurrent is electric field-dependent; it is slow at low electric fields and becomes limited by the time resolution of the setup at high electric fields.

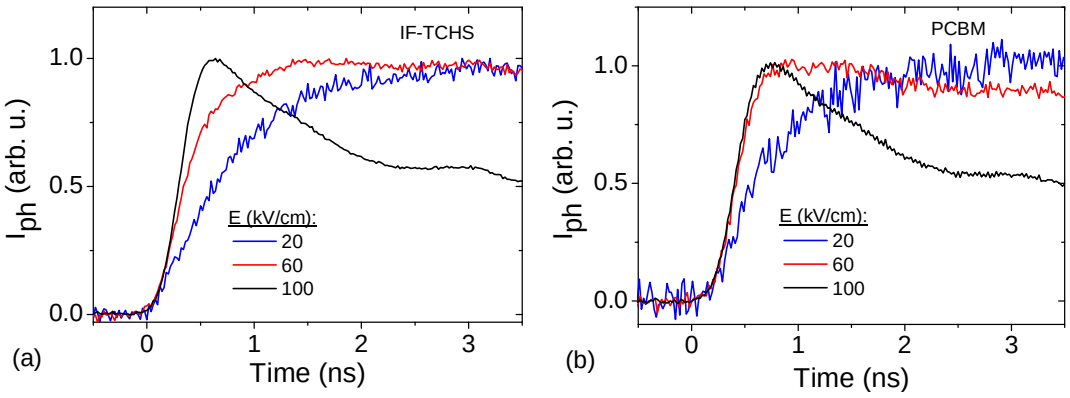

Figure 5.13: Transient photocurrent (I_{ph}) in composite films with (a) IF-TCHS and (b) PCBM acceptors, at multiple values of applied E-field. I_{ph} was measured under 355 nm, 500 ps pulsed excitation. The currents shown are normalized by their peak values.

Regardless of the emission properties of the CT exciton in our composites, the following picture of nanosecond time-scale charge photogeneration emerged. The photoexcitation of the donor results in the formation of a precursor state to the donor exciton followed by the competition between sub-0.6 ns charge carrier photogeneration, and CT exciton formation. At low *E*-fields (≤60 kV/cm), the CT exciton formation prevails and is followed by slow charge carrier generation via *E*-field-assisted dissociation. Since the CT exciton dissociation is more efficient in composites with a larger D/A separation, a small improvement in charge photogeneration (of up to factor of 2 at 40 kV/cm, depending on the ΔLUMO, filled symbols in Fig. 5.14) is observed in these composites as compared to pristine donor films. In contrast, the CT exciton dissociation is not efficient in composites with acceptors having TIPS side groups, and, thus, a reduction in charge photogeneration efficiency is observed (Fig. 5.14, 40 kV/cm). At high *E*-fields (>60 kV/cm), fast

carrier photogeneration dominates over the CT exciton formation in all composites, and no increase in charge photogeneration efficiency in composites as compared to pristine donor films is observed (open symbols in Fig. 5.14, 100 kV/cm).

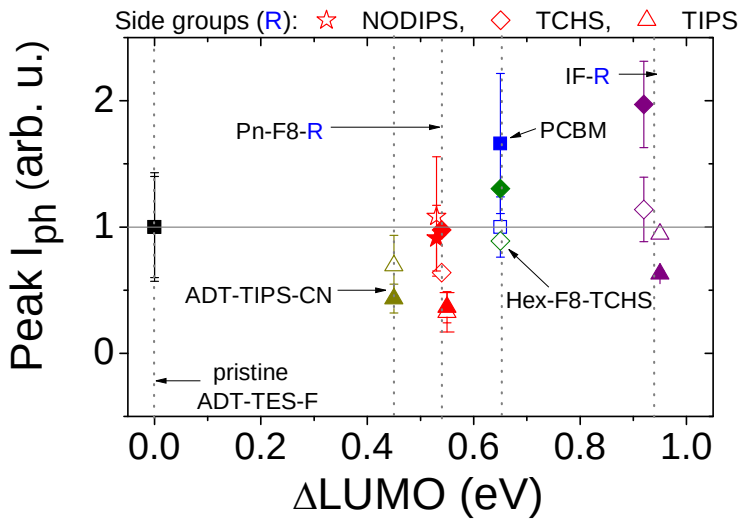

Figure 5.14: Peak transient photocurrents (I_{ph}) obtained in composite films at 40 kV/cm (filled symbols) and 100 kV/cm (open symbols). I_{ph} was measured under 355 nm, 0.18 μJ/cm^2 , 500 ps excitation. The values shown are normalized by corresponding values measured in pristine ADT-TES-F donor films.

The data in Fig. 5.15 shows the effect of the acceptor on charge carrier recombination. In all composites with a larger D/A separation (i.e. with PCBM or derivatives with TCHS or NODIPS side groups), the initial decay of the transient photocurrent was considerably slower than that in pristine donor films or in composites with acceptors that have TIPS side groups, indicative of inhibited charge recombination. For example at 100 kV/cm, only ~11% of initially generated charge carriers remained mobile at ~10 ns in the pristine donor films; this number increased to ~45% in composites with Pn-F8-TCHS and PCBM acceptors and to 53% in those with IF-TCHS. Figure 5.16 shows the amount of mobile charge obtained by

integrating photocurrent transients measured at 80 kV/cm over the time-scale of ~2 μs in composites, normalized by that in pristine donor films. In all composites, the inhibited recombination led to a higher total charge, as compared to that in pristine donor films, with the highest increase (by a factor of ~4-12) in composites with a larger D/A separation (i.e. with PCBM and derivatives with TCHS side groups).

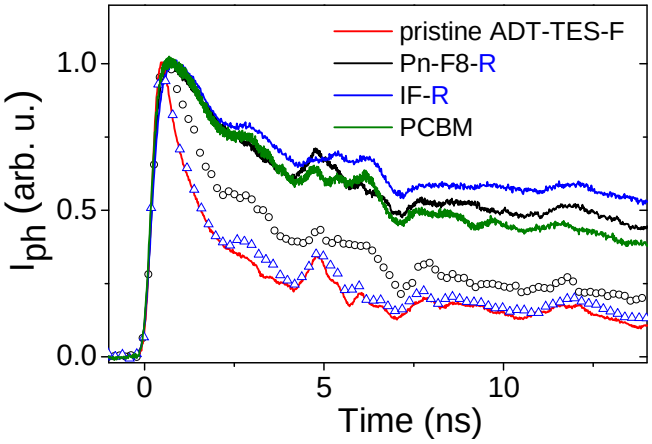

Figure 5.15: Normalized transient photocurrents in a pristine ADT-TES-F donor film and in composite films. Composite films with Pn-F8-R (black line and open squares for R = TCHS and TIPS, respectively), IF-R (blue line and open triangles for R = TCHS and TIPS, respectively), and PCBM (green line) are shown.

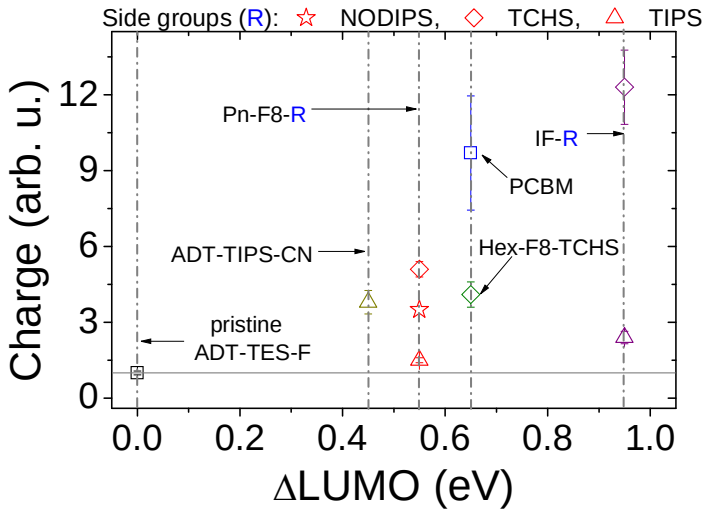

Figure 5.16: Total mobile charge in composite films, normalized to values in pristine ADT-TES-F donor. The charge was obtained by integrating transient photocurrents, measured under 355 nm, 500 ps, 0.18 μJ/cm^2 pulsed excitation at 80 kV/cm, over ~2 μs.

5.3.5 Cw Photocurrent in Composite Films

Figure 5.17 shows cw photocurrents (I_{cw}) obtained at 532 nm and ~370 nm excitation (filled and open symbols, respectively) at an *E*-field of 40 kV/cm in composites, normalized by those in pristine donor films. An increase in I_{cw} was observed in all composites as compared to pristine donor films, with a larger increase (by a factor of 5-10) achieved in composites with a larger D/A separation (i.e. those with PCBM or derivatives with TCHS side groups), as compared to that of a factor of 1.8-2.5 in composites with smaller D/A separation (i.e. those with derivatives that have TIPS side groups). In keeping with the insights obtained from time-resolved photocurrents in Fig.5.14 and 5.16, we attribute most of the increase in I_{cw} in composites to inhibited charge recombination, rather than to improved

photogeneration efficiency. The overall trends in I_{cw}, at both wavelengths of excitation, can be summarized as follows: (i) no particular dependence of I_{cw} on the ΔLUMO in composites with large D/A separation and a slight increase in I_{cw} with ΔLUMO (by a factor of ~1.5 from a ΔLUMO of 0.44 eV to 0.95 eV) in composites with small D/A separation and (ii) considerably stronger dependence of the I_{cw} on the D/A separation as compared to effects of the ΔLUMO.

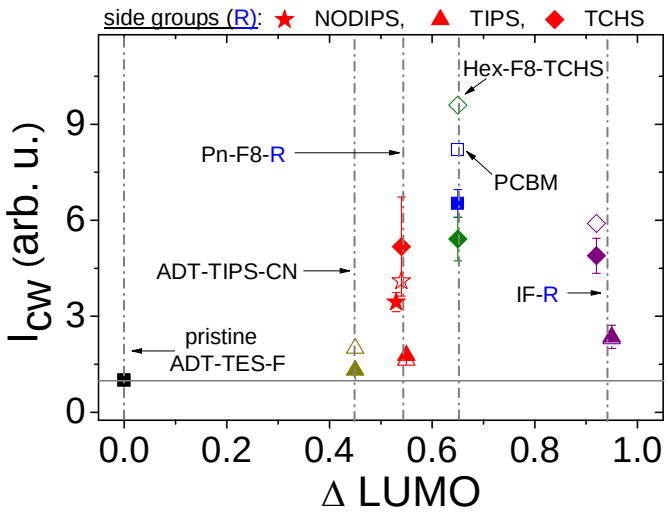

Figure 5.17: Photocurrents (I_{cw}) obtained under 532 nm (filled symbols) and ~370 nm (open circles) photoexcitation. The currents were measured at 40 kV/cm, and are normalized by corresponding values measured in pristine ADT-TES-F donor films.

5.4 Conclusion

In summary, the physical picture for the D/A charge transfer and photogeneration in the composite systems under study was determined, as depicted in Fig. 5.18. After photoexcitation (355 nm, 3.5 eV) at energies well above the absorption edge (~600nm, 2.1eV), competition between ADT-TES-F exciton formation (blue dotted lines) and charge transfer to either an emissive CT state

(exciplex) or a non-emissive CT state (referred to as CT state) occurred (k_{exc} or k_{CT} in Fig. 5.18). The type of charge transfer, was dictated by ΔLUMO, where exciplex formation was observed for ΔLUMO <0.6 eV and CT state formation was observed for ΔLUMO>0.6 eV. Under an applied *E*-field, a third competing process, fast (sub-0.6ns) charge carrier generation (η), was observed in all composites. The competition between these pathways was dependent on both E-field and D/A separation. After exciton formation occurred (either donor, exciplex, or CT state), E-field assisted PL quenching of the emissive exciplex and of the donor exciton was dramatically dependent on the D/A separation.

In composites with large D/A separation, substantial E-field-assisted PL quenching (Q) was observed, and the existence of a second charge carrier generation pathway, which was E-field dependent (η(E), Fig. 5.18(b)) appeared; this pathway was attributed to the dissociation of the exciplex or CT state. At low E-Field values, photoexcitation followed by charge transfer to the exciplex or CT state, and then charge carrier generation, η(E), was dominant (Fig. 5.18(b)). This carrier generation pathway resulted in up to a factor of ~2 increase in the peak photocurrent at 40kV/cm, as compared to that in pristine donor films (Fig. 5.14). However, in composites with small D/A separations, there was minimal PL quenching, and the second charge carrier pathway was not observed. At all values of E-field in the small D/A separation composites, sub-0.6 ns charge carrier photogeneration, η, was dominant (Fig. 5.18(a)).

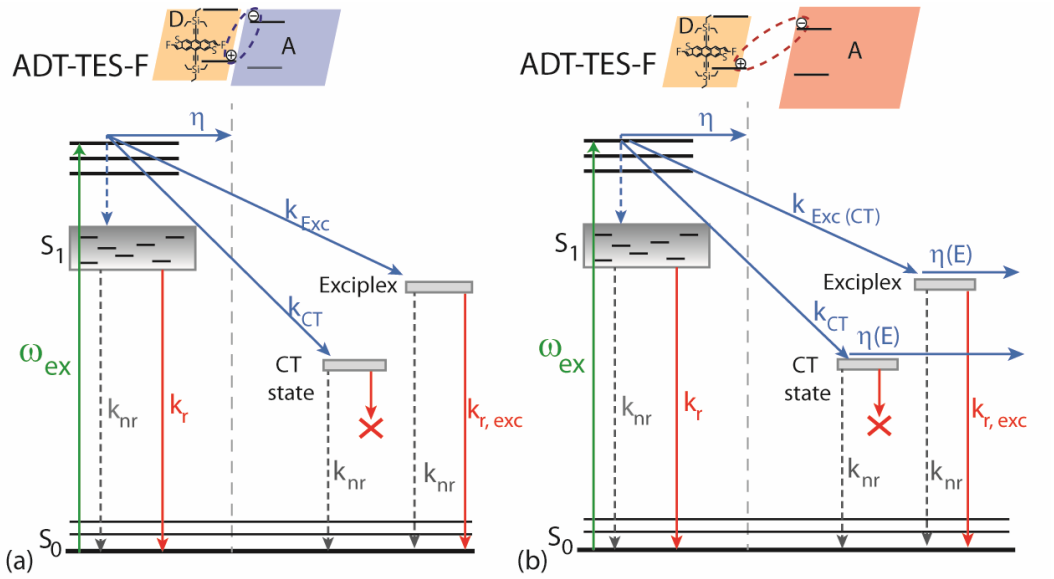

Figure 5.18: A diagram of exciton dynamics and charge carrier photogeneration pathways in the D/A composites films. Diagrams are shown for composites with small (a) and large (b) D/A separations. In both cases excitation (ω_{ex}) is followed by fast charge carrier generation (η), ADT-TES-F (donor) exciton formation (blue dotted line) , or charge transfer to either an exciplex (k_{Exc}) or CT state (k_{CT}) (depending on the ΔLUMO). In the case of small D/A separation (a) only fast charge carrier generation contributes to photocurrents. However, for composites with large D/A separations (b) exciplex or CT state dissociation leads to a slower charge generation process which contributes significantly to photocurrents at low E-field values. Radiative and nonradiative rate constants are also shown (k_{nr} and k_r).

After charge carrier generation, dramatic changes in charge carrier recombination dynamics that were dependent on the D/A separation were observed. These changes contributed up to a factor of 5-10 improvement in cw photocurrents in composites with large D/A separation, as compared to those in pristine donor films. Our studies show that it is possible to control properties of CT states and their contribution to the photocurrent by optimizing morphology of the D/A interface. In particular, both CT dissociation and charge recombination can be effectively manipulated by adjusting the molecular interaction between the donor and acceptor by

changing the size of the substituent on the acceptor, without a need to increase ΔLUMO (at least for ΔLUMO >0.5 eV) to improve the photocurrents. In applications that rely on applied *E*-fields, it should be possible to manipulate contributions of CT excitons to the photocurrent by changing the E-field and thus tune charge photogeneration dynamics and efficiency to satisfy particular requirements.

6 Resonant Enhancement of the Optical Tweezer Trapping Force

6.1 Introduction to Optical Tweezers

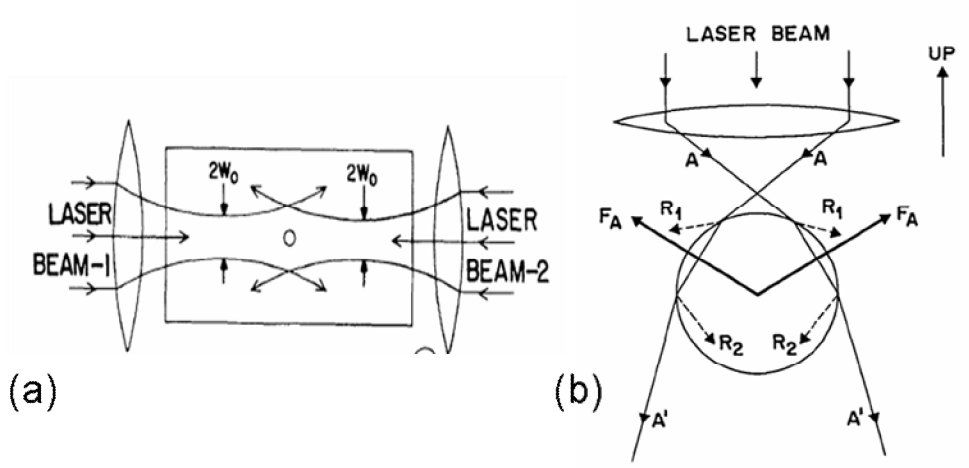

Figure 6.1: (a) Diagram of the experimental setup of the first optical trap experiments performed by Ashkin, figure taken from [98]. (b) Diagram of an optical tweezer trap, taken from [99].

In 1970 Aurthor Ashkin showed that continuous wave laser light could be used to accelerate and trap micron-sized particles [98]. In this pioneering work Ashkin used a single laser beam focused through a lens to accelerate polystyrene microspheres along the path of propagation of the laser light. He also showed that microspheres could be trapped in three dimensions (3-D) with the addition of a second focused laser beam counter propagating against the first laser beam (Fig. 6.1(a)). In 1986 Ashkin followed his initial work with the development of the single-beam gradient optical trap (Fig. 6.1(b)), referred to as optical tweezers [99]. With optical tweezers, a single laser beam focused with a high numerical aperture (NA) lens could be used to optically trap and manipulate particles on the micrometer and nanometer scales.

Since their invention optical tweezers have been used extensively in many applications spanning chemistry, biology, engineering, and physics [100]. The majority of the work done with optical tweezers has involved micron-sized dielectric particles which can be trapped with low- to moderate-power lasers. Optical tweezers with particles on this size scale have been used in experiments that include observing mechanical properties of DNA [101], measuring forces produced by molecular motors [102], micromachining, and assembling both ordered arrays and 3-D structures of particles [103]. However, experiments done with nanometer-sized particles, or 'nanoparticles', are limited [99, 104]. Given the recent emphasis on nanotechnology and the desire to design experiments on the nanoscale, there is motivation to trap and manipulate particles on this scale. Furthermore, the ability to not only confine nanoparticles but to further suppress their natural Brownian motion to the nanometer and sub-nanometer scales is desirable. One possible application is a nanometer-sized fluorescent probe for biological experiments. Such an application would require spatial control of the nanometer-sized probe with high precision without using large laser powers, to avoid damaging the object under observation. However, adapting optical tweezers for applications on the nanoscale is difficult because the trapping force on nanoparticles scales with the volume of the particle [104]. Thus, under the same conditions, the force acting on a 1 nm particle is 10^6 times smaller than the force on a 100 nm particle.

A possible method to increase the trapping force exerted on nanoparticles would be to exploit optical resonances. For example, atoms, on the sub-nanometer

scale, have been successfully trapped using optical tweezers [105]. The reason that atoms can be trapped is that the wavelength of the trapping laser can be tuned close to a strong resonance transition where the optical response of the atom is enhanced. Resonances in transparent dielectric spheres are in the ultraviolet, far from the typical near-infrared wavelengths used in optical tweezers. Potential candidates for resonance-enhanced optical trapping include metallic nanoparticles, metal-dielectric nanoshells, quantum dot nanocrystals, chromophore-doped nanoshells, dye-doped dielectric particles, and carbon nanotubes. In all of these cases, we can tune the laser wavelength to match the optical response and thus enhance the optical forces. An even more exciting prospect is that in many cases we can tune the particle's optical response through synthesis to a range of wavelengths that includes a desired trapping wavelength [106-110].

This chapter is dedicated to optical tweezer based studies, and is organized as follows: in Section 6.2, the theory of optical tweezer trapping forces acting on a sphere of arbitrary size will be presented, as well as the theory of resonant enhancement of the optical tweezer force. In Section 6.3, experiments and numerical simulations conducted on the resonance enhancement of the optical tweezer force on polystyrene spheres doped with dye are presented. In Section 6.4 a preliminary study using pH/ion-sensitive particles is discussed. In Section 6.5 initial results for optical tweezer based effective charge measurements are described.

6.2 Theory

The force acting on a particle in an optical tweezer trap is a result of the transfer of momentum between the highly focused laser light and the particle. The forces acting on a spherical particle of arbitrary size can be determined analytically using electromagnetic scattering theory. For spherical particles much smaller or much larger than the wavelength of the trapping light, approximations can be applied to make calculation of the trapping force less intensive. In addition, when using these approximations to calculate the trapping force ($\boldsymbol{F}_{trap}$) it is possible to separate the force into three components: the scattering force ($\boldsymbol{F}_{scat}$), the absorption force ($\boldsymbol{F}_{abs}$), and the gradient force ($\boldsymbol{F}_{grad}$), where $\boldsymbol{F}_{trap} = \boldsymbol{F}_{grad} + \boldsymbol{F}_{scat} + \boldsymbol{F}_{abs}$ [111]. The gradient force attracts the particle towards the high intensity focus of the trap, to trap the particle, and acts as a restoring force when the particle is displaced from equilibrium. The scattering and absorption forces act in the direction of propagation of the laser, pushing the particle away from the high intensity focus. Stable trapping in three dimensions is possible if the gradient force exceeds the combined scattering and absorption forces [112]. When performing calculations using rigorous electromagnetic (EM) theory, the trapping force can not be easily separated into the scattering, absorption, and gradient forces, but qualitatively the gradient of the field traps the particle, while scattering and absorption destabilize the trap.

6.2.1 Optical Tweezer Force on an Arbitrary Sized Sphere

To calculate the forces acting on an arbitrarily sized sphere, EM scattering theory must be employed to determine the EM fields scattered from the sphere in the trap. Lorentz-Mie theory can be used to obtain an analytical solution of the scattered fields from a sphere, given incident plane wave EM radiation [113, 114]. However, optical tweezers are created using highly focused light. Several techniques have been developed to extend the Lorentz-Mie theory to fields scattered from a sphere with arbitrary incident EM fields, including the Generalized Lorentz-Mie Theory (GLMT) and the T-Matrix method [115].

In the case of optical tweezers, the incident EM field is typically a highly focused Gaussian-profiled, or TEM_{00}, laser beam. A significant amount of research has been conducted on calculating the EM fields and forces in optical tweezers acting on a spherical particle using GLMT and T-Matrix methods, which are identical for spherical particles [116, 117]. In both these methods, the incoming highly focused Gaussian field is expressed as an expansion of vector spherical wave functions (VSWFs), which are functions of spherical Bessel functions [118]. The expansion coefficients of the VSWFs that define the fields of the incoming Gaussian beam are determined using a point matching algorithm in the far field [119]. The EM field scattered from the particle (i.e. outgoing field) can then be determined from the incoming field using the T-matrix method [115]. For example, Nieminen et al. [120] presented the incoming and outgoing fields ($\boldsymbol{E}_{in}$ and $\boldsymbol{E}_{out}$, respectively) in terms of VSWF and expansion coefficients as follows:

$$\boldsymbol{E}_{in} = \sum_{i=1}^{\infty} \sum_{j=-i}^{i} a_{ij} \boldsymbol{M}_{ij}^{(2)}(k_m \boldsymbol{r}) + b_{ij} \boldsymbol{N}_{ij}^{(2)}(k_m \boldsymbol{r}), \tag{6.1}$$

$$\boldsymbol{E}_{out} = \sum_{i=1}^{\infty} \sum_{j=-i}^{i} p_{ij} \boldsymbol{M}_{ij}^{(1)}(k_m \boldsymbol{r}) + q_{ij} \boldsymbol{N}_{ij}^{(1)}(k_m \boldsymbol{r}), \tag{6.2}$$

where $k_m = 2\pi/\lambda_m$ is the wavenumber in the surrounding medium, $\boldsymbol{r}$ is the position vector, $\boldsymbol{M}^{(l)}_{ij}$ and $\boldsymbol{N}^{(l)}_{ij}$ are the VSWFs, and a_{ij}, b_{ij}, p_{ij}, and q_{ij} are the expansion coefficients. With expressions for the incoming and outgoing EM fields, given by Eqs. 6.1 and 6.2 respectively, the forces acting on the sphere in the Gaussian beam can be calculated by evaluating the momentum transfer from the EM fields to the particle, because the change in momentum of the particle must equal the change in momentum of the fields. This change in momentum, and thus the trapping force, can be calculated by taking a surface integral of the Maxwell stress tensor over a spherical surface in the far field. In particular, the force acting in the direction parallel to the propagation of laser light (taken here as the *z*-direction) in SI units is [121]

$$\begin{aligned} F_z = \frac{2n_m}{c} \sum_{i=1}^{\infty} \sum_{j=-i}^{i} & \frac{j}{i(i+1)} \mathrm{Re}\left(a_{ij}^* b_{ij} - p_{ij}^* q_{ij}\right) \\ & - \frac{1}{i+1} \left[\frac{i(i+2)(i-j-1)(i+j+1)}{(2i+1)(2i+3)}\right]^{1/2} \\ & \times \mathrm{Re}\left(a_{ij} a_{i+1,j}^* + b_{ij} b_{i+1,j}^* - p_{ij} p_{i+1,j}^* + q_{ij} q_{i+1,j}^*\right) \end{aligned} \tag{6.3}$$

where n_m is the index of refraction of the surrounding medium, and c is the speed of light. The forces in the transverse direction (i.e. *x*-and *y*-directions) are obtained using the same expressions for the EM fields (Eqs. 6.1 and 6.2) by rotating the coordinate

system and defining new coefficients a_{ij}, b_{ij}, p_{ij}, and q_{ij} in the rotated frame of reference [117, 122]. In the two limiting cases, $d >> \lambda$, and $d << \lambda$, where d is the sphere diameter and λ is the wavelength of the trapping light, the expressions for the trapping force are simplified, as described below.

6.2.2 Geometrical Optics Regime ($d >> \lambda$)

In the geometric optics regime ($d >> \lambda$), the focused light that creates the optical tweezer trap can be described as an infinite number of rays that are incident on, and interact with, the particle at different angles, where the range of angles is determined by how strongly the light is focused. When each ray strikes the surface of the sphere, a portion of the light is scattered, a portion is absorbed, and a portion is transmitted. The relative amplitudes of the light that is scattered, transmitted, or absorbed depend on the index of refraction of the particle. The light that is reflected and absorbed by the sphere results in radiation pressure, or the scattering and absorption forces, that act in the direction of propagation of the light. The transmitted light is refracted, resulting in a change in momentum as it enters and exits the sphere, which, according to Newton's third law, imparts an equal and opposite change in momentum to the particle. This change in momentum resulting from the refraction of the transmitted light is proportional to the force that confines the sphere and is referred to as the gradient force. In the geometric optics regime, a concise form of the total force (combining scattering and gradient forces) acting on a dielectric sphere when in an optical trap has been given by Ashkin [123]. The expressions for the force in Ref.

[123] show that rays incident at large angles contribute more to the gradient (and thus the trapping) force than those incident at small angles, with a maximum contribution from rays incident at an angle near 70^o [124]. This dictates the choice of high numerical aperture objectives for optical tweezer traps.

6.2.3 Rayleigh Regime ($d<<\lambda$)

In the Rayleigh regime ($d<<\lambda$), the reaction of the particle to the incident EM field at any instant in time is approximately constant throughout the particle. The particle can then be approximated as a point dipole. In this regime, the trapping force acting on the dipole can succinctly be broken up into three components: the scattering force, the absorption force, and the gradient force. In the case of a sphere, the scattering and absorption forces ($\boldsymbol{F}_{scat}$ and $\boldsymbol{F}_{abs}$, respectively) acting on the particle in the trap are [104]

$$\boldsymbol{F}_{scat} = \hat{\boldsymbol{k}}\left(\frac{n_m}{c}\right)C_{scat}\cdot I = \hat{\boldsymbol{k}}\frac{4\pi^3 n_m}{c\varepsilon_o^2\lambda^4}\left|\alpha\right|^2\cdot I \tag{6.4}$$

$$\boldsymbol{F}_{abs} = \hat{\boldsymbol{k}}\left(\frac{n_m}{c}\right)C_{abs}\cdot I = \hat{\boldsymbol{k}}\frac{2\pi}{c\varepsilon_o\lambda}\mathrm{Im}\left(\alpha\right)\cdot I \tag{6.5}$$

where C_{scat} and C_{abs} are the scattering and absorption cross sections, ε_o is the dielectric constant in vacuum, α is the complex polarizability of the sphere, $\hat{\boldsymbol{k}}$ is the unit vector in the direction of propagation of the laser beam, and I is the intensity of trapping

light. The polarizability of the sphere is related to the index of refraction by the Clausius-Mossotti equation (in SI units) [125]

$$\alpha = 4\pi\varepsilon_m \left(\frac{d}{2}\right)^3 \left(\frac{m^2 - 1}{m^2 + 1}\right) \tag{6.6}$$

where ε_m is the dielectric constant, in SI units, of the surrounding material and m is the relative complex index of refraction, which is the ratio of the index of refraction of the sphere (n_s) to the index of refraction of the surrounding material (n_m). The third force acting on the sphere is the gradient force $\boldsymbol{F}_{grad}$ [126],

$$\boldsymbol{F}_{grad} = \frac{\mathrm{Re}(\alpha)}{c n_m \varepsilon_o} \nabla I \tag{6.7}.$$

The trapping force on the sphere is the vector sum of $\boldsymbol{F}_{grad}$, $\boldsymbol{F}_{scat}$, and $\boldsymbol{F}_{abs}$. In the Rayleigh regime, the scattering force, which depends on the volume of the particle squared, is small compared to the gradient force, which depends on the volume (Eqs. 6.4, 6.5, and 6.7). Furthermore, it can be seen from Eqs. 6.5-6.7 that an increase in the trapping force can be obtained if the polarizability can be adjusted such that there is an increase in the real part of the polarizability, and hence $\boldsymbol{F}_{grad}$, without a substantial increase in the imaginary part, and $\boldsymbol{F}_{abs}$.

6.2.4 Resonant Enhancement of Optical Tweezer Trapping Force

Regardless of the sphere size, the force acting on a trapped particle depends on the complex index of refraction of the material. The real part of the index of

refraction, the refractive index, *n*, is attributed to reflection and refraction, and the imaginary part, the extinction coefficient, κ, to absorption [127]. The behavior of the complex index in the vicinity of a resonance is illustrated in Fig. 6.2(a), which was calculated using the classic electron oscillator model [128]. The corresponding polarizability of a sphere with a diameter of 50 nm is calculated using Eq. 6.6 and is shown in Fig. 6.2(b). On the red side of resonance (e.g. >790 nm in Fig. 6.2) the increase in the real part of the polarizability exceeds the increase in the imaginary part, so that the increase in the gradient force due to resonance is larger than the increase in the absorption force, resulting in an enhancement in the trapping force.

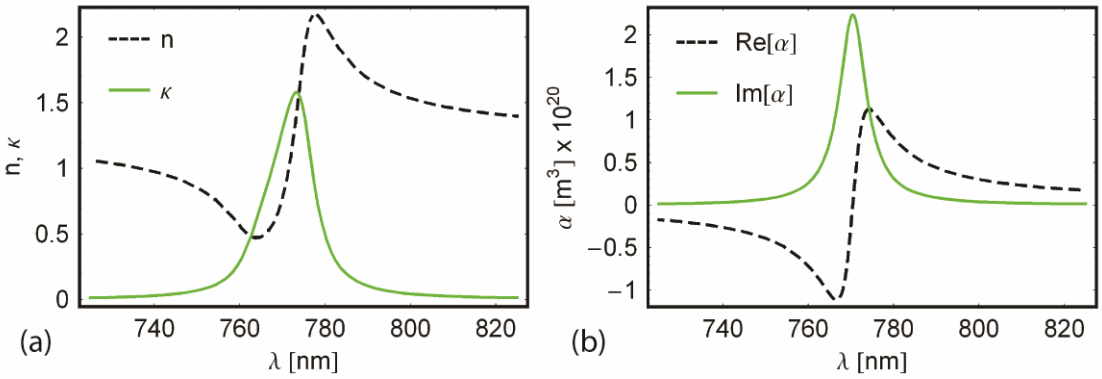

Figure 6.2: (a) The real and imaginary parts (n and κ, respectively) of the complex index of refraction near resonance, obtained from the classic electron oscillator model of the dielectric constant. (b) The real and imaginary parts of the polarizability, α in units of meters squared near resonance, calculated using the complex index of refraction in (a) and the Clausius-Mossotti equation (Eq. 6.6). Both (a) and (b) show that there is an increase in either the real part of the index of refraction (i.e. in the refractive index *n*) or the real part of the polarizability on the red side of the resonance, which can be related to the forces acting on a particle in an optical trap.

Enhancement in the gradient force on the red side of an optical resonance has been exploited in the past to trap atoms and molecules on the sub-nanometer scale

[105, 129]. More recently, plasmon resonant particles ranging in size between 18 and 254 nm have been trapped experimentally with optical tweezers at wavelengths on the red side of resonance [112, 130, 131]. The applicability of the enhancement of the trapping force on nanometer-sized nonmetallic absorbing spheres has also been explored theoretically, and the possibility of up to an order of magnitude increase was predicted [132].

The work presented in *Section 6.3* is based on the exploration of the possible resonant enhancement in the optical tweezer force acting on particles doped with dye. The ability to increase the trapping force on these particles without having to increase the power of the trapping laser is attractive for applications in samples that are susceptible to photo damage at high laser intensities. Another desirable feature that would result from increasing the trapping force through optical resonance, would be the further suppression of the natural Brownian motion the particle undergoes within the trap, which would increase the potential spatial resolution in a optical tweezer based probe.

6.3 Wavelength Dependence of Optical Tweezer Forces on Dye-Doped Polystyrene Spheres

To explore the possibilities of resonance-enhanced optical trapping, we initially conducted experiments with polystyrene spheres doped with various dyes and performed numerical calculations of the trapping forces. The aim of these experiments and calculations is to study the additional force contributions from the resonance of the dye that is added to spheres, in particular, the wavelength

dependence. These spheres are a model system to quantitatively explore this resonance effect on the trapping force, as they have been used extensively in optical tweezers, and the forces on transparent polystyrene spheres are well understood.

6.3.1 Experiments

To quantitatively explore the wavelength dependence of optical forces in the vicinity of a resonance we have conducted experiments using 1μm polystyrene spheres doped with dye. We used micron-sized spheres because they are widely used in many optical tweezer applications, and techniques for trapping and measuring the optical trapping force on them are well documented [111, 133, 134]. In our experiments we measured the trapping force at multiple wavelengths near the dye resonance. The experiments were conducted to explore the effect of resonant enhancement on the trapping force at wavelengths on the blue-side of resonance, on resonance, and on the red side of resonance. As a control, similar measurements were taken on polystyrene spheres without dye, which have no optical absorption at the wavelengths where measurements were taken.

The dyed particles used in our experiments had peak absorption at wavelengths close to the tunability range of the trapping laser. The three types of particles we used were all 1 μm in diameter and had peak absorption at wavelengths of 625 nm (Crimson Spheres, Molecular Probes, Inc), 775 nm (Duke Scientific, Inc), and 840 nm (Duke Scientific, Inc); later referred to as ‘625 nm’, ‘775 nm’, and ‘840 nm’ spheres, respectively. We independently measured the extinction spectra of dyes used in the

‘775 nm’ and ‘840 nm’ spheres after extracting the dye from the spheres by dissolving them in acetone and filtering the solution using a 200 nm pore. The extinction spectra in Fig. 6.3 show that the dyes used in the ‘775 nm’ and ‘840 nm’ spheres have peak absorption in acetone at 760 nm and 825 nm, respectively. The inset in Fig. 6.3 shows the extinction spectrum of the ‘840 nm’ spheres in a deionized water (di-H_2O) suspension. The spectrum of the dye-doped spheres is red shifted by ~15 nm and broadened, as compared to that of the dilute solution of the same dye in acetone (Fig. 6.3), due to aggregation effects. Similar effects were observed in the ‘775 nm’ spheres as well. We also verified that the dye was loaded in the spheres, and not in the solution, by filtering the dye-doped spheres from their di-H_2O suspension using a filter with a 200 nm pore size. Extinction spectra measurements were then taken of the solutions before and after filtering. The spectral data suggested that no discernable amount of dye existed in the solution. Polystyrene spheres with a diameter of 1 μm without dye (transparent) from Duke Scientific, Inc. were also used as a control. All spheres were obtained from the manufacturer as a suspension in di-H_2O at concentrations between 2% and 10% by weight. These suspensions were ultrasonicated and further diluted with di-H_2O, so that measurements could be taken without multiple spheres falling into the trap at the same time. Sample solutions were held between a microscope slide and cover slip in a securely sealed fluid chamber.

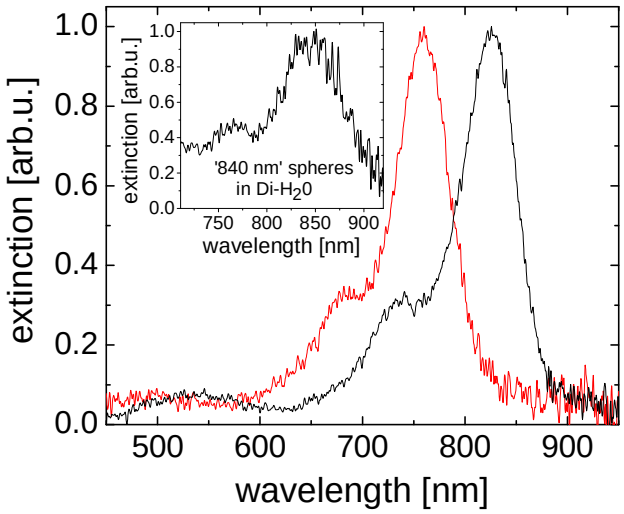

Figure 6.3: Extinction spectra of the dyes used in the '775 nm' and '840 nm' spheres in a dilute acetone solution, with peak absorption at 760 nm and 826 nm, respectively. The inset shows the spectrum of a Di-H_2O suspension of the '840 nm' spheres, which has a broadened peak that is red-shifted by ~16 nm, as compared to the same dye in the acetone solution.

Experimentally, optical tweezer trapping was performed in a custom inverted microscope assembly with an oil immersion microscope objective (Edmund Optics, 100X, NA 1.26, 160 mm tube length), as shown in Fig. 6.4. Particles were trapped with either a continuous wave (cw) Ti:Sapphire laser, tunable between 750 nm and 840 nm, or a diode laser (λ = 980 nm). The objective was placed on a 1-D stage (*z*-direction) to control the position of the trap in the sample. The sample was placed on a 2-D stage (*x*- and *y*-directions) to control trap position in the plane of the sample. The trapping laser light was steered using silver mirrors (M1 and M2) into a laser beam expansion lens pair (L2 and L4) so that the light was both focused at the tube length of the objective and overfilled the back aperture of the objective. For trap strength measurements, a Helium-Neon (He-Ne) laser (633 nm) and Hamamatsu

S4349 quadrant photodiode (QPD) were used to measure scattered light from the sphere undergoing Brownian motion in the trap [135]. The He-Ne laser light was steered to overlap with the trapping laser light into the objective and through a condenser using silver mirrors (M3 and M4). A hot mirror (D2) was used to reflect both the trapping laser and He-Ne light into the objective. The telescope lens pair (L3 and L4) was used to expand the He-Ne laser light. In addition the lens, L3, was placed on a stage to allow the focal plane of the He-Ne light to be finely adjusted within the sample (in the axial or z-direction). This made it possible to adjust the position of the focal plane relative to the particle in the trap to optimize the scattered light signal collected by the QPD. A short pass filter was used to filter the trapping laser light from the QPD, so that only the scattered light from the He-Ne was measured. The signal from the QPD was collected using a DAQ (NI-6221), and data acquisition was done using a custom LabView program. A halogen lamp and CCD camera were used to illuminate the sample and image particles.

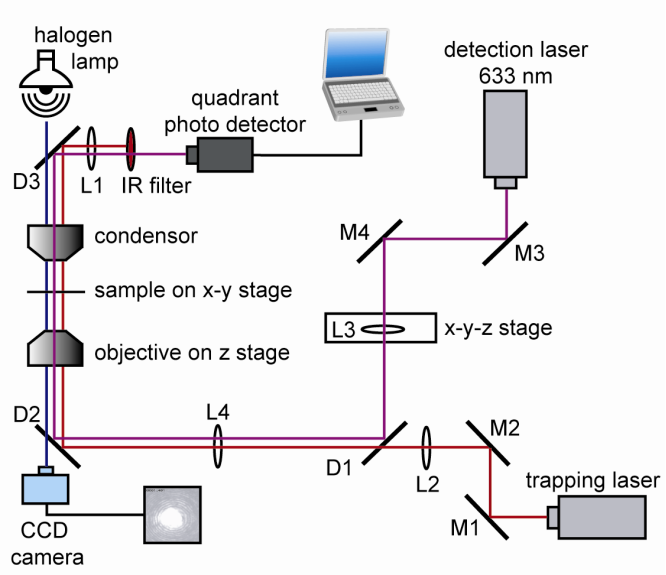

Figure 6.4: The experimental setup used to measure optical tweezer trap strength. Optical tweezer trapping was achieved by focusing either cw Ti:Sapphire laser light (tunable between 750 nm and 840 nm) or diode laser light (980 nm) with a high NA objective. A detection laser (He-Ne) and a quadrant photo detector were used to measure the suppressed Brownian motion of a particle in the trap, from which the trap strength can be obtained. Notations: L – lenses, D – dichroic mirrors, and M - mirrors.

For our measurements we define the *z*-direction as the direction of the propagation of the laser beam, and the *x*-and *y*- directions as transverse to the laser propagation. To measure the trap strength in the *x*-direction the time series of the particle undergoing Brownian motion within the trap was acquired (Fig. 6.5(a)) and analyzed. In our data analysis, we assumed that the trapping laser beam had a Gaussian intensity profile in the x-y plane. In the *x*- and *y*-directions, the scattering and absorption forces are zero (Eqs. 6.4 and 6.5), so that when displaced from equilibrium a small distance in the x-y plane the restoring force acting on a particle in the trap is

$$F_{\text{trap i}}\,\hat{i} = F_{\text{grad i}}\,\hat{i}\,, \tag{6.8}$$

where $i = x, y$. From Eq. 6.7 the restoring force on the particle in the x-y plane is then

$$F_{\text{trap x}}\,\hat{x} + F_{\text{trap y}}\,\hat{y} = \frac{\text{Re}(\alpha)}{cn_m\varepsilon_o}\left(\frac{\partial}{\partial x}\,\hat{x} + \frac{\partial}{\partial y}\,\hat{y}\right)I \tag{6.9},$$

which for the Gaussian beam becomes

$$F_{\text{trap x}}\,\hat{x} + F_{\text{trap y}}\,\hat{y} \propto \left(\frac{\partial}{\partial x}\,\hat{x} + \frac{\partial}{\partial y}\,\hat{y}\right)e^{-(x^2+y^2)/w^2} \sim x\,\hat{x} + y\,\hat{y} \tag{6.10}$$

after Taylor expansion, where w is the beam waste. It can be seen from Eq. 6.10 that the trapping forces acting on the particle, when it is displaced small distances in x and y from equilibrium, are Hooke's law restoring forces, $F_{trapx}\,\hat{\boldsymbol{x}} = -k_x x\,\hat{\boldsymbol{x}}$ and $F_{trapy}\,\hat{\boldsymbol{y}} = -k_y y\,\hat{\boldsymbol{y}}$ respectively; where k_x and k_y are the strap stiffnesses in the x- and y-directions.

To support the validity of experimental results, we applied more than one data analysis technique to determine the trap strength. These included using the variance of the particle's motion in the trap (Fig. 6.5(a)) and the equipartition theorem, a Gaussian fit to a histogram of the distribution of the particle's fluctuations within the trap, and the corner frequency of the power spectrum of the particle's suppressed Brownian motion in the trap (Fig. 6.5(b)), as described in detail in Refs. [111, 131, 136]. For example, in Fig. 6.5(a) the variance of the particle's displacement, $\sigma^2 = (22.2\text{ nm})^2$, yielded the trap strength, $k_x = 8.3$ pN/μm, using the equipartition theorem,

$$\frac{1}{2}k_x\sigma^2 = \frac{1}{2}k_BT \qquad (6.11)$$

where k_B is the Boltzman constant and T is the temperature. The power spectrum of the position fluctuations (Fig. 6.5(b)) is given by [111],

$$\left|\tilde{x}(f)^2\right| = \frac{k_BT}{\pi^2\beta\left(f_c^2 + f^2\right)} \qquad (6.12),$$

where f is frequency, β is the drag coefficient of the particle in water, and f_c is the corner frequency, which is proportional to the trap stiffness, $f_c = k_x/(2\pi\beta)$. The data in Fig. 6.5(b) yielded a corner frequency of 136 Hz and a spring stiffness, k_x = 8.0 pN/μm. A criterion for a reliable determination of the trap strength was that the three data analysis methods yielded similar values of k_x (within 10 to 15%). Experimental controls, including measurements of sphere-to-sphere variation and sample-to-sample variation of the trap strength, using our experimental procedures were conducted, and an experimental uncertainty of approximately 15% was determined. The linear dependence of the trap stiffness on trapping laser power was also verified for both dye-doped and transparent spheres.

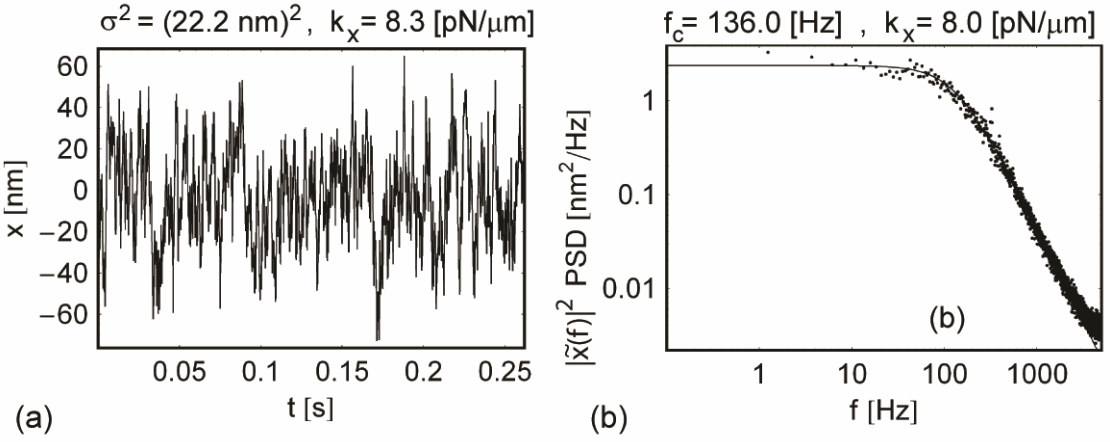

Figure 6.5: An example of the experimental data obtained from trap stiffness measurements. (a) Time series data of suppressed Brownian motion of a 1 μm dye-doped polystyrene sphere in the optical trap at the wavelength of 810 nm at 28 mW. The trap strength is obtained using the standard deviation of the data and equipartition theorem. (b) The power spectrum of the Brownian motion data in (a). The trap strength is obtained from the corner frequency, f_c, of the spectrum, which in this case is $f_c = 136.0$ Hz.

Trapping was done at a distance of approximately 16 μm from the cover slip inside the sample, to avoid hydrodynamic effects near the cover slip surface. Particles were typically trapped at laser powers between 8 and 48 mW, as measured after the dichroic mirror D2 and before the microscope objective (Fig. 6.4). To reduce experimental uncertainty, measurements at each wavelength were performed on 2-3 spheres, with multiple datasets taken for each trapped sphere. The trap strength measurements at each wavelength were then averaged. Under the same experimental conditions, measurements on 1 μm transparent polystyrene spheres were also taken at each wavelength. The data from the dye-doped spheres were then normalized using data from the transparent spheres. This was done to eliminate possible changes in the trapping force that may have resulted from slight variations of the incident laser beam

characteristics upon adjusting the wavelength, any wavelength dependence of the optics, etc.

6.3.2 Experimental Results

Figure 6.6 shows the transverse trap stiffness values, (k_x-dyed), measured for the '625 nm', '775 nm', and '840 nm' spheres, normalized by those obtained for the transparent spheres (k_x-transparent). An enhancement in the trap stiffness, as presented, is a value of k_x-dyed/k_x-transparent greater than 1. Measurements for the '625 nm' spheres were taken at wavelengths between 740 nm and 840 nm, which are on the red side of resonance. These results show that the '625 nm' spheres could be trapped stably (i.e. trapped indefinitely long in three dimensions) at all wavelengths, and no significant change in the trap strength was observed as a function of wavelength. For the '775 nm' spheres, measurements were taken at wavelengths between 755 nm (on the blue side of resonance) and 840 nm (on the red side of resonance). For these particles, stable trapping was also possible at all wavelengths, with no significant difference between trap stiffness values at wavelengths on either side of resonance. For the '840 nm' spheres we measured the trap strength on the red side of resonance at 980 nm, finding a small ~35% increase in the trap stiffness. However, the '840 nm' spheres could not be stably trapped at wavelengths between 750 - 840 nm, which are on the blue side of resonance. At these wavelengths they could be trapped momentarily (~10 s) before diffusing from the trap. When stable trapping was not observed the trap stiffness was considered to be $k_x = 0$ in Fig. 6.6. It can be seen from the data that there was little enhancement in the trap stiffness

observed experimentally for the ‘625 nm’, ‘775 nm’, and ‘840 nm’ spheres; with a ~35% increase in the trap stiffness for the ‘840 nm’ spheres observed at a wavelength of 980 nm, and a ~10% increase for both the ‘625 nm’ and ‘775 nm’ spheres (which is within our experimental uncertainty).

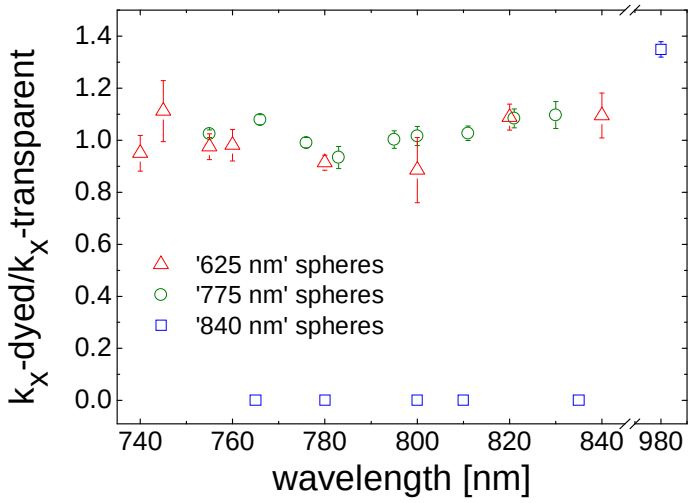

Figure 6.6: Experimental results for the measurements of the trap stiffness near resonance. The wavelength dependence of the trap stiffness values (*k*-dyed) is shown for ‘625 nm’, ‘775 nm’, and ‘840 nm’ dye-doped polystyrene spheres, all normalized by those measured on transparent spheres (*k*-transparent) under the same conditions. An enhancement in the trap stiffness is a value greater than one, and an unstable trap is a zero value.

6.3.3 Numerical Results and Discussion

To aid in the explanation of these experimental results and to obtain further insight, we modeled the optical properties of our dye-doped spheres and calculated the force acting on them in an optical tweezer trap. In particular, we calculated the trap stiffness of both dye-doped and transparent polystyrene spheres in an optical trap at multiple wavelengths near resonance using software developed by Nieminen et al. [121]. The program implements the T-Matrix formalism numerically, as described in

Section 6.2.1, to calculate the trapping force, from which the trap stiffness can be determined by using $\boldsymbol{F_{trap}}=F_{trap\,x}\,\hat{\boldsymbol{x}}+F_{trap\,y}\,\hat{\boldsymbol{y}}+F_{trap\,z}\,\hat{\boldsymbol{z}}=-k_x x\,\hat{\boldsymbol{x}}-k_y y\,\hat{\boldsymbol{y}}-k_z z\,\hat{\boldsymbol{z}}$. Numerical results for the trap stiffness and for the dimensionless trap efficiency, Q, in the x- and z-directions are presented in this section. The trap efficiency is related to the trapping force by $F_{trap\,i} = n_m P Q_i / c$, where P is the laser power.

To model the complex index of refraction of the dye-doped polystyrene spheres, we obtained values of the molar extinction coefficient (from the manufacturer) for the dye in the spheres as a function of wavelength. The imaginary part of the index of refraction, κ, was then determined using the molar extinction coefficient data, the molecular weight of the dye, the percentage dye loading of the sphere, the density of polystyrene, and by assuming that the dye was uniformly distributed in the sphere. The wavelength dependence of the extinction coefficient, κ, was then fit using the classic electron oscillator model of the complex dielectric constant [127]

$$\mathrm{Re}\left[\tilde{\varepsilon}(\omega)/\varepsilon_o\right] = \varepsilon_b + \sum_i f_i \frac{\omega_i^2 - \omega^2}{(\omega_i^2 - \omega^2)^2 + (\gamma_i \omega)^2} \tag{6.13}$$

$$\mathrm{Im}\left[\tilde{\varepsilon}(\omega)/\varepsilon_o\right] = \sum_i f_i \frac{\gamma_i \omega}{(\omega_i^2 - \omega^2)^2 + (\gamma_i \omega)^2} \tag{6.14}$$

and the relationship between the complex dielectric constant and the complex index of refraction,

$$\tilde{n}(\omega) = n(\omega) + i\kappa(\omega) = \sqrt{\tilde{\varepsilon}(\omega)/\varepsilon_o} \qquad (6.15)$$

where ε_b is the relative dielectric constant of the transparent polystyrene sphere (ε_b = 2.53), ω_i are resonant frequencies, γ_i are the damping coefficients, and f_i are scaling variables that are proportional to the molecular density and oscillator strength of the resonances. For the fit of κ (Fig. 6.7(a)) we assumed two resonance frequencies (i = 1, 2). The '775 nm' spheres have a peak value of κ_{peak} = 0.054. The refractive index, *n*, was then obtained using the fit parameters, f_i, γ_i, and Eqs. (6.13-6.15), as shown in Fig. 6.7(b). Similar analysis performed for the '840 nm' spheres, yielded a peak value of κ_{peak} = 0.108.

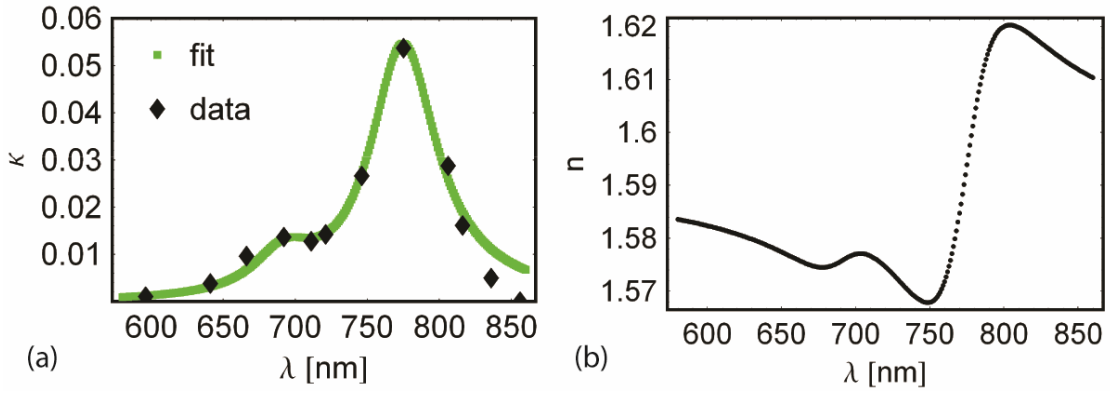

Figure 6.7: The wavelength dependence of the imaginary (a) and real (b) parts of the complex index of refraction, calculated by applying the classic electron oscillator model to the case of the '775 nm' spheres used in our experiments. (a) Values for the imaginary part of the index of refraction, κ, obtained from the manufacturer of the dye in the '775 nm' spheres (diamonds), fit using the classic electron oscillator model of the dielectric constant (line). (b) The corresponding refractive index values, n, calculated using the parameters extracted from the fit of the κ values in (a) and Eqs. 6.13 and 6.15.

To calculate the trap stiffness for the model of the '775 nm' dye-doped polystyrene spheres we first calculated the trap efficiency, Q, as a function of position in the trap. Example calculations of Q for the '775 nm' dye-doped sphere as a function of position, at two trap wavelengths are shown in Fig. 6.8. Simulations were performed using values from our experiments of $n_m = 1.33$ and NA = 1.25. Overfilling of the back aperture of the objective was not accounted for in the calculations (i.e. the Gaussian beam was not truncated). The geometry within the trap is shown in the inset of Fig. 6.8(a), with the origin of the coordinate system located at the focus of the trap. The trap efficiency, Q_z, (i.e. in the direction of laser propagation) as a function of position, z, is shown in Fig. 6.8(a), for wavelengths where both stable trapping occurs ($\lambda = 596$ nm) and stable trapping is not possible ($\lambda = 641$ nm). For stable trapping to occur the magnitude of the gradient force must be larger than the scattering and absorption forces. When this is the case, the particle will find a stable equilibrium point at a positive z position in the trap (z_{eq}) where the trapping force in the z-direction, and Q_z, are equal to zero. However, if the magnitude of the sum of the scattering and absorption forces is larger than the gradient force, then stable trapping in 3-D is not possible, and there will be no equilibrium point for the particle in the trap. The trap efficiency in the transverse direction, Q_x, as a function of position, x, is shown in Fig. 6.8(b) for the same wavelengths. The calculations of Q_x are performed for the particle at its equilibrium position z_{eq}. In the case where stable trapping is not possible, Q_x is zero, hence no data is shown for $\lambda = 641$ nm.

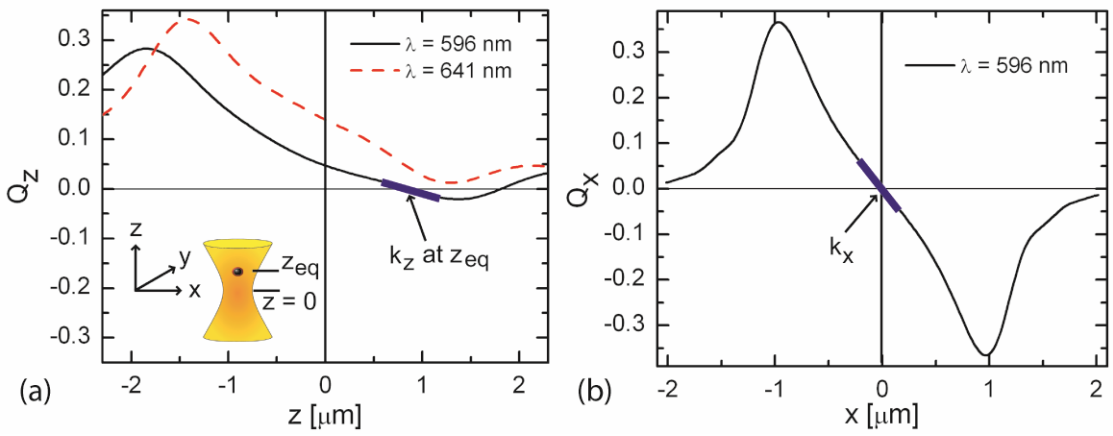

Figure 6.8: The numerically calculated trap efficiency Q in the (a) *z*-direction (Q_z) and (b) *x*-direction (Q_x) as a function of the position of the '775 nm' 1 μm sphere (κ_{peak} = 0.054) in the trap (*z* and *x*, respectively). The laser beam propagation is along *z*-axis, as indicated in the inset of (a). The trap stiffness k_z is determined from the slope of the Q_z (*z*) at $z = z_{eq}$, as illustrated in (a) for the case of λ = 596 nm. At λ = 641 nm, stable trapping is not possible (i.e. z_{eq} is not achieved), and therefore in (b) the Q_x data are shown only for λ = 596 nm. The trap stiffness k_x is calculated from the slope of $Q_x(x)$ at $x = 0$ (i.e. in the center of the beam).

The trap stiffness, *k*, was calculated from the slope of the trap efficiency near the equilibrium positions in *x* and *z*, (i.e. $x = 0$ and $z = z_{eq}$) as shown in Figs. 6.8(a) and 6.8(b). The calculated trap stiffness, k_x and k_z, for the '775 nm' spheres normalized to k_x and k_z, respectively, for transparent spheres, at multiple wavelengths near resonance is shown in Fig. 6.9. It can be seen from the data that it is not possible to trap stably ($k_x = k_z = 0$) near the resonance peak at wavelengths between 641nm and 806 nm. This behavior near the peak absorption agrees with the experimental results for the '840 nm' spheres (Fig. 6.6), but not for the '775 nm' or '625 nm' spheres. It can also be seen from Fig. 6.9, that at a wavelength of 836 nm (which is approximately 60 nm from the peak absorption) the simulations predict ~33% enhancement in k_x for the dyed-doped spheres relative to the transparent spheres. However, at this wavelength

the trap stiffness k_z is reduced so that the strength of the trap in 3-D is not enhanced. At a trap wavelength of 856 nm (~ 80 nm from the wavelength of peak absorption), there is less than a 10% enhancement in the normalized trap stiffness in the *x* and *z*-directions. Qualitatively, we expected the increase in the normalized trap stiffness at these wavelengths to be due in part to the increase in the refractive index off resonance (Fig. 6.7(b)). In our model, the increase in refractive index is from 1.59 for the transparent spheres to 1.6145 at 836 nm and 1.6109 at 856 nm for the dye-doped '775 nm' spheres. Interestingly, the simulations predict an enhancement in k_x of ~17 % on the blue side of resonance at a wavelength of 641 nm, as can be seen in Fig. 6.9. This is qualitatively unexpected given the reduction in the refractive index (1.5786) and the small amount of absorption (κ=0.0038) at this wavelength. Both of these would be expected to reduce the trap stiffness of the dye-doped spheres relative to the transparent spheres as is the case for k_z. It is possible, however, that Mie resonances in the electromagnetic fields [114, 128], which are dependent on the ratio of sphere diameter to wavelength of light, might account for this behavior. The results from the simulations of the '775 nm' 1μm polystyrene spheres, predict that the resonance of the dye does not provide a significant enhancement in the trap stiffness at wavelengths on the red side of resonance.

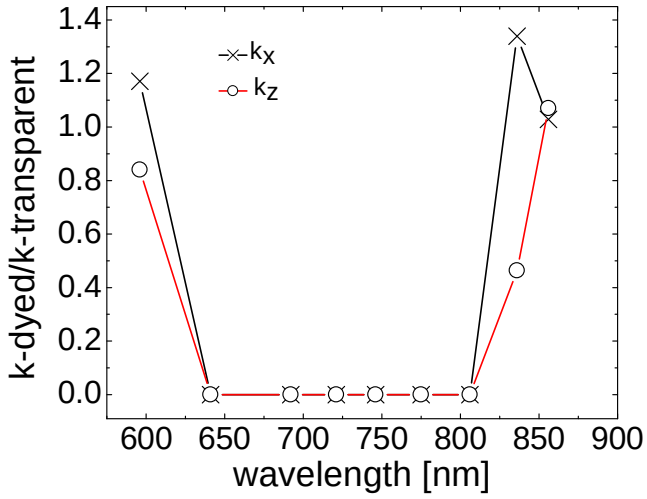

Figure 6.9: Numerically calculated wavelength dependence of the trap stiffness k_x and k_z in '775 nm' 1 μm spheres (*k*-dyed) with $\kappa_{peak} = 0.054$, normalized by the corresponding values calculated for 1 μm polystyrene transparent spheres (*k*-transparent). Stable trapping was not possible near resonance, which corresponds to zero values for k_x and k_z.

To gain insight as to why significant changes in the trap stiffness were not observed due to the resonance of the dye in the polystyrene, we performed simulations of the trap stiffness for nonabsorbing ('transparent') spheres with different refractive indices. The results of the simulations for k_x and k_z as a function of relative refractive index, *m*, at a trap wavelength of 780 nm are shown in Fig. 6.10. Simulations were conducted for 1μm ($d \sim \lambda$) and 20 nm ($d << \lambda$) spheres. It can be seen from the data that in both cases trap stiffness increases almost linearly for small values of *m*, but for the 1 μm spheres the existence of Mie scattering and resonances results in non-monotonic behavior for larger *m* [137]. In addition, for larger values of *m* (m>1.39) the scattering from the sphere increases, thus increasing the scattering force and preventing stable trapping (Fig. 6.10(a)) [123]. This behavior does not occur for smaller particles (Rayleigh particles), because scattering is much smaller (Fig.

6.10(b)). It can also be seen from Fig. 6.10(a) that an increase in the relative refractive index from m=1.59/1.33=1.20 (polystyrene in water) to m=1.62/1.33=1.22 (the maximum value of n from our model in Fig. 6.7(b)) results in an approximate increase in k_x of only ~20%. Thus the relative increase in the refractive index, n, resulting from the dye in the sphere is not substantial enough to provide a large increase in the trap stiffness.

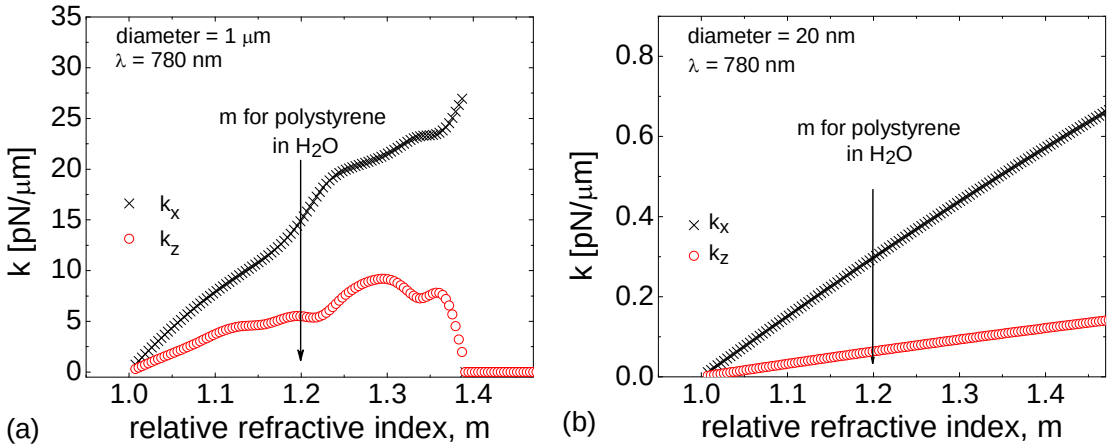

Figure 6.10: Numerically calculated dependence of the trap stiffness k_x and k_z, on the relative refractive index m for nonabsorbing spheres with a diameter of (a) 1 μm and (b) 20 nm, trapped at λ = 780 nm. At m > 1.39, stable trapping is not possible at this wavelength for 1 μm spheres (k_z = 0) in (a), but is possible for 20 nm spheres in (b). Structure seen in (a) is due to Mie resonances.

To explore the effect of a dye resonance in nanometer-sized polystyrene spheres, we used our model for the '775 nm' dye-doped spheres to explore the change in the trapping stiffness near resonance for smaller spheres. Figure 6.11(a) shows the trap stiffness, k_x, as a function of sphere diameter, at multiple trapping wavelengths. The numerical data shows that stable trapping can be achieved at all wavelengths near resonance for particles smaller than 60 nm in diameter. Figure 6.11(b) shows

normalized values of the trap stiffness, k_x, at wavelengths near resonance for particles 20 nm, 100 nm, 200 nm, 600 nm and 1 μm in diameter. It can be seen from these results that it is possible to trap smaller particles near resonance and that there is a smaller reduction in the trap stiffness, k_x, on resonance. Similar results were obtained for the trap stiffness, k_z (not shown). This is likely due to a decrease in the scattering and absorption cross sections as the particle becomes smaller. The results also show that the largest enhancement in the trap stiffness, k_x, occurred for the 1 μm diameter spheres (~35% at 836 nm). Reducing the sphere size did not produce additional enhancement in the trap stiffness.

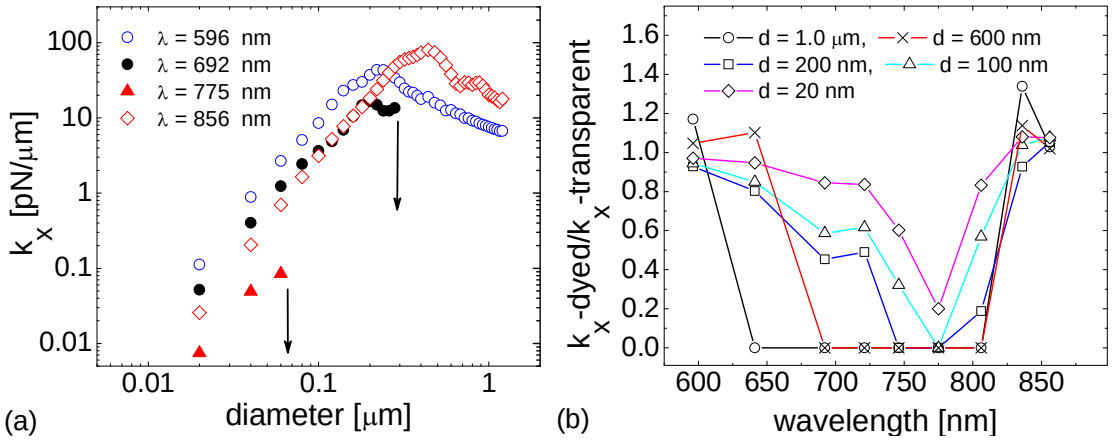

Figure 6.11: (a) Numerically calculated dependence of the trap stiffness k_x on the '775 nm' sphere diameter (all at κ_{peak} =0.054), at several wavelengths near the resonance. At small sphere sizes, the trap stiffness increases with the diameter (d) as $k_x \sim d^3$, as expected for Rayleigh particles. At λ = 775 nm (692 nm), stable trapping cannot be achieved for spheres larger than 60 nm (300 nm). (b) Numerically calculated wavelength dependence of the trap stiffness k_x in '775 nm' spheres (k_x-dyed) at κ_{peak} = 0.054, normalized by the corresponding values calculated for polystyrene transparent spheres (k_x-transparent), at various diameters of the sphere. At the diameter of 20 nm, stable trapping is possible at all wavelengths near the resonance, which is not the case for larger spheres. The largest enhancement of ~35% is achieved in 1 μm spheres at λ = 836 nm.

To further explore the effect of absorption from the dye on the trap stiffness, we changed the strength of absorption in our model of the 1 μm diameter '775 nm' dye-doped spheres by scaling the extinction coefficient values, κ. The values of κ in Fig. 6.7(a), were scaled to 150%, 25%, 10%, and 5% of the original values, resulting in peak values κ_{peak} of 0.081, 0.0135, 0.0054, and 0.0027 respectively. For each of κ_{peak} values above, the scaled extinction coefficient as a function of wavelength was fit using the classic electron oscillator model, and new refractive index values were obtained. Figure 6.12 shows the results for the normalized trap stiffness, k_x, for the scaled extinction values. It can be seen that when the values of κ are reduced to 10% of their original values ($\kappa_{peak} = 0.0054$) it is possible to trap at wavelengths on resonance, except for at the peak absorption ($\lambda = 775$ nm). In addition, the reduction in absorption results in a reduction in the increase in the relative trap stiffness seen on the blue side of resonance at $\lambda = 596$ nm, as compared to the increase at full absorption ($\kappa_{peak} = 0.054$). When further reducing the absorption to 5% it becomes possible to trap at all wavelengths near resonance, which agrees with experimental results for the '625 nm' and '775 nm' spheres. It can also be seen from Fig. 6.12 that when the absorption is further reduced the enhancement of the trap stiffness on the red side of resonance is also reduced and that the maximum enhancement of ~35% occurs at $\kappa_{peak} = 0.054$.

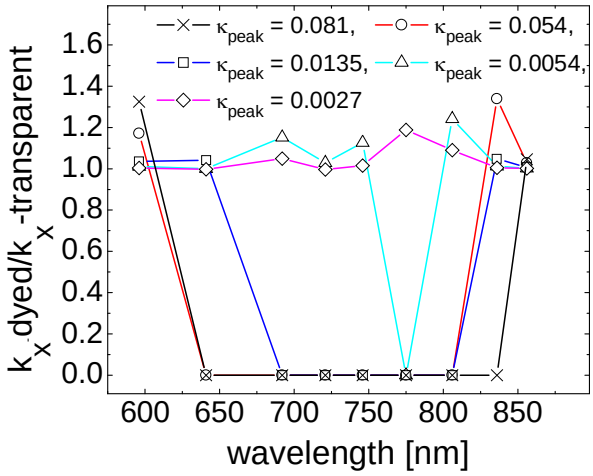

Figure 6.12: Numerically calculated wavelength dependence of the trap stiffness k_x of '775 nm' 1 μm spheres (k_x-dyed) for different peak values of the extinction coefficient (κ_{peak}), normalized by the corresponding values calculated for polystyrene transparent spheres (k_x-transparent). Stable trapping is not possible for the larger values of the extinction coefficient. The largest enhancement of ~35% on the red side of the resonance occurs for $\kappa_{peak} = 0.054$.

6.3.4 Conclusions from Wavelength Dependent Study

We explored, experimentally and numerically, the enhancement of the optical tweezer trapping force resulting from an optical resonance, using polystyrene spheres doped with dye as a model system. In both our experiments and numerical simulations we determined the trap stiffness at multiple trap wavelengths near the resonance. In our experimental and numerical results for dye-doped 1 μm spheres ($d \sim \lambda$), we did not find a substantial change or enhancement in the force at wavelengths near resonance when compared to polystyrene spheres without dye. Our numerical simulations also showed that a significant increase in the trap stiffness is not predicted for the dye-doped spheres if the size of the spheres is changed (20 nm < d < 1 μm) or if the strength of the absorption ($0.0027 < \kappa_{peak} < 0.081$) of the dye is changed. In

particular, the largest enhancement of the trap stiffness observed both experimentally and numerically was approximately 35%. The model could be further improved to include possible effects of nonuniform dye distribution in the sphere, which could be the cause of higher trap stiffness observed experimentally than that predicted theoretically for the same absorption strength near the resonance in '775 nm' spheres. Nevertheless, we conclude that the optical resonance of a dye-doped polystyrene sphere (ranging in size from 20 nm to 1 μm) does not provide a significant enhancement of the optical tweezer trapping force.

As a possible alternative to the absorption resonance provided by the dye in the polystyrene spheres, we explored, numerically, enhancements resulting from the absorption (plasmon) resonance of gold nanoparticles. Simulations for gold nanparticles were conducted using values for the refractive index, n, and the absorption coefficient, κ, of gold taken from Johnson and Christy [138]. The trap stiffness in the x- and z-direction was calculated as a function of wavelength, as with the dye-filled particles. Data for the numerical simulations on 40 nm and 80 nm gold spheres are shown in Fig. 6.13. Data are also shown for polystyrene spheres (n=1.59) as a function of wavelength to identify the wavelength dependence that occurs at a constant refractive index, which is due to changes in how the trapping light is focused at different wavelengths. In these simulations stable trapping was not possible at wavelengths close to resonance (i.e. $\lambda < 700$ nm). The increase in the trap stiffness, k_x, resulting from the plasmon resonance appears to be larger than that observed in the dye-filled spheres. For example on 40 nm spheres, the trap-stiffness at trapping

wavelengths on the red-side of resonance (peak absorption ~ 500nm) changes substantially for λ>704 nm. For larger particles it becomes more difficult to trap closer to resonance due to scattering and absorption from the gold particles in the trap (i.e. λ < 812 nm for 80 nm gold spheres). For larger particles (d > 130 nm) scattering and absorption make the trap unstable at all wavelengths simulated. The increase in the trap stiffness predicted for the 40nm gold spheres is promising and warrant the pursuit of conducting wavelength dependent experiments on gold nanoparticles.

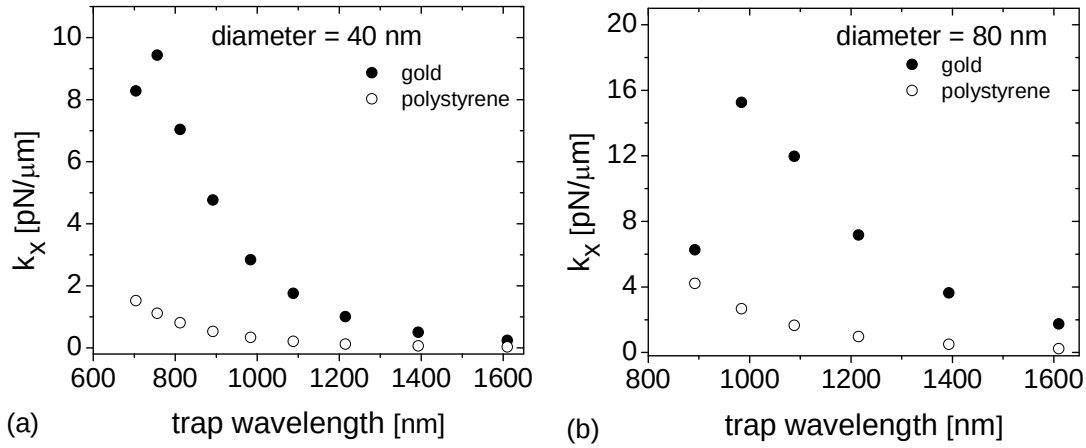

Figure 6.13: Numerical simulations of the trap stiffness in the *x*-direction, k_x, as function of wavelength on gold nanospheres. (a) Simulations for 40 nm gold particles and polystyrene particles (*n*=1.59). (b) Simulations for 80 nm gold and polystyrene particles. Data for transparent polystyrene spheres are included as a measure of the wavelength dependence that occurs at a constant refractive index.

6.4 pH/Ion Sensitive Nanoprobes with Optical Tweezers

6.4.1 Introduction

Optical tweezers are an important tool that can be used to control and manipulate particles [100]. For example, optical tweezers have been used in many biological applications [139, 140]. In addition, combining optical tweezers with

microfluidic devices in biological applications has recently been explored [141]. Also of recent interest is the development of intracellular measurement techniques, which has led to further understanding of cellular and molecular dynamics [142]. It is desirable to develop sensors that not only measure chemical properties of cells, but monitor chemical changes within cells as they respond to internal and external changes in their environment. In the preliminary work presented here, initial characterization of optically tweezer trapped fluorescence-based sensors, which can be used to detect changes in pH/ion-concentration, was conducted. An experimental setup was designed to simultaneously tweezer trap and measure photoluminescence (PL) from the sensors. The eventual end goal of this preliminary work is to (i) develop a measurement technique that incorporates optical tweezers, microfluidic devices, and fluorescence read-out of the pH/ion-sensors to monitor temporal and spatial changes in pH/ion-concentration within an environment; and (ii) develop the capability to use this technique as a method for intracellular monitoring of such changes as they occur within a cell, in a lab-on-a-chip platform.

6.4.2 pH/Ion-Sensitive Particles

For these experiments, our collaborator Dr. Alexey Shvarev developed polymeric fluorescent particles that are sensitive to pH and an ion of interest (e.g. sodium (Na^+), potassium (K^+), or calcium (Ca^+)). Details concerning the development of the ion selective particles (ion-optodes) can be found in Refs [143, 144]. The ion-optodes contain two types of fluorophores, ionophores and chromoionophores. The ionophores selectively bind to a primary ion of interest, and the chromoionophores

interact with the reference hydrogen ion (H^+). Multiple versions of the ion-optodes were developed, each having a different chromoionophore, resulting in a different fluorescence spectrum. However, each of the developed ion-optodes could be tailored to respond to an ion of interest, based on the ionophore used in the particle. An example of fluorescence (measured as PL, see *Section 3.2.3*) from a Na^+ sensitive ion-optode with chromoionophore1 is shown in Fig. 6.14. The spectra in Fig 6.14 display how the PL of the ion-optode changes from 'protonated' (peak PL ~680 nm) to 'deprotonated' (peak PL ~650 nm) when the concentration of Na^+ in the ion-optode's environment increases from a very low concentration to a higher concentration, respectively. As such, the ratio of the two PL peaks is used to determine the ion concentration of the environment. Each batch of sensors is calibrated by our collaborators, in solutions of known concentration upon being fabricated, as described in Refs [144, 145]. Once calibrated the sensors can be placed in an unknown solution to determine the concentration of a specific ion in the solution. Through the calibration procedure, the Na^+ ion-optodes exhibited a concentration detection limit of $5x10^{-4}$ M and a dynamic range of $5x10^{-4}$ to $1x10^{-1}$ M; K^+ and Ca^+ exhibited dynamic ranges of $1x10^{-4}$ to $1x10^{-1}$ M and $2x10^{-4}$ to $5x10^{-2}$ M, respectively. In addition, the pH/ion sensitive particles can be fabricated with an average size ranging from 200 nm to 30 μm, depending on fabrication conditions [144, 145]. When combined with optical tweezer trapping, these nano- to micro-sized particles can serve as high-spatial resolution probes in unknown environments.

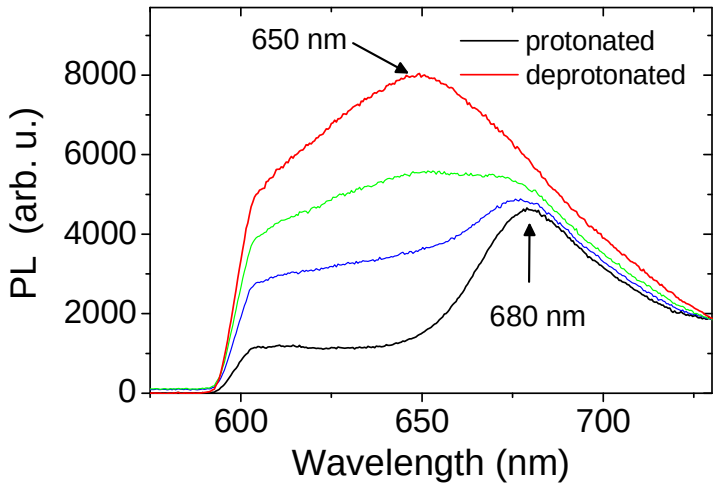

Figure 6.14: PL spectra from a Na^+ sensitive ion-optode in solution. Multiple spectra are shown from a single particle stuck to a coverslip, each at a different concentration of Na^+ in the solution.

6.4.3 Experimental Setup for Simultaneous Tweezer Trapping and PL detection

In this project, my work was focused on the development of an experimental setup and the initial characterization of tweezer trapped probes. Our experiments were conducted using an inverted microscope (Olympus, IX71), where we optically trapped and manipulated the nanosensors using optical tweezers at a wavelength in the near-infrared (Ti-Sapphire, λ~780nm) and excited PL at a wavelength of 532 nm. Both tweezer trapping and PL excitation/emission are conducted using a high NA objective (100X, 1.40 NA, Olympus UPlanSApo) (Fig. 6.15). Optical tweezer trapping light was aligned into the microscope's custom trapping port with external mirrors (M1 and M2) through a lens expansion pair. The light was then steered into the objective using a 725DCSP (Omega Optical) short pass dichroic mirror (DM1, Fig. 6.15) which reflects the trapping laser, but transmits both the PL excitation and emission. The PL

excitation was aligned into the microscope with a long pass dichroic mirror (either 560DCLP or 580 DRLP). In the experiments, either wide-field or confocal excitation was used depending on the strength of PL emission and the photostabilty of particles. The PL emission from the optodes was coupled back through the objective and the microscope confocal port into a 600 μm fiber (Ocean Optics, P600-2-600-UV-VIS), which delivered the emission to a spectrometer (USB2000, UV-VIS FLG). The spectrometer was calibrated to 3100K halogen lamp light that was collected through the emission path in the microscope described above. Alignment protocol were developed to co-align the trapping laser path, detection laser path, and the emission through the confocal port of the microscope. Samples, which consisted of ion-optode particles in solution, were imaged using a CCD camera (Coho, 4812) that was mounted on a special port on the microscope binoculars.

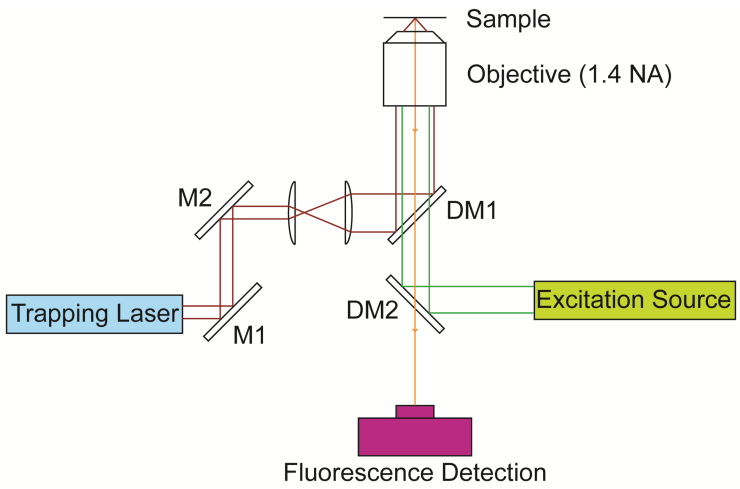

Figure 6.15: Experimental setup for simultaneous optical tweezer trapping and fluorescence measurements of pH/ion sensitive particles. The trapping laser (λ~780nm) was aligned into the microscope using mirrors (M1, M2) and a short pass dichroic mirror (DM1). The excitation source (λ~532 nm) was aligned into the microscope using a long pass dichroic mirror DM2.

6.4.4 Preliminary Results

Measurements attempted with optically trapped ion-optodes containing the chromoionphore1, as shown in Fig. 6.14 for a non-tweezer trapped particle, were unsuccessful, as they were susceptible to photodamage by the intense near-IR light used to trap. PL spectra obtained from ion-optodes with diameters of ~3-5 μm, containing the chromoionophore7, which have protonated and deprotonated PL peaks at ~670 nm and ~695 nm, respectively, are shown in Figs. 6.16 and 6.17. In these experiments, tweezer trapping was conducted at ~5mW, as measured before the dichroic mirror, DM1 (Fig 6.15) and with a confocal excitation power of ~11μW, as measured before DM2 (Fig. 6.15). The data in Fig. 6.16 shows PL spectra of optically tweezer trapped ion-optodes in an acidic solution (pH of ~2, blue line) and in a basic solution (pH~7.5, black line). The data show that the optodes have PL peaks at ~670 and 695 nm, but the peak at 695 nm is suppressed when the solution has a high pH. In the optodes with chromoionophore7, for solutions having intermediate pH values (data not shown), the PL peak at 670 nm would remain constant, and the amplitude of the PL peak at 695 nm would change with the pH. The data shown in Fig. 6.17 is from optically trapped Na^+ ion-optodes in solutions without salt (NaCl), and with a ~0.1 M concentration of NaCl, black and blue lines respectively.

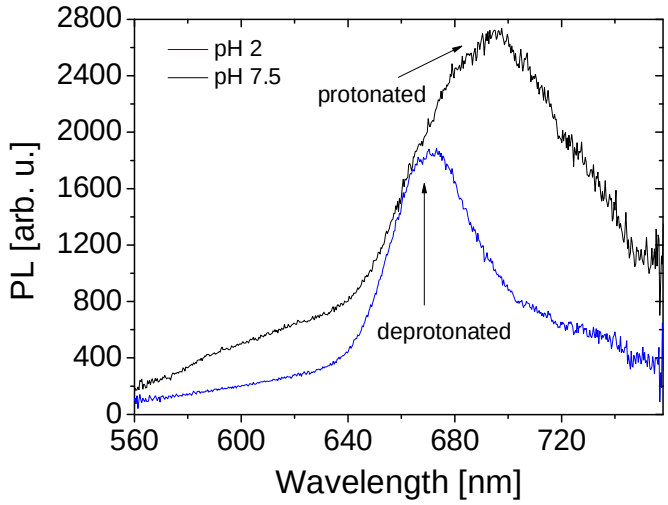

Figure 6.16: PL spectra from optically tweezer trapped ion-optodes in an acidic solution, pH~2, and a basic solution pH~7.5.

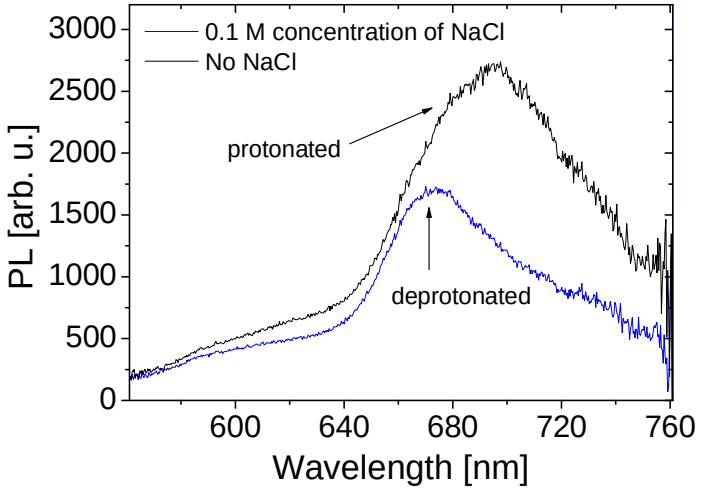

Figure 6.17: PL spectra from optically tweezer trapped ion-optodes in a solution without NaCl and with a 0.1 M concentration of NaCl.

6.4.5 Conclusions from ion-Optode Tweezer Trapping

The preliminary work on optical tweezer trapped ion-optodes was successful in developing an experimental setup to simultaneously trap and measure PL from the ion-optodes. This setup allowed for initial characterization of trapped pH/ion-optodes.

The characterization displayed the ability to tweezer trap ion-optodes and distinguish between environments with low and high pH, as well as environments with and without NaCl (with Na^+ ion-optodes). It was also successful in identifying the following experimental issues: (i) sensitivity limitations exist in the current PL measurement techniques, as signal to noise was extremely poor for particles smaller than ~3 μm; (ii) the polydispersity of ion-optode samples make it difficult to identify particles of a specific size, improvements in particle filter techniques could be needed; and (iii) the photostability, within the tweezer trap, of ion-optodes that contain the chromoionophore1 is limited. Work is currently underway by Dr. David McIntyre to remedy some of the experimental issues that were identified. For example, a new experimental setup is being developed that will allow multiple ion-optodes to be trapped, while simultaneously measuring the fluorescence from each of the trapped particles using wide-field excitation, an imaging spectrograph, and a highly sensitive CCD camera.

6.5 Surface Charge Measurements with Optical Tweezers

6.5.1 Introduction

Highly sensitive techniques for measuring the effective charge of particles in non-polar media, where the charge is typically very low, are desirable. In this section an optical tweezer based technique, developed by Roberts [146], is implemented and proof-of-principle effective charge measurements on polystyrene spheres in Milli-Q di-H_2O are presented. The effective charge is obtained experimentally, by measuring

the optical trapping forces acting on a particle under an applied alternating current (AC) electric-field (E-field) (Fig. 6.18). The method, as estimated by Roberts [146], is capable of accurately measuring a mean particle charge on the order of the unit charge of an electron (*e*).

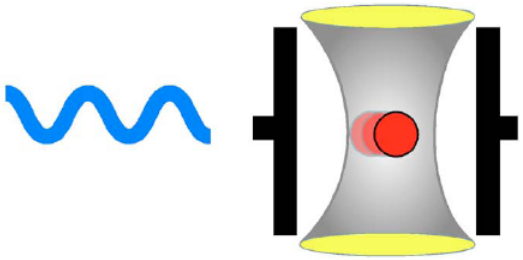

Figure 6.18: A cartoon depicting the optical tweezer based charge measurement technique, figure is taken from Ref [146]. The effective charge of a particle is obtained experimentally by applying an AC E-field to the particle within an optical tweezer trap and measuring the trapping force.

6.5.2 Charge Measurement Experiments

Samples were prepared as follows: (i) ~ 3mm wide strips of 150 μm thick aluminum tape were placed on a microscope slide, separated by ~ 300μm (estimated visually under a microscope using a micrometer driven stage); (ii) two adhesive Secure-seal spacers were stacked on top of each other over the electrodes and the microscope slide to create a sealed chamber; (iii) 1 μm polystyrene spheres (Duke Scientific) suspended in Milli-Q Di-H_2O were placed in the chamber; and (iv) a microscope cover-slip was placed over the adhesive spacer to close the chamber.

The experimental setup used to measure the optical tweezer trapping force acting on a particle within the trap is described above in *Section 6.3.1*. An AC voltage was applied to samples using a function generator (Tektronix, AFG3021).

The field was assumed to be approximately homogeneous in the region between the electrodes, where tweezer trapping was conducted [146], and was thus calculated as V/L, where L is the separation between the electrodes. Particles were trapped at a wavelength of λ~800 nm and power of ~20 mW, at a depth of ~20 μm from the cover slip. Particles were also trapped at a location roughly halfway between the two electrodes.

6.5.3 Preliminary Charge Measurement Results

Power spectrum measurements of the trap stiffness (as described in *Section. 6.3.1*) of an optically trapped polystyrene sphere with no applied E-field and with an AC E-field (100 Hz) of 6.67 kV/m and 13.33 kV/m are shown in Fig. 6.19. From the experimental data the effective charge of the particle was calculated as follows.

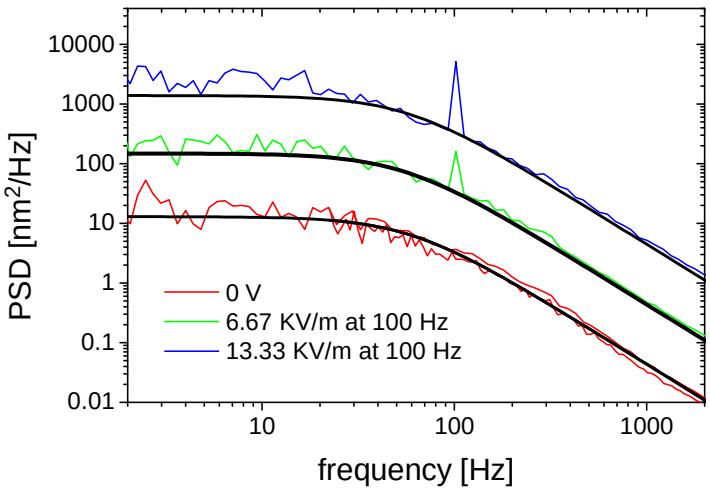

Figure 6.19: Power spectrum data obtained for surface charge measurements of a polystyrene sphere in an optical tweezer trap. Power spectra at multiple values of applied E-field, at an AC frequency of 100 Hz, are shown. Data at 6.67 kV/m and 13.33 kV/m are shifted up on the vertical axis for clarity.

The power spectral density of the particle's position within the trap (*PSD(f)*) can be expressed as a superposition of the contribution of the suppressed random Brownian motion in the trap (1st term in Eq. 6.16) and the contribution due to the sinusoidal driving force from the AC E-field (2nd term in Eq. 6.16). The PSD is expressed as

$$\frac{k_B T}{\pi^2 \beta\left[\left(k/2\pi\beta\right)^2 + f^2\right]} + \frac{k_B T \gamma^2}{k}\left(\delta(f - f_{AC})\right) = PSD(f) \qquad (6.16)$$

where k_B is the Boltzmann constant, β is the drag coefficient of the bead, k is the trap-stiffness, T is temperature, f_{AC} is the frequency of the AC E-field, and γ is a the ratio of the mean square sinusoidal and Brownian forces [146]. As such, the PSD is the typical Lorentzian spectrum of a particle in the trap (Fig. 6.5(b)) with a delta function at the frequency of the AC E-field, which has an amplitude that is E-field dependent. The contribution of the AC E-field to the PSD (P_{AC}) can then be determined by integrating

$$P_{AC} = \int_{-\infty}^{+\infty} \frac{k_B T \gamma^2}{k}\left(\delta(f - f_{AC})\right) = \frac{k_B T \gamma^2}{k} \qquad (6.17).$$

From the experimental data in Fig. 6.19, P_{AC} is determined at each value of applied E-field, by first fitting the PSD data to Eq. 6.12 to obtain the trap stiffness, *k*. The fit data is then subtracted from the experimental data to isolate the contribution of the AC E-field, and P_{AC} is calculated by integrating this contribution. Using the following relationship $\gamma^2 \sim E^2$ from Ref [146], P_{AC} is plotted as a function E^2 (Fig. 6.20)

and fit linearly. Values from the fit at applied E-fields are used to calculate the effective charge from Eq. 6.17 and

$$e\left|Z_{eff}\right| = \frac{\gamma\beta}{E}\sqrt{\frac{2k_BT}{k}\left(\left(2\pi f_{AC}\right)^2 + \left(k/\beta\right)^2\right)} \qquad (6.18),$$

where Z_{eff} is the effective charge in units of e, and β is the drag coefficient of the sphere [146]. A value of $Z_{eff} \sim 135$ was obtained from the data shown in Figs. 6.19 and 6.20. This value is an order of magnitude larger than that obtained for poly(methyl methacrylate) (PMMA) spheres with a diameter of ~1.2 μm in dodecane [146]. Future measurements of similar PMMA particles in dodecane would be needed to compare our experimental capabilities directly.

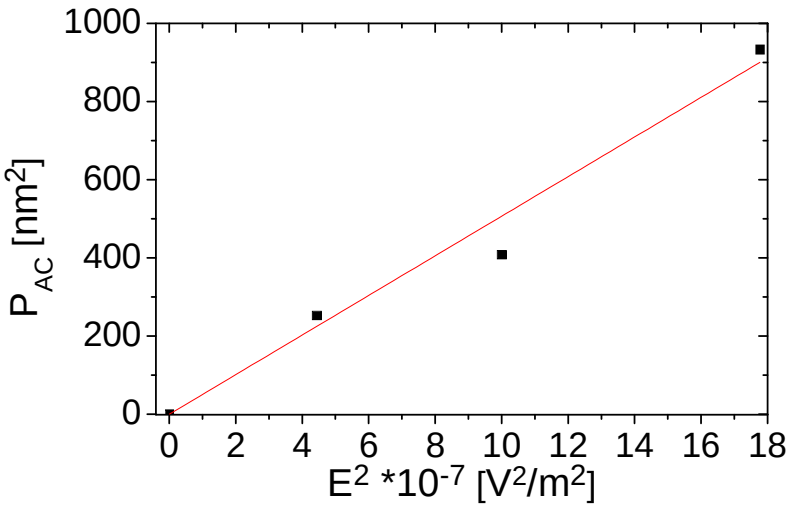

Figure 6.20: Values of P_{AC} as a function the E-field squared, obtained from experimental data. A linear fit to the data is also shown.

6.5.4 Summary of Preliminary Charge Measurements

The preliminary charge measurements, were successful in that we were able to detect the contribution from an applied AC E-field on a trapped polystyrene sphere, in data obtained using our experimental setup. However, to validate our measurements, further investigation into the experimental results for the effective charge on a 1 μm polystyrene sphere in di-H_2O is needed, as they differed substantially from those obtained for similar sized PMMA particles in dodecane. In addition, improvements in the technique used to attach electrodes to our sample substrates could be beneficial.

7 Conclusion

Light-matter interactions, which are fundamental to many research areas, were used to study the photophysics in organic semiconductors and explore the development of high-spatial resolution optical tweezer based probes. In the research related to organic semiconductor materials, a variety of novel materials and their composites were characterized, and physical mechanisms behind their optoelectronic properties were established. In the optical tweezer based research, the optical resonances of tweezer trapped particles were exploited in an attempt to increase the potential spatial resolution of optical tweezer-based probes.

Characterization of novel organic materials is crucial to the process of developing materials for specific applications and that have improved (opto)electronic properties. We conducted characterization of three novel hexacene derivatives (a non-fluorinated, a partially fluorinated, and a fluorinated derivative) functionalized with TCHS side groups. It was demonstrated that these derivatives are both sufficiently soluble and stable for studies in electronic devices. From our stability studies it was determined that fluorination of the hexacene backbone added to the stability of the material, such that fluorinated hexacenes could be factor of ~3 more stable than the non-fluorinated derivative in solution. In addition, the partially fluorinated hexacene derivative proved to be the most (photo)conductive in drop-cast films. A lower bound value of the mobility ($\sim 8.4 \times 10^{-3}$ cm^2/Vs) was obtained from space charge limited dark currents in partially fluorinated hexacene films on untreated

electrodes. Further optimization of both materials and processing conditions could be explored to determine if stability and material performance can be improved upon.

Organic semiconductor, donor/acceptor, composite films have been utilized in organic devices to enhance charge carrier photogeneration. An understanding of the charge transfer process in these composites, and how it relates to charge carrier photogeneration and transport is of importance for the development of better performing devices. We have investigated the charge transfer process in a variety of small-molecule organic, donor/acceptor, composite films. In ADT-TES-F/ADT-TIPS-CN (2%) and ADT-TES-F/C_{60} (2%) composite spun-cast films that have distinctly different charge transfer processes (e.g. charge transfer to a bound emissive exciton state and charge transfer to charge separated states, respectively) we determined a physical picture of exciton and charge carrier dynamics. Our findings in spun-cast films, from temperature and electric-field (E-field) dependent photoluminescence (PL) and transient photocurrent measurements, included the following: (i) dissociation of donor ADT-TES-F emissive excitons does not contribute to charge carrier photogeneration in composites; (ii) exciplex dissociation contributes to charge carrier photogeneration in ADT-TES-F/ADT-TIPS-CN composites; (iii) charge carrier photogeneration contributions from charge transfer to charge separated states in ADT-TES-F/C_{60} were ultra-fast, below the time resolution of our experiments; and (iv) charge transport in composites is dictated by the large percentage of the ADT-TES-F donor in the composite films, and, is characterized by a thermally activated hopping transport on time-scales up to ~5 ns that evolves into a non-activated tunneling

transport at longer time-scales. These measurements revealed that the dynamics of excited states at picosecond and sub-picosecond time-scales have a considerable contribution to the optical and electronic properties of ADT-TES-F-based composite films. Therefore, further studies using ultra-fast spectroscopy techniques, such as transient absorption, would be interesting and beneficial to determine the evolution of excitonic and charged transfer states on much shorter time-scales. This would allow for a refined physical picture of exciton and charge carrier dynamics in these materials.

In donor/acceptor (D/A) composite films, the dependence of charge transfer on the difference in LUMO energies of the donor and acceptor (ΔLUMO) and molecular packing at the D/A interface is of great interest. In our work, we determined that the type of charge transfer in a variety of drop-cast composite films, was dictated by ΔLUMO. Charge transfer to a bound emissive charge transfer state (exciplex) was observed for ΔLUMO <0.6 eV and charge transfer to a bound non-emissive charge transfer state (CT state) was observed for larger ΔLUMO values. However, the most dramatic effects observed in these composites were related to packing at the D/A interface; specifically, the separation between the donor and acceptor at the interface was the driving factor. In composites with large D/A separations, exciplex and CT state dissociation contributed to photocurrents at low values of applied E-field; no such contribution was observed in composites with small D/A separations. In addition, a dramatic reduction in charge carrier recombination, after initial photogeneration, was observed in composite films with large D/A separation, as

compared to pristine ADT-TES-F films and composite films with small D/A separation. The reduced recombination contributed to a factor of ~5-10 increase in continuous wave photocurrents in composites with large D/A separations. We demonstrated through this work that both charge transfer exciton dissociation and charge recombination can be effectively manipulated by adjusting the molecular interaction between the donor and acceptor by changing the size of the substituent on the acceptor. Given the importance of the molecular packing at the D/A interface, additional studies looking closely at the film morphology and molecular packing in composite films to try to identify physical differences between D/A interfaces in different composite films, and how they affect exciton and charge carrier dynamics could be rather revealing. For example, using high resolution PL imaging methods coupled with the development of new experimental techniques that allow for E-field-assisted PL quenching and transient photocurrent measurements within small regions of a film could be used as a method to relate physical structure within a film to excitonic and charge carrier dynamics. This could make it possible to identify differences in molecular packing in the donor phase of the film as compared to D/A interfaces, or between D/A interfaces in different types of composite films.

In optical tweezer controlled probes, high spatial resolution is of importance. However, the natural Brownian motion of a particle within the optical tweezer trap reduces the resolution of such a probe. This Brownian motion can be better suppressed with stronger trapping forces acting on a particle in the trap. As a method to increase the trapping forces on a particle, we explored, experimentally and

numerically, the enhancement of the optical tweezer trapping force (trap stiffness) resulting from an optical resonance, using polystyrene spheres doped with dye. In our experimental and numerical results for dye-doped 1 μm spheres ($d \sim\lambda$), a small increase in the trap-stiffness was observed when tweezer trapping at wavelengths on the red-side of resonance. Our numerical simulations also showed that only a small increase in the trap stiffness is predicted for the dye-doped spheres if the size of the spheres is changed (20 nm < d < 1 μm) or if the strength of the absorption ($0.0027 < \kappa_{peak} < 0.081$) of the dye is changed. In particular, the largest enhancement of the trap stiffness both experimentally and numerically was approximately 35%. From our models, we also identified limitations in using resonant enhancement for micron sized particles, due to large scattering from particles on this size scale. We also believe that there is a limitation in the optical absorption resonance of the dye in the spheres that resulted in a small increase in the real part of the index of refraction Re(n); where more dramatic increases in Re(n) are needed to obtain larger increases in the trap stiffness. Therefore, resonant enhancement of the tweezer trapping force may be worth pursuing in other resonant particles that have a different optical absorption resonance. For example, based on our numerical simulations on gold nanospheres, metallic nanoparticles could be promising candidates.

References

1. K. Visscher, M. J. Schnitzer, and S. M. Block, "Single kinesin molecules studied with a molecular force clamp," Nature **400**, 184-189 (1999).

2. R. Farchioni and G. Grosso, eds., *Organic Electronic Materials Conjugated Polymers and Low Molecular Weight Organic Solids* (Springer, New York, 2000).

3. E. A. Silinish and V. Capek, *Organic Molecular Crystals: Interaction, Localization, and Transport Phenomena* (American Institute of Physics, New York, 1994).

4. Y. Yang and F. Wudl, "Organic Electronics: From Materials to Devices," Advanced Materials **21**, 1401-1403 (2009).

5. P. Peumans, A. Yakimov, and S. R. Forrest, "Small molecular weight organic thin-film photodetectors and solar cells," Journal of Applied Physics **93**, 3693-3723 (2003).

6. D. Braga and G. Horowitz, "High-Performance Organic Field-Effect Transistors," Advanced Materials **21**, 1473-1486 (2009).

7. O. Ostroverkhova and W. E. Moerner, "Organic photorefractives: Mechanisms, materials, and applications," Chemical Reviews **104**, 3267-3314 (2004).

8. S. R. Forrest, "The path to ubiquitous and low-cost organic electronic appliances on plastic," Nature **428**, 911-918 (2004).

9. C. D. Dimitrakopoulos and P. R. L. Malenfant, "Organic thin film transistors for large area electronics," Advanced Materials **14**, 99-117 (2002).

10. V. Coropceanu, J. Cornil, D. A. da Silva, Y. Olivier, R. Silbey, and J. L. Bredas, "Charge transport in organic semiconductors," Chemical Reviews **107**, 926-952 (2007).

11. E. A. Silinsh, G. A. Shlihta, and A. J. Jurgis, "A model description of charge carrier transport phenomena in organic molecular-crystals .2.-perlylene," Chemical Physics **155**, 389-399 (1991).

12. F. A. Hegmann, "Ultrafast carrier dynamics in conjugated polymers and organic molecular crystals," Physics In Canada **59**, 127-140 (2003).

13. J. E. Anthony, D. L. Eaton, and S. R. Parkin, "A road map to stable, soluble, easily crystallized pentacene derivatives," Organic Letters **4**, 15-18 (2002).

14. J. Cornil, J. P. Calbert, and J. L. Bredas, "Electronic structure of the pentacene single crystal: Relation to transport properties," J. Am. Chem. Soc. **123**, 1250-1251 (2001).

15. O. D. Jurchescu, D. A. Mourey, S. Subramanian, S. R. Parkin, B. M. Vogel, J. E. Anthony, T. N. Jackson, and D. J. Gundlach, "Effects of polymorphism on charge transport in organic semiconductors," Physical Review B **80**, 085201 (2009).

16. J. E. Anthony, "Functionalized acenes and heteroacenes for organic electronics," Chemical Reviews **106**, 5028-5048 (2006).

17. J. E. Anthony, J. S. Brooks, D. L. Eaton, and S. R. Parkin, "Functionalized pentacene: Improved electronic properties from control of solid-state order," J. Am. Chem. Soc. **123**, 9482-9483 (2001).

18. S. K. Park, T. N. Jackson, J. E. Anthony, and D. A. Mourey, "High mobility solution processed 6,13-bis(triisopropyl-silylethynyl) pentacene organic thin film transistors," Applied Physics Letters **91**, 063514 (2007).

19. J. E. Anthony, "The larger acenes: Versatile organic semiconductors," Angewandte Chemie-International Edition **47**, 452-483 (2008).

20. D. J. Gundlach, J. E. Royer, S. K. Park, S. Subramanian, O. D. Jurchescu, B. H. Hamadani, A. J. Moad, R. J. Kline, L. C. Teague, O. Kirillov, C. A. Richter, J. G. Kushmerick, L. J. Richter, S. R. Parkin, T. N. Jackson, and J. E. Anthony, "Contact-induced crystallinity for high-performance soluble acene-based transistors and circuits," Nature Materials **7**, 216-221 (2008).

21. S. K. Park, D. A. Mourey, S. Subramanian, J. E. Anthony, and T. N. Jackson, "High-mobility spin-cast organic thin film transistors," Applied Physics Letters **93**, 043301 (2008).

22. R. J. Kline, S. D. Hudson, X. R. Zhang, D. J. Gundlach, A. J. Moad, O. D. Jurchescu, T. N. Jackson, S. Subramanian, J. E. Anthony, M. F. Toney, and L. J. Richter, "Controlling the Microstructure of Solution-Processable Small Molecules in Thin-Film Transistors through Substrate Chemistry," Chemistry of Materials **23**, 1194-1203 (2011).

23. O. Ostroverkhova, D. G. Cooke, F. A. Hegmann, J. E. Anthony, V. Podzorov, M. E. Gershenson, O. D. Jurchescu, and T. T. M. Palstra, "Ultrafast carrier

dynamics in pentacene, functionalized pentacene, tetracene, and rubrene single crystals," Applied Physics Letters **88**, 162101 (2006).

24. H. Bassler and B. Schweitzer, "Site-selective fluorescence spectroscopy of conjugated polymers and oligomers," Accounts of Chemical Research **32**, 173-182 (1999).

25. P. Coppo and S. G. Yeates, "Shining light on a pentacene derivative: The role of photoinduced cycloadditions," Advanced Materials **17**, 3001-+ (2005).

26. W. Brutting, *Physics of Organic Semiconductors* (Wiley-VCH, Germany, 2005).

27. M. Pope and C. E. Swenberg, *Electronic Processes in Organic Crystals and Polymers* (Oxford University Press, New York, 1998).

28. T. Holstein, "Studies of polaron motion: Part II. The "small" polaron," Ann. Phys. **8**, 325-342 (1959).

29. W. Warta and N. Karl, "Hot holes in naphthalene - High electric-field-dependent mobilities," Physical Review B **32**, 1172-1182 (1985).

30. V. K. Thorsmolle, R. D. Averitt, X. Chi, D. J. Hilton, D. L. Smith, A. P. Ramirez, and A. J. Taylor, "Ultrafast conductivity dynamics in pentacene probed using terahertz spectroscopy," Applied Physics Letters **84**, 891-893 (2004).

31. O. D. Jurchescu, J. Baas, and T. T. M. Palstra, "Effect of impurities on the mobility of single crystal pentacene," Applied Physics Letters **84**, 3061-3063 (2004).

32. D. Moses, C. Soci, X. L. Chi, and A. P. Ramirez, "Mechanism of carrier photogeneration and carrier transport in molecular crystal tetracene," Physical Review Letters **97**, 067401 (2006).

33. O. Ostroverkhova, *Optical and electrical properties of organic semiconductor*, Encyclopedia of Nanoscience and Nanotechnology (American Scientific Publishers, CA, 2011), Vol. 20.

34. J. Day, S. Subramanian, J. E. Anthony, Z. Lu, R. J. Twieg, and O. Ostroverkhova, "Photoconductivity in organic thin films: From picoseconds to seconds after excitation," Journal of Applied Physics **103**, 123715 (2008).

35. A. D. Platt, M. J. Kendrick, M. Loth, J. E. Anthony, and O. Ostroverkhova, "Temperature dependence of exciton and charge carrier dynamics in organic thin films," Physical Review B **84**, 235209 (2011).

36. O. Ostroverkhova, D. G. Cooke, S. Shcherbyna, R. F. Egerton, F. A. Hegmann, R. R. Tykwinski, and J. E. Anthony, "Bandlike transport in pentacene and functionalized pentacene thin films revealed by subpicosecond transient photoconductivity measurements," Physical Review B **71**, 035204 (2005).

37. J. Day, A. D. Platt, S. Subramanian, J. E. Anthony, and O. Ostroverkhova, "Influence of organic semiconductor-metal interfaces on the photoresponse of functionalized anthradithiophene thin films," Journal of Applied Physics **105**, 103703 (2009).

38. A. D. Platt, J. Day, S. Subramanian, J. E. Anthony, and O. Ostroverkhova, "Optical, Fluorescent, and (Photo)conductive Properties of High-Performance Functionalized Pentacene and Anthradithiophene Derivatives," Journal of Physical Chemistry C **113**, 14006-14014 (2009).

39. J. Day, A. D. Platt, O. Ostroverkhova, S. Subramanian, and J. E. Anthony, "Organic semiconductor composites: Influence of additives on the transient photocurrent," Applied Physics Letters **94**, 013306 (2009).

40. W. E. B. Shepherd, A. D. Platt, M. J. Kendrick, M. A. Loth, J. E. Anthony, and O. Ostroverkhova, "Energy Transfer and Exciplex Formation and Their Impact on Exciton and Charge Carrier Dynamics in Organic Films," Journal of Physical Chemistry Letters **2**, 362-366 (2011).

41. W. E. B. Shepherd, A. D. Platt, D. Hofer, O. Ostroverkhova, M. Loth, and J. E. Anthony, "Aggregate formation and its effect on (opto)electronic properties of guest-host organic semiconductors," Applied Physics Letters **97**, 163303 (2010).

42. W. E. B. Shepherd, Platt A.D., Banton G., Loth A., Anthony J.E., and Ostroverkhova O., "Optical, photoluminescent, and photoconductive properties of functionized anthradithiophene and benzothiophene derivatives," in *proceedings of SPIE,* (2010), p. 75990R.

43. M. M. Payne, S. A. Odom, S. R. Parkin, and J. E. Anthony, "Stable, crystalline acenedithiophenes with up to seven linearly fused rings," Organic Letters **6**, 3325-3328 (2004).

44. R. Mondal, B. K. Shah, and D. C. Neckers, "Photogeneration of heptacene in a polymer matrix," J. Am. Chem. Soc. **128**, 9612-9613 (2006).

45. W. Q. Deng and W. A. Goddard, "Predictions of hole mobilities in oligoacene organic semiconductors from quantum mechanical calculations," Journal of Physical Chemistry B **108**, 8614-8621 (2004).

46. R. Mondal, R. M. Adhikari, B. K. Shah, and D. C. Neckers, "Revisiting the stability of hexacenes," Organic Letters **9**, 2505-2508 (2007).

47. M. M. Payne, S. R. Parkin, and J. E. Anthony, "Functionalized higher acenes: Hexacene and heptacene," J. Am. Chem. Soc. **127**, 8028-8029 (2005).

48. D. Chun, Y. Cheng, and F. Wudl, "The Most Stable and Fully Characterized Functionalized Heptacene," Angewandte Chemie-International Edition **47**, 8380-8385 (2008).

49. S. S. Zade and M. Bendikov, "Heptacene and Beyond: The Longest Characterized Acenes," Angewandte Chemie-International Edition **49**, 4012-4015 (2010).

50. B. Purushothaman, S. R. Parkin, and J. E. Anthony, "Synthesis and Stability of Soluble Hexacenes," Organic Letters **12**, 2060-2063 (2010).

51. I. Kaur, N. N. Stein, R. P. Kopreski, and G. P. Miller, "Exploiting Substituent Effects for the Synthesis of a Photooxidatively Resistant Heptacene Derivative," J. Am. Chem. Soc. **131**, 3424-3425 (2009).

52. S. Subramanian, S. K. Park, S. R. Parkin, V. Podzorov, T. N. Jackson, and J. E. Anthony, "Chromophore fluorination enhances crystallization and stability of soluble anthradithiophene semiconductors," J. Am. Chem. Soc. **130**, 2706-2707 (2008).

53. M. A. Lampert and P. Mark, *Current injection in solids* (Academic Press Inc, , New York, 1970).

54. W. P. Hu, B. Gompf, J. Pflaum, D. Schweitzer, and M. Dressel, "Transport properties of [2,2]-paracyclophane thin films," Applied Physics Letters **84**, 4720-4722 (2004).

55. T. M. Clarke and J. R. Durrant, "Charge Photogeneration in Organic Solar Cells," Chemical Reviews **110**, 6736-6767 (2010).

56. J. H. Chen, C. K. Tee, J. Y. Yang, C. Shaw, M. Shtein, J. Anthony, and D. C. Martin, "Thermal and mechanical cracking in bis(triisopropylsilyiethnyl) pentacene thin films," Journal of Polymer Science Part B-Polymer Physics **44**, 3631-3641 (2006).

57. C. W. Sele, B. K. C. Kjellander, B. Niesen, M. J. Thornton, J. van der Putten, K. Myny, H. J. Wondergem, A. Moser, R. Resel, A. van Breemen, N. van Aerle, P. Heremans, J. E. Anthony, and G. H. Gelinck, "Controlled Deposition of Highly Ordered Soluble Acene Thin Films: Effect of Morphology and Crystal Orientation on Transistor Performance," Advanced Materials **21**, 4926-4931 (2009).

58. H. E. Katz and J. Huang, "Thin-Film Organic Electronic Devices," Annual Review of Materials Research **39**, 71-92 (2009).

59. A. C. Arias, J. D. MacKenzie, I. McCulloch, J. Rivnay, and A. Salleo, "Materials and Applications for Large Area Electronics: Solution-Based Approaches," Chemical Reviews **110**, 3-24 (2010).

60. Z. Li, Y. F. Lim, J. B. Kim, S. R. Parkin, Y. L. Loo, G. G. Malliaras, and J. E. Anthony, "Isomerically pure electron-deficient anthradithiophenes and their acceptor performance in polymer solar cells," Chemical Communications **47**, 7617-7619 (2011).

61. M. T. Lloyd, A. C. Mayer, S. Subramanian, D. A. Mourey, D. J. Herman, A. V. Bapat, J. E. Anthony, and G. G. Malliaras, "Efficient solution-processed photovoltaic cells based on an anthradithiophene/fullerene blend," J. Am. Chem. Soc. **129**, 9144-9149 (2007).

62. T. Offermans, P. A. van Hal, S. C. J. Meskers, M. M. Koetse, and R. A. J. Janssen, "Exciplex dynamics in a blend of pi-conjugated polymers with electron donating and accepting properties: MDMO-PPV and PCNEPV," Physical Review B **72**, 045213 (2005).

63. D. Veldman, O. Ipek, S. C. J. Meskers, J. Sweelssen, M. M. Koetse, S. C. Veenstra, J. M. Kroon, S. S. van Bavel, J. Loos, and R. A. J. Janssen, "Compositional and electric field dependence of the dissociation of charge transfer excitons in alternating polyfluorene copolymer/fullerene blends," J. Am. Chem. Soc. **130**, 7721-7735 (2008).

64. A. J. Heeger, "Semiconducting polymers: the Third Generation," Chemical Society Reviews **39**, 2354-2371 (2010).

65. Y. Kim, M. Ballarotto, D. Park, M. Du, W. Cao, C. H. Lee, W. N. Herman, and D. B. Romero, "Interface effects on the external quantum efficiency of organic bulk heterojunction photodetectors," Applied Physics Letters **91**, 193510 (2007).

66. M. T. Lloyd, Y. F. Lim, and G. G. Malliaras, "Two-step exciton dissociation in poly(3-hexylthiophene)/fullerene heterojunctions," Applied Physics Letters **92**, 143308 (2008).

67. H. Kleemann, C. Schuenemann, A. A. Zakhidov, M. Riede, B. Lussem, and K. Leo, "Structural phase transition in pentacene caused by molecular doping and its effect on charge carrier mobility," Organic Electronics **13**, 58-65 (2012).

68. Y. F. Lim, Y. Shu, S. R. Parkin, J. E. Anthony, and G. G. Malliaras, "Soluble n-type pentacene derivatives as novel acceptors for organic solar cells," Journal of Materials Chemistry **19**, 3049-3056 (2009).

69. F. C. Spano, J. Clark, C. Silva, and R. H. Friend, "Determining exciton coherence from the photoluminescence spectral line shape in poly(3-hexylthiophene) thin films," J. Chem. Phys. **130**, 074904 (2009).

70. C. H. Lee, G. Yu, D. Moses, K. Pakbaz, C. Zhang, N. S. Sariciftci, A. J. Heeger, and F. Wudl, "Sensitization of the photoconductivity of conducting polymers by C-60: Photoinduced electron-transfer," Physical Review B **48**, 15425-15433 (1993).

71. Y. C. Luo, H. Aziz, R. Klenkler, G. Xu, and Z. D. Popovic, "Temperature dependence of photoluminescence efficiency in doped and blended organic thin films," Chemical Physics Letters **458**, 319-322 (2008).

72. A. Y. Kobitski, R. Scholz, D. R. T. Zahn, and H. P. Wagner, "Time-resolved photoluminescence study of excitons in alpha-PTCDA as a function of temperature," Physical Review B **68**(2003).

73. G. Gigli, F. Della Sala, M. Lomascolo, M. Anni, G. Barbarella, A. Di Carlo, P. Lugli, and R. Cingolani, "Photoluminescence efficiency of substituted quaterthiophene crystals," Physical Review Letters **86**, 167-170 (2001).

74. Z. D. Popovic, M. I. Khan, A. M. Hor, J. L. Goodman, and J. F. Graham, "Study of carrier generation in phthalocyanines by time-resolved fluorescence," Journal of Physical Chemistry B **106**, 8625-8631 (2002).

75. Z. D. Popovic, M. I. Khan, S. J. Atherton, A. M. Hor, and J. L. Goodman, "Study of carrier generation in titanyl phthalocyanine (TiOPc) by electric-field-induced quenching of integrated and time-resolved fluorescence," Journal of Physical Chemistry B **102**, 657-663 (1998).

76. H. Najafov, I. Biaggio, T. K. Chuang, and M. K. Hatalis, "Exciton dissociation by a static electric field followed by nanoscale charge transport in PPV polymer films," Physical Review B **73**(2006).

77. H. Scher, M. F. Shlesinger, and J. T. Bendler, "Time-scale invariance in transport and relaxation," Physics Today **44**, 26-34 (1991).

78. O. D. Jurchescu, S. Subramanian, R. J. Kline, S. D. Hudson, J. E. Anthony, T. N. Jackson, and D. J. Gundlach, "Organic Single-Crystal Field-Effect Transistors of a Soluble Anthradithiophene," Chemistry of Materials **20**, 6733-6737 (2008).

79. O. Ostroverkhova, S. Shcherbyna, D. G. Cooke, R. F. Egerton, F. A. Hegmann, R. R. Tykwinski, S. R. Parkin, and J. E. Anthony, "Optical and transient photoconductive properties of pentacene and functionalized pentacene thin films: Dependence on film morphology," Journal of Applied Physics **98**(2005).

80. P. B. Miranda, D. Moses, and A. J. Heeger, "Ultrafast photogeneration of charged polarons in conjugated polymers," Physical Review B **64**, 081202 (2001).

81. V. I. Arkhipov, E. V. Emelianova, and H. Bassler, "Hot exciton dissociation in a conjugated polymer," Physical Review Letters **82**, 1321-1324 (1999).

82. C. Deibel and V. Dyakonov, "Polymer-fullerene bulk heterojunction solar cells," Reports on Progress in Physics **73**(2010).

83. B. Walker, C. Kim, and T. Q. Nguyen, "Small Molecule Solution-Processed Bulk Heterojunction Solar Cells," Chemistry of Materials **23**, 470-482 (2011).

84. J. E. Anthony, "Small-Molecule, Nonfullerene Acceptors for Polymer Bulk Heterojunction Organic Photovoltaics," Chemistry of Materials **23**, 583-590 (2011).

85. J. Roncali, "Molecular Bulk Heterojunctions: An Emerging Approach to Organic Solar Cells," Accounts of Chemical Research **42**, 1719-1730 (2009).

86. M. T. Lloyd, J. E. Anthony, and G. G. Malliaras, "Photovoltaics from soluble small molecules," Materials Today **10**, 34-41 (2007).

87. Y. Shu, Y. F. Lim, Z. Li, B. Purushothaman, R. Hallani, J. E. Kim, S. R. Parkin, G. G. Malliaras, and J. E. Anthony, "A survey of electron-deficient pentacenes as acceptors in polymer bulk heterojunction solar cells," Chemical Science **2**, 363-368 (2011).

88. S. Shoaee, M. P. Eng, E. Espildora, J. L. Delgado, B. Campo, N. Martin, D. Vanderzande, and J. R. Durrant, "Influence of nanoscale phase separation on

geminate versus bimolecular recombination in P3HT:fullerene blend films," Energy & Environmental Science **3**, 971-976 (2010).

89. C. Deibel, T. Strobel, and V. Dyakonov, "Role of the Charge Transfer State in Organic Donor-Acceptor Solar Cells," Advanced Materials **22**, 4097-4111 (2010).

90. J. L. Bredas, J. E. Norton, J. Cornil, and V. Coropceanu, "Molecular Understanding of Organic Solar Cells: The Challenges," Accounts of Chemical Research **42**, 1691-1699 (2009).

91. X. Y. Zhu, Q. Yang, and M. Muntwiler, "Charge-Transfer Excitons at Organic Semiconductor Surfaces and Interfaces," Accounts of Chemical Research **42**, 1779-1787 (2009).

92. C. R. Swartz, S. R. Parkin, J. E. Bullock, J. E. Anthony, A. C. Mayer, and G. G. Malliaras, "Synthesis and characterization of electron-deficient pentacenes," Organic Letters **7**, 3163-3166 (2005).

93. B. Purushothaman, M. J. Kendrick, D. David, J. W. Ward, L. Yee-Fun, G. G. Malliaras, O. D. Jurchescu, O. Ostroverkhova, and J. E. Anthony, "Synthesis and device studies of stable hexacene derivatives," (in progress).

94. D. T. Chase, A. G. Fix, B. D. Rose, C. D. Weber, S. Nobusue, C. E. Stockwell, L. N. Zakharov, M. C. Lonergan, and M. M. Haley, "Electron-Accepting 6,12-Diethynylindeno[1,2-b]fluorenes: Synthesis, Crystal Structures, and Photophysical Properties," Angewandte Chemie-International Edition **50**, 11103-11106 (2011).

95. M. T. Rispens, A. Meetsma, R. Rittberger, C. J. Brabec, N. S. Sariciftci, and J. C. Hummelen, "Influence of the solvent on the crystal structure of PCBM and the efficiency of MDMO-PPV : PCBM 'plastic' solar cells," Chemical Communications, 2116-2118 (2003).

96. J. R. Lakowicz, *Principles of Fluorescence Spectroscopy* (Springer, New York, 2006).

97. Y. S. Huang, S. Westenhoff, I. Avilov, P. Sreearunothai, J. M. Hodgkiss, C. Deleener, R. H. Friend, and D. Beljonne, "Electronic structures of interfacial states formed at polymeric semiconductor heterojunctions," Nature Materials **7**, 483-489 (2008).

98. A. Ashkin, "Acceleration and Trapping of Particles by Radiation Pressure," Physical Review Letters **24**, 156-159 (1970).

99. A. Ashkin, J. M. Dziedzic, J. E. Bjorkholm, and S. Chu, "Observation of a Single-Beam Gradient Force Optical Trap for Dielectric Particles," Optics Letters **11**, 288-290 (1986).

100. A. Ashkin, "History of optical trapping and manipulation of small-neutral particle, atoms, and molecules," Ieee Journal of Selected Topics in Quantum Electronics **6**, 841-856 (2000).

101. M. D. Wang, H. Yin, R. Landick, J. Gelles, and S. M. Block, "Stretching DNA with optical tweezers," Biophysical Journal **72**, 1335-1346 (1997).

102. K. Svoboda, C. F. Schmidt, B. J. Schnapp, and S. M. Block, "Direct Observation of Kinesin Stepping by Optical Trapping Interferometry," Nature **365**, 721-727 (1993).

103. E. R. Dufresne, G. C. Spalding, M. T. Dearing, S. A. Sheets, and D. G. Grier, "Computer-generated holographic optical tweezer arrays," Rev. Sci. Instrum. **72**, 1810-1816 (2001).

104. K. Svoboda and S. M. Block, "Optical Trapping of Metallic Rayleigh Particles," Optics Letters **19**, 930-932 (1994).

105. S. Chu, J. E. Bjorkholm, A. Ashkin, and A. Cable, "Experimental-observation of optically trapped atoms," Physical Review Letters **57**, 314-317 (1986).

106. S. Schultz, D. R. Smith, J. J. Mock, and D. A. Schultz, "Single-target molecule detection with nonbleaching multicolor optical immunolabels," Proceedings of the National Academy of Sciences of the United States of America **97**, 996-1001 (2000).

107. M. Z. Liu, P. Guyot-Sionnest, T. W. Lee, and S. K. Gray, "Optical properties of rodlike and bipyramidal gold nanoparticles from three-dimensional computations," Physical Review B **76**, 235428 (2007).

108. S. J. Oldenburg, J. B. Jackson, S. L. Westcott, and N. J. Halas, "Infrared extinction properties of gold nanoshells," Applied Physics Letters **75**, 2897-2899 (1999).

109. A. D. Yoffe, "Semiconductor quantum dots and related systems: electronic, optical, luminescence and related properties of low dimensional systems," Advances in Physics **50**, 1-208 (2001).

110. H. Kataura, Y. Kumazawa, Y. Maniwa, I. Umezu, S. Suzuki, Y. Ohtsuka, and Y. Achiba, "Optical properties of single-wall carbon nanotubes," Synthetic Metals **103**, 2555-2558 (1999).

111. K. C. Neuman and S. M. Block, "Optical trapping," Rev. Sci. Instrum. **75**, 2787-2809 (2004).

112. C. Selhuber-Unkel, I. Zins, O. Schubert, C. Sonnichsen, and L. B. Oddershede, "Quantitative optical trapping of single gold nanorods," Nano Lett. **8**, 2998-3003 (2008).

113. G. Mie, "Beiträge zur Optik trüber Medien, speziell kolloidaler Metallösungen," Annalen der Physik **330**, 377-445 (1908).

114. H. C. v. d. Hulst, *Light Scattering by Small Particles,* 1st ed. (Dover, New York, 1981).

115. M. I. Mishchenko, L. D. Travis, and A. A. Lacis, *Scattering, Absorption, and Emission of Light by Small Paticles,* 1st ed. (Cambridge, New York, 2002).

116. K. F. Ren, G. Grehan, and G. Gouesbet, "Radiation Pressure Forces Exerted on a Particle Arbitrarily Located in a Gaussian-Beam by Using the Generalized Lorenz-Mie Theory, and Associated Resonance Effects " Opt. Commun. **108**, 343-354 (1994).

117. T. A. Nieminen, H. Rubinsztein-Dunlop, N. R. Heckenberg, and A. I. Bishop, "Numerical modelling of optical trapping," Computer Physics Communications **142**, 468-471 (2001).

118. T. A. Nieminen, H. Rubinsztein-Dunlop, and N. R. Heckenberg, "Multipole expansion of strongly focussed laser beams," Journal of Quantitative Spectroscopy & Radiative Transfer **79**, 1005-1017 (2003).

119. T. A. Nieminen, H. Rubinsztein-Dunlop, and N. R. Heckenberg, "Calculation of the T-matrix: general considerations and application of the point-matching method," Journal of Quantitative Spectroscopy & Radiative Transfer **79**, 1019-1029 (2003).

120. T. A. Nieminen, N. R. Heckenberg, and H. Rubinsztein-Dunlop, "Computational modelling of optical tweezers," SPIE Proc. **5514**, 514-523 (2004).

121. T. A. Nieminen, V. L. Y. Loke, A. B. Stilgoe, G. Knoner, A. M. Branczyk, N. R. Heckenberg, and H. Rubinsztein-Dunlop, "Optical tweezers computational toolbox," Journal of Optics a-Pure and Applied Optics **9**, S196-S203 (2007).

122. C. H. Choi, J. Ivanic, M. S. Gordon, and K. Ruedenberg, "Rapid and stable determination of rotation matrices between spherical harmonics by direct recursion," J. Chem. Phys. **111**, 8825-8831 (1999).

123. A. Ashkin, "Forces of a single-beam gradient laser trap on a dielectric sphere in the ray optics regime," Biophysical Journal **61**, 569-582 (1992).

124. N. Malagnino, G. Pesce, A. Sasso, and E. Arimondo, "Measurements of trapping efficiency and stiffness in optical tweezers," Opt. Commun. **214**, 15-24 (2002).

125. M. Born and E. Wolf, *Principles of Optics,* 7th ed. (Cambridge, New York, 2005).

126. L. Novotny and B. Hect, *Principles of Nano-Optics,* 1st ed. (Cambridge, New York, 2006).

127. J. D. Jackson, *Classical Electrodynamics,* 3rd ed. (Wiley, 1998).

128. C. F. Bohren and D. R. Huffman, *Absorption and Scattering of Light by Small Particles,* 1st ed. (Wiley, New York, 1998).

129. D. T. Chiu and R. N. Zare, "Biased diffusion, optical trapping, and manipulation of single molecules in solution," J. Am. Chem. Soc. **118**, 6512-6513 (1996).

130. K. C. Toussaint, M. Liu, M. Pelton, J. Pesic, M. J. Guffey, P. Guyot-Sionnest, and N. F. Scherer, "Plasmon resonance-based optical trapping of single and multiple Au nanoparticles," Optics Express **15**, 12017-12029 (2007).

131. P. M. Hansen, V. K. Bhatia, N. Harrit, and L. Oddershede, "Expanding the optical trapping range of gold nanoparticles," Nano Lett. **5**, 1937-1942 (2005).

132. R. R. Agayan, F. Gittes, R. Kopelman, and C. F. Schmidt, "Optical trapping near resonance absorption," Applied Optics **41**, 2318-2327 (2002).

133. M. J. Lang, P. M. Fordyce, A. M. Engh, K. C. Neuman, and S. M. Block, "Simultaneous, coincident optical trapping and single-molecule fluorescence," Nat. Methods **1**, 133-139 (2004).

134. K. Svoboda and S. M. Block, "Biological Applications of Optical Forces," Annu. Rev. Biophys. Biomolec. Struct. **23**, 247-285 (1994).

135. K. Visscher, S. P. Gross, and S. M. Block, "Construction of multiple-beam optical traps with nanometer-resolution position sensing," Ieee Journal of Selected Topics in Quantum Electronics **2**, 1066-1076 (1996).

136. L. Oddershede, S. Grego, r. Simon F. NÃ¸, and K. Berg-SÃ¸rensen, "Optical Tweezers: Probing Biological Surfaces," Probe Microscopy **2**, 129 (2001).

137. G. Knoner, S. Parkin, T. A. Nieminen, N. R. Heckenberg, and H. Rubinsztein-Dunlop, "Measurement of the index of refraction of single microparticles," Physical Review Letters **97**, 157402 (2006).

138. P. B. Johnson and R. W. Christy, "Optical-Constants of Noble-Metals," Physical Review B **6**, 4370-4379 (1972).

139. F. M. Fazal and S. M. Block, "Optical tweezers study life under tension," Nature Photonics **5**, 318-321 (2011).

140. M. J. Lang and S. M. Block, "Resource letter: LBOT-1: Laser-based optical tweezers," American Journal of Physics **71**, 201-215 (2003).

141. E. Eriksson, J. Enger, B. Nordlander, N. Erjavec, K. Ramser, M. Goksor, S. Hohmann, T. Nystrom, and D. Hanstorp, "A microfluidic system in combination with optical tweezers for analyzing rapid and reversible cytological alterations in single cells upon environmental changes," Lab on a Chip **7**, 71-76 (2007).

142. S. M. Buck, Y. E. L. Koo, E. Park, H. Xu, M. A. Philbert, M. A. Brasuel, and R. Kopelman, "Optochemical nanosensor PEBBLEs: photonic explorers for bioanalysis with biologically localized embedding," Current Opinion in Chemical Biology **8**, 540-546 (2004).

143. A. Shvarev, "Photoresponsive ion-selective optical sensor," J. Am. Chem. Soc. **128**, 7138-7139 (2006).

144. V. Bychkova and A. Shvarev, "Fabrication of Micrometer and Submicrometer-Sized Ion-Selective Optodes via a Solvent Displacement Process," Analytical Chemistry **81**, 2325-2331 (2009).

145. V. Bychkova and A. Shvarev, "Surface Area Effects on the Response Mechanism of Ion Optodes: A Preliminary Study," Analytical Chemistry **81**, 7416-7419 (2009).

146. G. S. Roberts, T. A. Wood, W. J. Frith, and P. Bartlett, "Direct measurement of the effective charge in nonpolar suspensions by optical tracking of single particles," J. Chem. Phys. **126**, 194503 (2007).